ABSTRACT

Title of Dissertation:	UNDERSTANDING THE REACTION MECHANISM OF ALUMINUM NANOCOMPOSITE THERMITES
	Garth Christopher Egan, Doctor of Philosophy, 2015
Dissertation directed by:	Professor Michael R. Zachariah, Department of Chemical and Biomolecular Engineering and Department of Chemistry and Biochemistry

Nanocomposite energetics are a relatively new class of materials that combine nanoscale fuels and oxidizers to allow for the rapid release of large amounts of energy. In thermite systems (metal fuel with metal oxide oxidizer), the use of nanomaterials has been illustrated to increase reactivity by multiple orders of magnitude as a result of the higher specific surface area and smaller diffusion length scales. However, the highly dynamic and nanoscale processes intrinsic to these materials, as well as heating rate dependencies, have limited our understanding of the underlying processes that control reaction and propagation. For my dissertation, I have employed a variety of experimental approaches that have allowed me to probe these processes at heating rates representative of free combustion with the goal of understanding the fundamental mechanisms.

Dynamic transmission electron microscopy (DTEM) was used to study the *in situ* morphological change that occurs in nanocomposite thermite materials subjected to rapid (10^{11} K/s) heating. Aluminum nanoparticle (Al-NP) aggregates were found to lose their nanostructure through coalescence in as little as 10 ns, which is much faster than any other timescale of combustion. Further study of nanoscale reaction with CuO determined that a condensed phase interfacial reaction could occur within 0.5-5 μs in a manner consistent with bulk reaction, which supports that this mechanism plays a dominant role in the overall reaction process. Ta nanocomposites were also studied to determine if a high melting point (3280 K) affects the loss of nanostructure and rate of reaction.

The condensed phase reaction pathway was further explored using reactive multilayers sputter deposited onto thin Pt wires to allow for temperature jump (T-Jump) heating at rates of ~$5x10^5$ K/s. High speed video and a time of flight mass spectrometry (TOFMS) were used to observe ignition temperature and speciation as a function of bilayer thickness. The ignition process was modeled and a low activation energy for effective diffusivity was determined. T-Jump TOFMS along with constant volume combustion cell studies were also used to determine the effect of gas release in nanoparticle systems by comparing the reaction properties of CuO and Cu_2O.

UNDERSTANDING THE REACTION MECHANISM OF ALUMINUM NANOCOMPOSITE THERMITES

by

Garth Christopher Egan

Dissertation submitted to the Faculty of the Graduate School of the
University of Maryland, College Park, in partial fulfillment
of the requirements for the degree of
Doctor of Philosophy
2015

Advisory Committee:
Professor Michael R. Zachariah, Chair
Professor John Cumings
Professor Ichiro Takeuchi
Professor Liangbing Hu
Professor Bryan W. Eichhorn, Dean's Representative

Dedication

To my wonderful wife Kim, for providing a constant supply of cheer, optimism, and love throughout the entire process. To my parents, whose love and support made everything in my life possible. To my brother and sister, Laird and Tessa, for being such inspirational and awesome people.

Acknowledgements

I am incredibly grateful for all the people who helped make this dissertation possible and who have shaped my life over these past 5 and a half years.

First and foremost, I want to thank Dr. Michael Zachariah for being a fantastic advisor. His advice and example have taught me so much about how to be a successful researcher and person. I am particularly grateful for all the opportunities to collaborate on wide range of exciting projects that he made possible.

I would also like to thank all my current and former lab mates, particularly Dr. Kyle Sullivan, Dr. Nick Piekiel, Dr. Guoqiang Jian, Dr. Wenbo Zhou, Jeffery Delisio, Phillip Guerieri, Rohit Jacob, and Carlos Rodrigez for their years of invaluable input and support. I would also like to thank my many collaborator for all their time, efforts, and expertise and for trusting me with their work. In particular, thanks to Dr. Edward Mily, Dr. Thomas Lagrange, Dr. Bryan Reed, Dr. Joseph Mckeown, Dr. John Roehling, Dr. Tammy Olson, and Dr. Yong Han. Also thanks to Dr. Sz-Chian Liou and Dr. Wen-An Chiou of the UMD Nanocenter's AIMLab and to my undergraduate researchers who helped me deal with all the troubles of thermite printing, Ellen Cesewski and Amine Oueslati.

Finally, I'd like to acknowledge my advisory committee for their time and advice. I'd also like thank the Army Research Office and the Defense Threat Reduction Agency for financial support of my projects.

Table of Contents

List of Tables

List of Figures

List of Supplemental Figures

List of Appendix Figures

List of Abbreviations

SEM	Scanning Electron Microscopy/Microscope
TEM	Transmission Electron Microscopy/Microscope
DTEM	Dynamic TEM
MM-DTEM	Movie Mode DTEM
SAED	Selected Area Electron Diffraction
EDS/EDX	Energy Dispersive X-ray Spectroscopy
BSE	Backscattered Electrons
EELS	Electron Energy Loss Spectroscopy
XRD	X-ray Diffraction
T-Jump	Temperature Jump
TOFMS	Time-of-Flight Mass Spectrometer
MCP	Microchannel Plates
FWHM	Full Width at Half Maximum
TGA	Thermogravimetric Analysis
DSC	Differential Scanning Calorimetry
MEMS	Microelectromechanical Systems
PVD	Physical Vapor Deposition
RF	Radio Frequency
CCD	Charge-Coupled Device
CW	Continuous Wave
CEA	Chemical Equilibrium with Applications
MD	Molecular Dynamics

NIST	National Institute of Standards and Technology
LLNL	Lawrence Livermore National Laboratory
n-Al	Nanoaluminum
Al-NPs	Aluminum Nanoparticles
UFG	Ultrafine grain
RDX	Cyclotrimethylenetrinitramine
TNT	2, 4, 6-trinitrotoluene
NC	Nitrocellulose
MIC	Metastable Intermolecular Composites
ESD	Electrostatic Discharge
MDM	Melt Dispersion Mechanism
ARM	Arrested Reactive Milling

Chapter 1: Introduction

1.1. Nanoenergetic Materials

The term energetic material encompasses a wide range of systems that can generally be characterized as possessing a large amount of chemical energy that can be rapidly released upon initiation of reaction. More conventionally, the term is used to refer to explosives, propellants, and pyrotechnics. Most often, the energy of these systems is released through the oxidation of a fuel, such as carbon or hydrogen.[1] If both the fuel and oxidizer are held within a single molecule, that energetic is referred to as monomolecular.[2] Classic examples of this are trinitrotoluene (TNT) and cyclotrimethylenetrinitramine (RDX), which both decompose to produce CO, N_2, and H_2O along with significant energy. The other class of energetic materials are composites, meaning that the fuel and oxidizers are held in different phases and that are often physically mixed together.[2] Black powder, the original energetic material, is an example of this, with charcoal and sulfur serving as fuels and with potassium nitrate as the oxidizer.[1] Composites allow for the use of a wide range of different fuels, including metals, which are valuable because they are generally stable and store large amounts of chemical energy. This latter point is illustrated in Figure 1.1, where the specific energy (energy per mass) and energy density (energy per volume) of various metals are compared with common monomolecular explosives.[3]

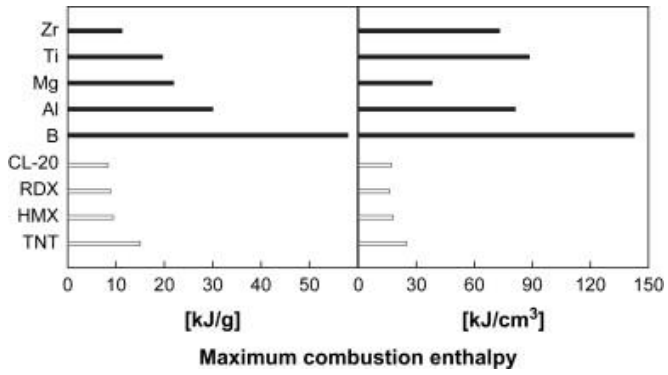

Figure 1.1. Specific energy and energy density of metal fuels compared with common monomolecular high explosives. Assumes complete combustion with oxygen that is not included in the mass or volume calculations. Reprinted from Progress in Energy and Combustion Science, 35, Dreizin, E. L., Metal-based reactive nanomaterials, 147-167, 2009, with permission from.[3]

When a metal fuel is combined with a metal oxide oxidizer, the composite energetic is referred to as a thermite. While this term has also been applied to other metal/oxidizer composites, the traditional thermite reaction is:

$$M_A + M_B O \rightarrow M_A O + M_B + \Delta H \qquad (1.1)$$

Where M_A is the metal fuel, $M_B O$ is the metal oxide oxidizer (e.g., Fe_2O_3, CuO, Bi_2O_3, MoO_3), and ΔH is the enthalpy released from reaction. This reaction is exothermic because $M_A O$ is more stable than the oxidizer. Aluminum is the most commonly used fuel because of its high energy content (see Figure 1.1), good reactivity, relative abundance, and low cost.[4] Iron oxide is a classic example of an oxidizer and the mixture of these two materials has long been used in the welding of railways.

Despite the high energy density of these materials, their applications had been limited by slow reaction kinetics and high ignition thresholds.[3,5] For monomolecular energetics, the fuel and oxidizer are within a few atomic distances of each other, so the reaction is limited by the kinetics of decomposition rather than transport.[2] But for thermites made from traditional coarse powders (particles >>1 μm), the two

components can be separated by many microns and the diffusion of species between the two will end up being a limiting factor, which leads to slow reaction rates. But as the technologies for the fabrication and characterization of nanoscale materials have grown, it has become possible to overcome these limitations. An illustration of the advantages of using smaller particles is shown with a scale comparison of 1 µm particles and 100 nm particles in Figure 1.2. Additionally, nanoscale materials offer high specific surface area, which allows for more reaction and further enhances reaction.

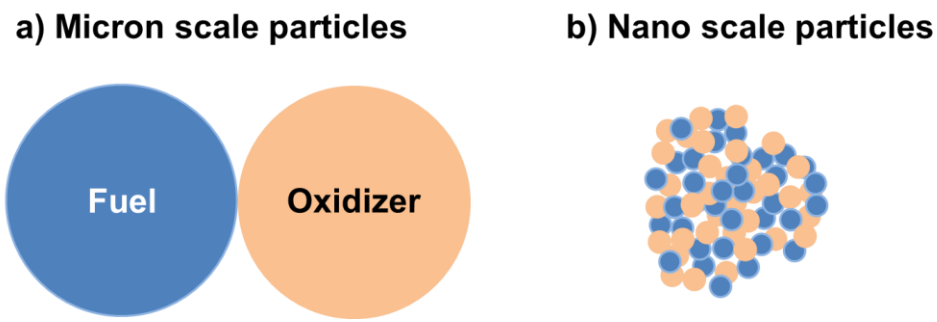

Figure 1.2. A scale illustration of the difference in diffusion distances between micron particles and nanoparticles. The particles in a) have a diameter 10 times that of the particles in b) and thus correspond to the difference between 1 µm particles and 100 nm particles.

The advantages of nanoscale particles in energetics were first demonstrated experimentally over two decades ago by Aumann *et al.* with what was referred to as ultrafine grain (UFG) aluminum that had primary particles with diameters of 20-50 nm.[6] In this and a large number of studies to follow, it was shown that nanoscales could react ~1000 times faster than traditional thermites and with much less energy needed for intiation.[7-10] While the term UFG is still used occasionally, more generally the term nanoparticle is used to refer to particles in the range of ten to several hundred nanometers. Similarly, to separate these highly reactive composites from the micron

scale variety, they have been referred to as metastable intermolecular composites (MICs), superthermites, nanothermites, and nanocomposite thermites interchangeably. In recent years the latter term has become most common and as I find it to be the most descriptive, I will primarily refer to these materials using that that phrase.

The high reaction rate demonstrated for nanocomposite thermites, along with their high energy density, have made them of significant interest to the energetic community. Another valuable characteristic they offer is their high degree of tunability, with particle size, oxidizer choice, stoichiometry, and packing density all having an impact on reactivity.[10-13] These properties make them attractive for traditional energetic applications (e.g., primers, explosive additives, propellant rate modifiers) as well as novel uses such as in microelectromechanical systems (MEMS). The low ignition thresholds and the ease with which these reactions propagate make nanocomposite thermites ideal for miniaturized systems where large amounts of energy is needed rapidly, as for *in situ*, small scale welding or gas generation for actuation.[14,15]

1.2. Nanocomposite Thermite Combustion

With any new class of materials, a critical step on the path to optimization and control is developing a deep understanding of the physics and chemistry involved in its processes. This allows for the development of models, which can drive and guide the further design of these systems. However, for nanocomposite thermites, several experimental challenges have limited our understandings of the fundamental physical

processes that drive reaction and propagation. In many ways, these challenges are direct consequences of the advantages gained by moving from traditional energetics to nanoscale materials. For example, the high reaction rates that make these materials so desirable, also demands that that the diagnostic tools used be capable of fast response and high temporal resolution. Additionally, while using smaller particles increases specific surface area and reduces length scales between fuel and oxidizers, which increase reactivity, it also limits our ability to directly probe reaction at the scale on which it occurs. The small sizes of these materials also leads to the formation of fractal aggregates during synthesis and handling as can be seen in Figure 1.3. Along with being complicated to model and understand, these complex morphologies promote coalescence and sintering that reduces surface area and destroys nanostructure on time scales faster or comparable to reaction.[16-18] Further, the high temperatures that are one of the most significant benefits of metal based nanoenergetics create complex multiphase and non-equilibrium environments during combustion, which significantly complicates interpretation of results.

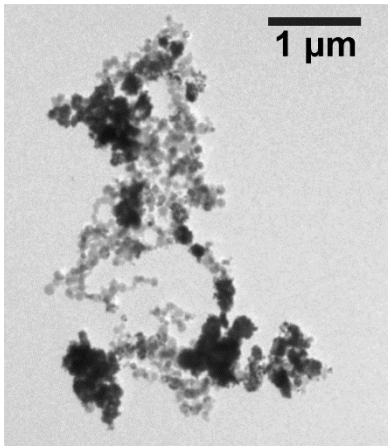

Figure 1.3. An example of the type of nanoparticles typically used in nanocomposite thermites. This images was taken with a transmission electron microscope (TEM). The lighter material is Al and the darker is CuO. The material was mixed in ethanol using ultrasonication.

More challenges arise from the reactive nature of the metallic fuels, which causes a 2-5 nm shell of oxide material to form on the nanoparticles and serve as a barrier to reaction.[19,20] Theses shells are perhaps also one of the reasons that nanoaluminum has been shown to have combustion behavior that is highly heating rate dependent.[21,22] This dependence places further constraints on experimental techniques by necessitating reproduction of the high heating rates (estimated at 10^5-10^8 K/s) found during combustion.[16,22] While there is still significant value to slow heating rate techniques (e.g., DSC, TGA), any theories of mechanistic behavior must be validated with experiments that produce these high heating rate conditions.[3]

The compounded impact of all these challenges has prevented the development of a cohesive theory for the physics that control nanoenergetic reaction. Indeed there are still several conflicting theories for the underlying mechanism.[16,20,23-25] All of this discussion is exemplified with one of the most prevalent experiments in the nanoenergetic community: burn tubes (see Figure 1.4).[26] These experiments are comprised of loading a tube with energetic material, igniting from one end, and observing the propagation of the luminous front with high speed video and/or the pressure wave with a series of pressure transducers to determine a flame speed.[10,26] Such experiments are good examples of high speed diagnostics and feature the high heating rates of free combustion, which has led to their results being used as the basis for many of the theories and models of nanoenergetic combustion.[20,27,28] However, even the straight forward and exceedingly prevalent measurement (flame speed) has been shown to be significantly complicated by the challenging nature of these materials. Recent work by Densmore *et al.* has helped illuminate how much is still

unknown about this widespread technique.[29] While the luminous front has long been taken as the reaction front, the authors showed that this front propagates even faster through unfilled tube, which suggests that it does not represent the ignition of new material but rather already combusting material being propelled forward through the tube. Other recent work has also shown that the materials remain hot and bright for milliseconds after the luminous front passed, which implies that significant unreacted material exists and continues to burn far outside the initial passage of the luminous front.[30] Thus the flame speed does not directly correspond to a reaction rate. For these reasons and despite being one of the most prevalent measurements found in the field of nanoenergetics, the actual physical meaning of the measurement is far from understood.

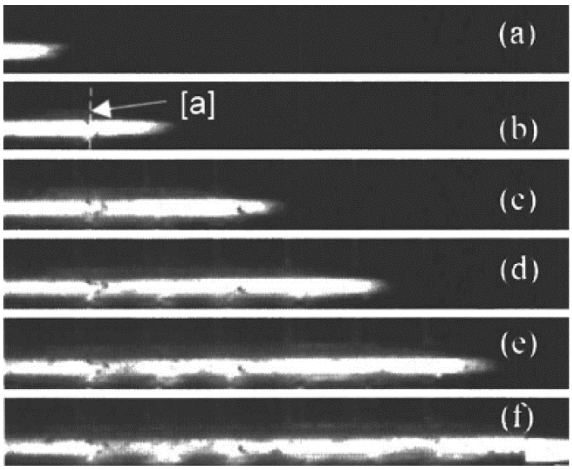

Figure 1.4. An example of a burn tube experiment involving Al/MoO3 nanocomposite. Parts (a)-(f) show sequential frames from a high speed camera taken ~20 μs apart, meaning frame (f) was taken 100 μs after (a). Point [a] represents the location of a sensor. Reprinted with permission from B. S. Bockmon, M. L. Pantoya, S. F. Son, B. W. Asay, and J. T. Mang, Journal of Applied Physics 98 (2005). Copyright 2005, AIP Publishing LLC.

The overall process of reaction propagation can be divided into two components: heat transfer and reaction. Heat transfer is generally better understood

than the reaction mechanisms, but includes some processes more complex than a simple categorization as conduction, convection or radiation. The evidence for these different possibilities will be discussed in the next section and some basic calculations done to further understand the problem are presented in Chapter 3. After heat transfer, the passivating effect of the oxide shell is explored. This layer serves as a barrier to reaction and must be overcome before or during the combustion process. This can be achieved through a simple diffusion of reactive ions through the barrier or a physical deterioration of the shell through fracturing or softening. The physics and evidence for these different processes as well as their potential impact on reaction mechanism will be discussed.

The remainder of this chapter focuses on three possible reaction mechanisms that have be proposed and considered throughout the literature. These are gas-condensed heterogeneous reaction, condensed phase interfacial reaction, and melt-dispersion mechanism (MDM). The first is a two-step process with the solid oxidizer decomposing to produce gaseous oxidizer (typically O_2) which then reacts heterogeneously with the solid or molten fuel. The second involves the transport of reacting species through the condensed phase and across the inter-component interfaces.[16,24] Lastly, MDM has been theorized to occur for high heating rates of aluminum nanoparticles, where pressure build up from the melting of the core causes violent rupture of the oxide shell and spallation of the Al core into small droplets which burn at high rates.[22,25,31] While multiple pathways could contribute to the overall reaction process, one will be the dominant process, although it is possible that which one dominates could change depending on combustion conditions.

1.3. Heat Transfer

In order for bulk scale energetic material to be combusted, the energy that is generated locally from reaction must be transported into the unreacted, cooler material. This material then starts reacting and generating heat, thereby propagating the self-sustaining combustion.

For nanocomposite thermites, burn tube experiments have proven that they can produce fast moving and hot gases.[29] Simultaneous optical and pressure measurements have shown that the waves of hot material coincide with or are slightly preceded by high pressure waves, even in materials that are not expected to produce significant gas.[10,32] This suggests that the primary means of heat transport is a convective/advective process, with hot gases and material being driven into the colder zones and depositing their heat. Indeed this has been supported throughout the literature.[7,10,13,27] The key evidence from these studies is that the highest flame speeds coincided with low packing densities, high gas production, low initial pressure, and confinement, which are all conditions that are most conducive to moving gases and material. In comparison, direct conduction would be oppositely affected by or insensitive to those parameters. Convection is further supported by the high specific surface area and small sizes intrinsic to nanoparticles, which yields a very low thermal relaxation time, meaning that in a hot gas they will quickly equilibrate to that temperature.[11] On the other hand, conduction would be hindered by the porous nature of nanoparticle beds, leading to an order of magnitude reduction in effective thermal conductivity.[33,34] Radiative heat transfer has not been observed to be an important factor, as tests with transparent barriers were found to arrest propagation.[7]

While it is clear that heat transfer driven by a convective process is well supported, the exact mechanism is not fully understood. In particular, it is not clear if it is hot gases alone or hot condensed phase material which transfers the bulk of the heat after being propelled into the cooler, unreacted material. While gases would greatly simplify the modelling process, recent studies have suggested that fast moving condensed phase material could play a large role. For example, with Al/MoO_3 it was observed that peak flame speed coincided with the highest production of gas above the melting point of Mo, which indicated that molten metal was important to propagation.[35] Additionally in open configuration, material was observed to have been thrown forward and to have ignited the unreacted material discontinuously.[36] Such behavior is not entirely surprising given the small stokes numbers of the nanoparticles will lead to significant entrainment.[30]

In order to better understand these possible heat transfer mechanisms, I present a series of simple calculations in Chapter 3. From these results, it can be determined that the movement of hot condensed phase material must be responsible for the fast heat transfer observed in nanocomposite thermite combustion.

1.4. The Oxide Shell

For any given sample of reactive metal a 2-5 nm oxide shell is expected to form upon exposure to air (see Figure 1.5).[19,23,37] Given the small length scales of nanomaterials, this thin layer can represent a significant portion of the mass leading to a large amount of dead weight. With aluminum, this passivating layers (Al_2O_3) has a melting temperature of 2345 K, which is much higher than the ignition temperatures typically found for aluminum based nanoenergetics.[6,13,38] Therefore, through ignition,

and potentially a significant portion of reaction, the shell is expected to be a barrier to reaction.

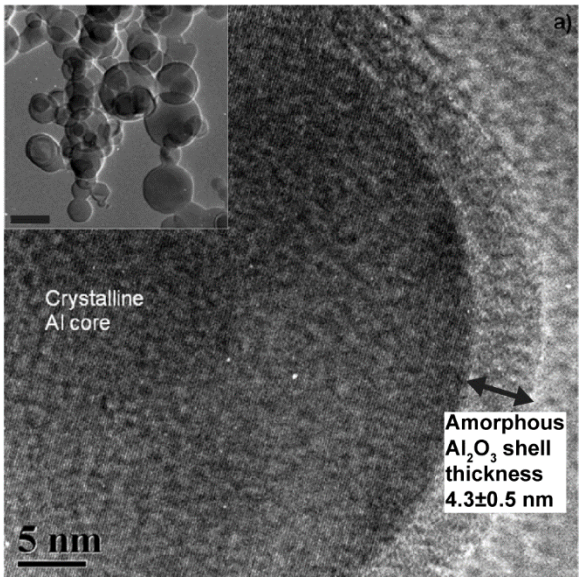

Figure 1.5. A high resolution transmission electron microscope (HR-TEM) image of an Al-NP and its amorphous oxide shell. The inset image is a lower magnification (scale bar = 100 nm) image of the same particle. Adapted with permission from D. A. Firmansyah, K. Sullivan, K. S. Lee, Y. H. Kim, R. Zahaf, M. R. Zachariah, and D. Lee, Journal of Physical Chemistry C 116, 404 (2012). Copyright 2012 American Chemical Society.

The simplest answer for how reaction occurs with respect to the shell would be a diffusion model where Al^+ diffuse out and O^- diffuse in. If oxygen diffused faster than the aluminum, this would produce a "shrinking core" scenario where the thickness of the shell increases inward, leading to a smaller and smaller metallic core.[39-41] Alternatively, if the outward diffusion of metallic ions is the faster process, then a thick, hollow oxide structures could result.[42] However, a hurdle to viability of this behavior is that self-diffusion coefficients for bulk Al_2O_3 are too low to account for the time scale measured in combustion experiments.[31] For example at ~2000 K, Ref. [43] gives values of ~10^{-15} and ~10^{-17} m^2/s for Al and O in alumina. So given even

a 2 nm oxide shell, one can expect a characteristic diffusion time ($\frac{l^2}{D}$) of 4 ms, which is much slower than the burn times and time scales found for Al-NP and nanothermite combustion which have shown responses on the order of 10-50 μs. This suggests that cross-barrier diffusion may only be viable under slow heating rate conditions.[31,44,45] However, the kinetics of this process could be significantly enhanced by other mechanisms, such as an intrinsic electric field to support enhanced diffusion with a Cabrera-Mott mechanism as has been shown in molecular dynamics (MD) simulations and used in other models.[46,47] It is possible that an initial diffusion step occurs during ignition, which then creates high temperatures and enables alternate pathways. This could explain the ignition delay observed in some systems.[23]

The alternative to a diffusive process is one that involves the mechanical breakdown of the oxide shell. This would allow for a molten Al core to quickly diffuse through the produced cracks or, if associated with a large pressure buildup, potentially lead to violent spallation into molten drops as predicted by MDM.[31,48] There are several different manners in which the impact of the shell could be reduced or removed through physical processes. For example, the breakdown of the shell has been modeled based on the density changes caused by crystallization from its initially amorphous state, which has been shown to occur at temperatures below the melting point of Al.[19] An illustration of this process is shown in Figure 1.6. Heterogeneous crystallization has also been observed in TEM to lead to localized fractures in the oxide shell.[37] However, both of these observations were made from slow heating rate (<40 K/min) experiments, so it is not clear if the heat rate dependencies discussed above would impact the kinetics of the observed processes at the higher heating rates

of combustion. Alternatively, a variety of MD simulations have shown a softening process in the oxide shell caused by interdiffusion between core and shell creating a metastable lower melting reduced oxide of Al.[17,49-51] Similar behavior was also observed in Reference 37 with swelling of the oxide without an oxidizing environment. Also some high heating rate (~$5x10^5$ K/s) mass spectrometry has shown evidence of a decreased melting temperature of the shell.[52] One final option is the rupture and cracking of the shell from stresses induced by the melting of the aluminum core at 933 K. Upon melting, Al will expand by an estimated 6% while the oxide shell remains relatively static.[31,48] For nanoparticles this could lead to a significant pressure buildup, which could drive the fracturing of the shell.

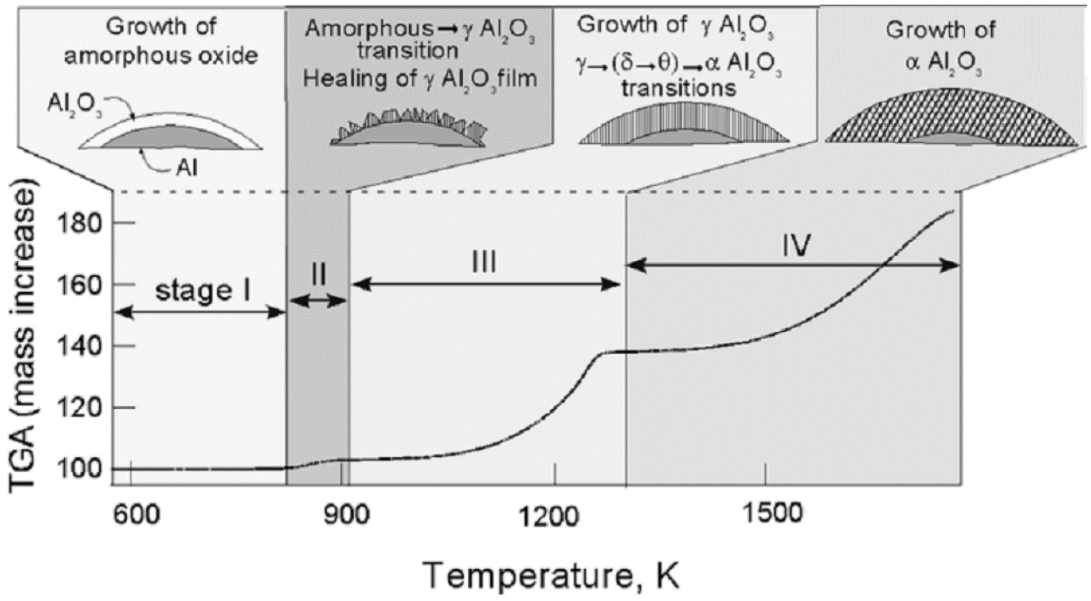

Figure 1.6. A schematic illustration of a proposed mechanism for aluminum oxidation based on the crystallization of the oxide shell. Reprinted with permission from M. A. Trunov, M. Schoenitz, and E. L. Dreizin, Combustion Theory and Modelling 10, 603 (2006). Copyright 2006 Taylor & Francis.

Experimentally validating any of these possible mechanisms is a challenging proposition because of the nanoscale of the behavior and the necessity to produce

high heating rates. One approach is to heat Al-NPs at high heating rates *ex situ* and analyze them after the fact with TEM. Both flash heating and T-Jump wire heating of Al-NPs in inert environments have shown the creation of hollow oxide structures that imply the escape of Al from the oxide shell, but it was not consistent for every nanoparticle.[52,53] Recent advances in the field of *in situ* electron microscopy has enabled direct imaging of morphological changes. High heating rate (~10^6 K/s) hot stage studies have shown that heating Al-NPs above their melting points does not necessarily lead to the breakdown of the oxide shell.[16] In Chapter 4, I build on these results using the same heating capability as well as dynamic transmission electron microscopy (DTEM) that is capable of nanosecond resolution and ~10^{11} K/s heating.[54] I find that oxide breakdown occurs rapidly, but nonviolently and is followed by coalescence rather than spallation.

1.5. Possible Reaction Mechanisms

1.5.1. Gas-Condensed Heterogeneous Reaction

There has been little consensus on the reaction mechanism of nanoenergetics. As discussed earlier, the possible physics can be fit into three broad categories. The first that I will discuss is the gas-condensed heterogeneous reaction mechanism, which has developed in response to the observation that many of the nanoparticle oxidizers decompose to release oxygen at elevated temperatures.[38,45,55] This decomposition typically involves the reduction to a stable reduced phase (e.g., $CuO \rightarrow Cu_2O$, $Fe_2O_3 \rightarrow Fe_3O_4$, $Co_3O_4 \rightarrow CoO$, $WO_3 \rightarrow WO_2$). High heating rate mass

spectrometry of these oxides and the corresponding thermites has shown that this reduction process often occurs at temperatures comparable to ignition and that significant gaseous oxygen is present during reaction.[38,55] This is all in accordance with the gas-condensed heterogeneous reaction mechanism, which is based on the burning of the fuel in the high pressure O_2 environment created by the decomposition of these oxides. Part of the attraction of this mechanism is its relative simplicity, as it can be treated as almost a one component system. The limiting step is either the reduction of the oxide to produce oxygen or the reaction of the fuel with the gas. As these two processes likely have very different kinetics, the overall reaction rate can be reduced to the slower of the two. Focusing on reaction, the problem of spheres burning in gases is a long studied and well understood one.[5] So even allowing for the role of the shell or the potential loss of nanostructure, this mechanism is conducive to relatively straight forward models. Further it also has the advantage that burning of metallic nanoparticles in oxidizing environments can be studied directly in wide array of different experiments.[56-58] Such studies provide a valuable metric in assessing the viability of the gas-condensed reaction mechanism as the time scales for the two forms of combustion can be compared.

To make this comparison, it is important to first establish a timescale for nanothermite combustion, which is not a straight forward task. From burn tubes, velocities of ~1 km/s and a reaction front width of 10 mm have been reported.[7] This suggests a characteristic time of ~10 μs, but as discussed above, the exact nature of this front is not well understood. Constant volume pressure cell tests of the fastest nanocomposites suggest two rather distinct timescale, as can be seen in Figure 1.7.

The pressure signal reaches its peak values in ~10 µs which is comparable to the burn tube experiments. On the other hand the optical signal doesn't reach its maximum until ~100 µs and has a full width at half maximum (FWHM) value of more than twice that. This order of magnitude difference in time scales suggests a two-step process that could be indicative of initial reaction, which heats up and reduces the oxidizer followed by heterogeneous burning in the released O_2.[45] For extended burn tubes, material has been observed to stay hot for ~3 ms after the initial expansion.[30] The challenge in interpreting these timescales is that it is not clear how the measured values relate to the overall reaction progress of these materials.

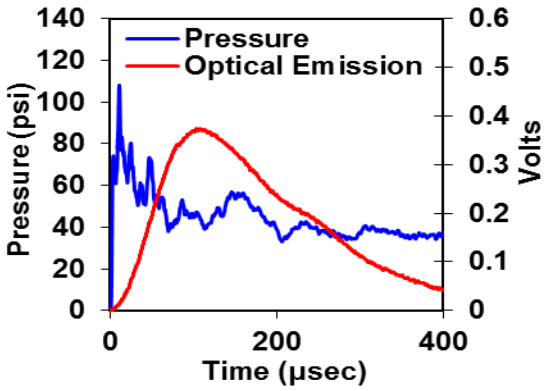

Figure 1.7. Results from Al/CuO nanothermite combustion in a constant volume pressure cell (25 mg of reactant in a 13 cc cell). Note that there is a considerable difference in the time to peak for the optical and pressure signals. For details of the experimental set up, see Section 2.3.

For Al-NPs burning in oxidizing environments, the key measurement is burn time. One setup used to make this measurement is a Bunsen burner type experiments where aerosolized Al is burned and the flame produced is observed.[58,59] For particles smaller than 100 nm, burn times range from 10 ms down to 200 µs depending on temperature and oxidizing environment. The fastest of these time scales lines up well with the slower time scales of the nanocomposites. Even faster burn times have been

found in shock tube experiments, which use a reflected shock to ignite materials at a variety of temperatures and elevated pressures.[41,44,57] Here Al-NPs where found to burn on a time scales of 50-500 µs. While that lower value is approaching the fast timescale for the nanothermites, the trend observed suggests 50 µs is the lower limit for burn time even at extreme pressures (32 atm) and temperature (>2000 K).[44] Therefore it seems unlikely that gas-condensed heterogeneous reaction could be responsible for the ~10 µs time scale, but could be responsible for a slower burning that occurs after the initial fast reaction.

Another reason why this mechanism is unlikely to play the dominant role in determining reaction rate, is that the decomposition properties of the oxidizer are not a good indicator of performance. With regards to ignition, there are some oxidizers (e.g., CuO, Fe_2O_3, $AgIO_3$) that show a correlation between the release of O_2 and the ignition with Al as is shown in Figure 1.8.[55] However, there are many more which show no similar trends. Indeed, Bi_2O_3, WO_3, MO_3, and SnO_2 have all been shown to ignite without any O_2 present. This suggests that for many cases, a gas-condensed heterogeneous reaction is not responsible for ignition.

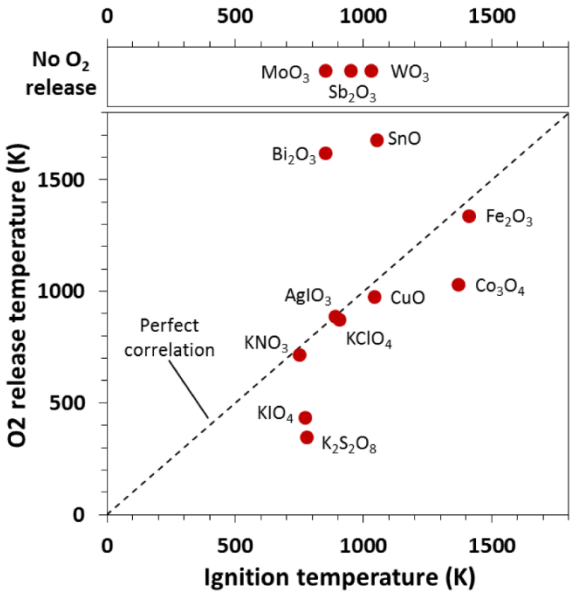

Figure 1.8. Data from high heating rate (~$5x10^5$ K/s) temperature jump time of fight mass spectrometry (T-Jump TOFMS) experiments such as those in Reference 55 and described in Section 2.2. This figure shows the temperature at which O_2 was first observed during heating of the oxidizer alone (Y-axis) versus the ignition temperature of the oxidizer when mixed stoichiometrically with Al-NPs (X-axis). The oxidizers that were found to not release O_2 below the experimental limit (1700K) are plotted separately at the top of the figure.

Further, if gaseous oxygen was critical to the reaction, it would follow that the materials which releases very little oxygen or decompose only at high temperatures would perform significantly worse than the O_2 producers. However, comparing Figure 1.9 and Table 1.1 reveals that this is not the case. Figure 1.9 shows the oxygen release profiles for various oxides during 3 ms heating pulses of ~$5x10^5$ K/s. It is clear that CuO produces the most oxygen, earliest, followed but Fe_2O_3, Bi_2O_3, and then SnO_2. Note that the time that the O_2 signal first rises is proportional to the O_2 release temperatures (position along y axis) plotted in Figure 1.8. If the presence of gaseous oxygen was important to the overall reaction process, it would follow that CuO would perform the best in combustion tests with Fe_2O_3, Bi_2O_3, and SnO_2 performing comparably but with Fe_2O_3 being the best of that bunch. However, Table

1.1 shows that this is not the case. The pressurization rate, which correlates to flame speed in a burn tube and is indicative of overall performance, is similar for CuO, Bi_2O_3, and SnO_2.[9] Only Fe_2O_3 is a significantly worse performer, with a pressurization rate 2 orders of magnitude slower. Similarly, MoO_3, which does not release O_2 below 1700K, will also react in the TOFMS with aluminum without the presence of detectable O_2 during reaction.[38] Thus, again, if gaseous oxygen was critical to reaction mechanism, MoO_3 would be expected to be a terrible performer, but burn tube studies have found it to be one of the best.[10]

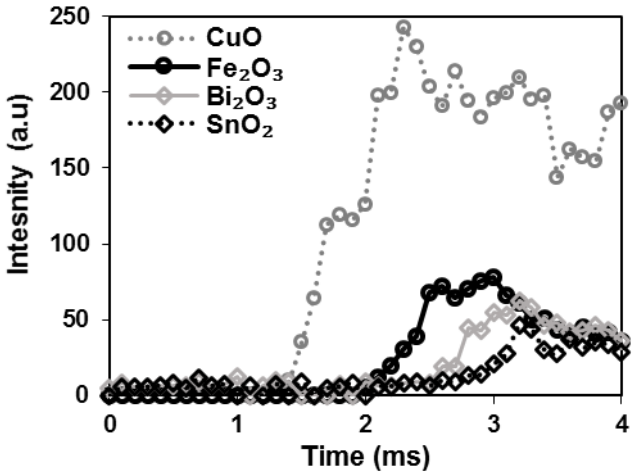

Figure 1.9. The O_2 release profiles from various oxidizers as measure by T-Jump TOFMS. Each sample was heated with a similar 3 ms long heating pulse of ~$5x10^5$ K/s.

	Peak pressure (PSI)	Pressurization rate (PSI/μs)	FWHM burning time (μs)
Al/SnO_2	80	7.7	210
Al/Bi_2O_3	123	12	193
Al/CuO	108	11	185
Al/Fe_2O_3	13	0.017	936

Table 1.1. Experimental combustion cell results for various thermites. Data taken with setup discussed in Section 2.3.

1.5.2. Condensed Phase Interfacial Reaction

As an alternative to the previously discussed mechanism, this one assumes that oxidation occurs directly between the condensed phase (i.e., solid or molten) fuel and the condensed phase oxidizer. While this has often been considered as a possible pathway for reaction of nanoenergetics, the underlying properties and processes have not been significantly developed. This is in part because it is a far more challenging problem to conceptualize and model in comparison to particles burning in a gas. Consider the complex aggregate morphology shown in Figure 1.3. How would a condensed phase reaction progress for this case? By definition it must occur across interfaces between the materials, but in this initial configuration the amount of interfacial area is only the points of contact between adjacent nanoparticle spheres of differing components. These very limited interfaces would severely inhibit the flux of reacting species and lead to very slow reaction. However, if there is some degree of mobility in either the fuel or the oxidizer, it can coalesce towards the opposite component and thereby increase the amount of contact. The increased interfacial area will increase reaction rates, which will generate heat, which will drive further coalescence leading to a feedback loop of sorts. This general process, which is illustrated schematically in Figure 1.10, has been dubbed reactive sintering.[16]

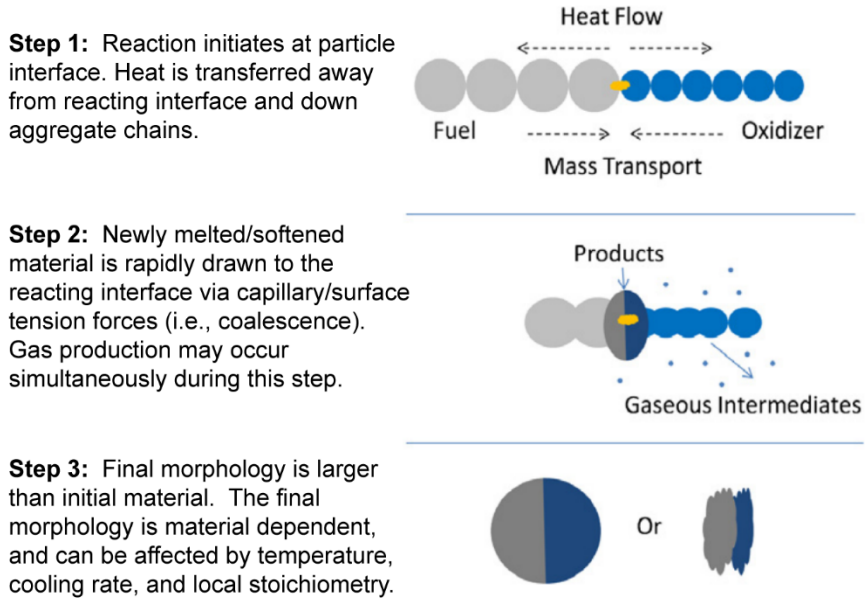

Figure 1.10. A schematic representation of the reactive sintering process. Adapted from Combustion and Flame, 159, Sullivan, K. T. et al., Reactive sintering: An important component in the combustion of nanocomposite thermites, 2-15, Copyright 2012, with permission from Elsevier

Even with this general conception for the mechanism, the details and information needed to derive models are far from clear. For example, this process is dependent on the loss of the original nanostructure, which means the initial configurations and morphologies will be lost prior to the bulk of reaction. How then will the length scale and total interfacial area develop? And how, if at all, will this process be related to that initial configuration? But before delving into such complicated processes, I will assess the viability of this proposed mechanism.

To do so, I will first consider a system that vastly simplifies the problem of reaction to a question of one dimensional diffusion. Reactive multilayers or nanolaminates are fully dense planar structure made up of alternating layers of fuel and oxidizer (Al/CuO example shown in Figure 1.11) or two metals that can combine to form an intermetallic phase.[15,60-62] Typically, they are created by physical vapor

deposition. Being fully dense limits reaction to the condensed phase and the planar geometry means that the interfaces and diffusion distances are well defined. For Al/CuO nanolaminates, speeds have been measured up to ~80 m/s which is comparable to values found for nanoparticle thermites in similar open configuration experiments.[13,36,62] This indicates that condensed phase reaction could be fast enough to account for the high reaction rates in nanothermites if there is sufficient interfacial area. To estimate if this amount of contact is reasonable, consider that ~80 m/s was achieved with bilayers that were 150 nm thick and comprised of 18% Al by weight. For a single bilayer there will be a single interface between components and the area of this interface on a per mass basis can be calculated as $\frac{A}{At_{\mathrm{b}}\rho} = \frac{1}{t_{\mathrm{b}}\rho}$, where A is the interfacial area (width of film times length), t_{b} is the bilayer thickness, and ρ is the average density. So for the 80 m/s case, there is 1.3 m^2/g of interfacial area. As bilayers are stacked, there will be additional interfaces between the bilayers, so with an infinite number of bilayers there will be two interfaces per bilayer, which would mean 2.6 m^2/g of interfacial area. Given that the nanoparticles typically used in nanothermites have specific surface areas an order of magnitude higher (27.7 m^2/g for 80 nm spherical Al-NPs), it seems reasonable that comparable interfacial area could be achieved even after considerable loss of nanostructure.[10]

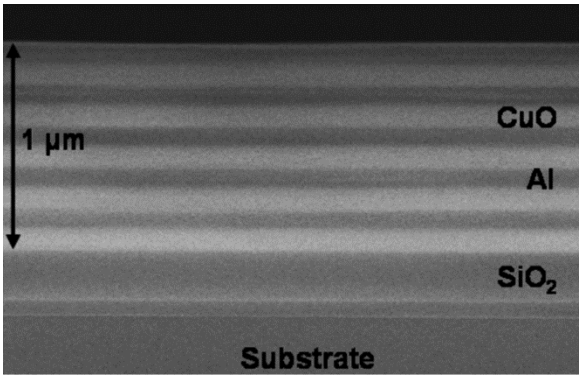

Figure 1.11. An example of an Al/CuO reactive multilayer that was sputter deposited onto an oxidized silicon substrate. Reprinted with permission from M. Petrantoni, C. Rossi, L. Salvagnac, V. Conedera, A. Esteve, C. Tenailleau, P. Alphonse, and Y. J. Chabal, Journal of Applied Physics 108 (2010). Copyright 2010, AIP Publishing LLC.

Another example of thermite material that is restricted to reacting through the condensed phase is material produced through arrested reactive milling (ARM).[40,63-66] This procedure typically involves ball milling powders into fully dense, micron scale materials that contain both fuel and oxidizer as nanoscale inclusions, as is shown in Figure 1.12. As with the nanolaminates the fully dense nature of the materials limits the role of any gas based reaction mechanism, although the geometry here is less simple to model and the amount of interfacial area is not as well known. However, the fact remains that these materials have been found to burn very quickly, with reaction initiated through electrostatic shock and flyer plates shown to have burn times <100 µs.[64] This is very similar to the timescales discussed in the previous section for loose powder nanothermites, which again suggests that condensed phase reaction kinetics are fast enough to explain combustion.

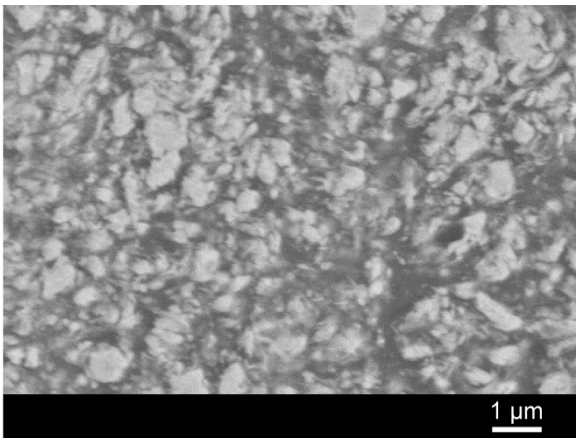

Figure 1.12. An example cross-section of a fully dense Al/CuO nanocomposite produced with ARM. Note the scale bar represents 1 µm. Reprinted from Combustion and Flame, 158, Ermoline, A. et al., Reactions leading to ignition in fully dense nanocomposite Al-oxide systems, 1076-1083, Copyright 2011, with permission from Elsevier.

Assuming that the kinetics of this condensed phase reaction are sufficiently fast, the next step is to determine if it actually occurs during combustion. One of the defining properties of the condensed-phase reaction mechanism as discussed so far is the loss of nanostructure and increase in particle size. Therefore, the products that result from such a reaction will be easily identifiable by significant interfaces and large sizes relative to the initial nanoscale reactants. Indeed there have been several different studies that have involved the capture of nanoenergetic material from a variety of experimental setups that have shown this type of product.[24,36,67,68] All these products exhibit resulting morphologies that were larger than 1 µm and contained both fuel and oxide elements within one particle as an alloy or in adjoining phases as shown in Figure 1.13a. In their experimental set up, Jacob et al. were able to measure the time at which the product was collected relative to the point of ignition. From this they were able to determine that the products could not have formed from the vapor phase because not enough time had elapsed to form such large products. Thus these

large products must have formed directly in the condensed phase. The authors also noticed a large number of nanosized products that can be seen decorating the micron scale particle in Figure 1.13b. These averaged ~50 nm in diameter and were consistent with homogenous nucleation from the vapor phase. However, volume analysis indicated that this nanomaterial represented <15% of the total mass of the product.[24]

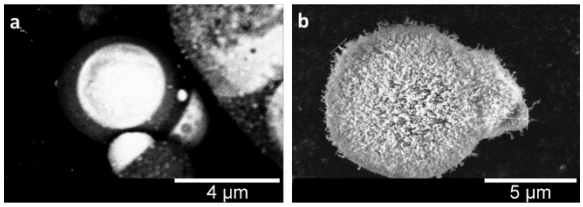

Figure 1.13. Product captured from a T-jump ignition experiment on Al/CuO nanothermite. The material in a) was captured ~90 µs after ignition and was imaged using back-scattered electrons (BSE) which makes the heavier elements (Cu) appear brighter. The material in b) was capture further out at a time of ~350 µs and does not use BSE. Reprinted from Combustion and Flame, 162, Jacob, R. et al., Energy release pathways in nanothermites follow through the condensed state, 258-264.Copyright 2015, with permission from Elsevier.

The results of these studies fully supports that condensed phase reaction occurs and is the dominant mechanism for nanothermite combustion. The significant loss of nanostructure that occurs in the formation of the large particles effectively closes off the possibility of fast gas-condensed heterogeneous reaction as the rates of that mechanism are highly size dependent.[58] Further, the large mass percent that these products represent suggest that they will be most responsible for generating heat. However, there are some inconsistencies between past results that must be addressed before this mechanism can be taken for granted. In particular, the work with Al/Bi_2O_3 in References 24 and 67 both showed the formation of micron scale particles from coalescence but showed differences in composition. Jacob et al. exhibited particles

that contained both Al and Bi, while Poda et al. presented particles that were primarily Bi with the Al existing primarily as nanoscale Al_2O_3. It is unclear why the two different combustion techniques (wire heating vs constant volume bomb cell) would produce such differences. Additionally, some authors have reported the opposite trend, with final product morphologies being considerably smaller [25,53]. In these cases it may be possible that the observed particles were from the vapor phase as discussed above and that sampling technique minimized the capture of large particles.

The general processes of condensed phase reaction raise some further questions about the effect nanoscale features have on reaction. In particular, if much of the nanostructure is lost prior to and during combustion, what then are the advantages to using nanomaterial? This is a fundamental question to the discussion of nanoenergetics that can be addresses in several ways.

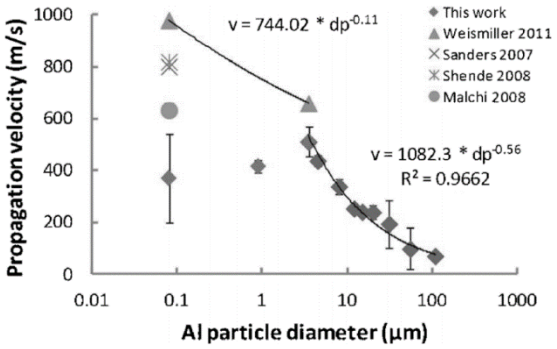

Figure 1.14. The effect of fuel particle size on combustion performance in a burn tube. Reprinted with permission K. T. Sullivan, J. D. Kuntz, and A. E. Gash, Propellants Explosives Pyrotechnics 39, 407 (2014). Copyright 2014 John Wiley and Sons.

First, there are several studies that have shown diminished returns in performance as particle size is reduced through the nano regime. Take for example the data reproduced in Figure 1.14, which shows burn tube flame speeds with varied

particle fuel size.[11] Note the marked difference in trends after sizes are reduced to less than 3.5 μm, as well as the large spread in nanoparticle data. Another example is burn times of Al-NPs in gaseous oxidizers, which are expected to scale linearly with diameter under kinetically controlled burning.[5] However, studies have shown much lower dependence with a scaling law closer to $d^{0.3}$ instead.[58] In both these cases, the diminished returns through further reduction in size can be explained by the loss of nanostructure, with the small initial particles coalescing into large particles.[18] If this happens prior to significant combustion, the material will have the kinetics of the larger particles. Such a process is supported by recent results that have shown that the time scales for coalescence and sintering are much faster than those for combustion. This was found in part using molecular dynamic simulations, an example of which is shown in Figure 1.15. Here, 8 nm particles were found to coalesce in 0.7 ns.[17] This value can be extrapolated to more complex aggregates of larger sizes based on a modified Frenkel law.[69] Doing so yields a time of 50 ns for an aggregate of 100 particles with 50 nm diameters. This value is far faster than any of the other timescales of combustion and lines up very well with my DTEM experiments on Al-NPs, which will be discussed in Chapter 4.

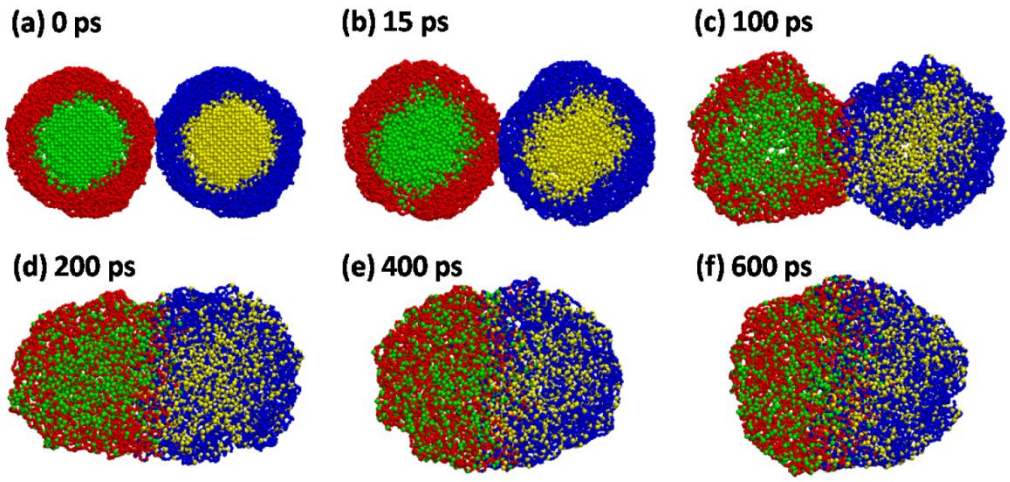

Figure 1.15. Molecular dynamics simulation of two 8 nm Al-NPs with oxide shells that were rapidly heated (0-15 ps) to 2000 K and held there. The different colors represent the different designations for each oxide as either shell (oxide) or core (aluminum). More details can be found in Reference 17.

Second, there are other potential advantages gained by using nanoparticles even if significant nanostructure is lost. One example is that nanomaterials allow for far more intimate mixing of fuel and oxidizer compared to larger composites. While it has been shown that that the initial configuration of the material is quickly lost, the number of inter-component interfaces during the early stages of reaction will still be dependent on the degree of segregation and the distances between components. Indeed, it has been shown that nanothermites are highly sensitive to mixing, although quantification of how this relates to inter-component distances has not been well characterized.[70-72] The initial nanoscale may also aid in heat transfer as the loss of nanostructure is not expected until temperatures comparable to ignition. Thus, the majority of the heating will occur prior to that process, when the material retains its small thermal mass and short thermal relaxation time. Additionally, the nanoscale could play a significant role in the breakdown of the oxide shell because the pressure buildup that could occur upon melting of the core would be size dependent.[31,48] Also,

the added surface energy of nanoparticles will drive coalescence, leading the molten Al to escape the shell as well as move towards reaction interfaces. In this way the loss of nanostructure process could be beneficial to some degree.

Third, if indeed a significant portion of the benefits of nanostructure is being lost to the coalescence intrinsic to the condensed phase mechanism, material design approaches could take account for this and minimize the effect. One way in particular that this has been achieved is with the use of structured gas generators.[68,73] Wang et al. were able to use electrospray to assemble Al/CuO thermite nanocomposite into microspheres (~5 μm) bound with nitrocellulose (NC), which would quickly generate gas at low temperature. The authors found that these mesoparticles significantly outperformed traditional Al/CuO as well as Al/CuO/NC that was physically mixed rather than assembled. The increased performance was found to correlate with product that was significantly smaller, as shown in Figure 1.16. It follows that the assembly and gas generation kept the Al/CuO nanoparticle from becoming too aggregated. As a result, the material retained more of its specific surface area as it coalesced, which would increase the reaction rate. This hypothesis has been further supported with Bunsen burner type tests on such microspheres.[73] This strategy has also been employed and showed promise in propellants, which further suggests its viability in the future.[74]

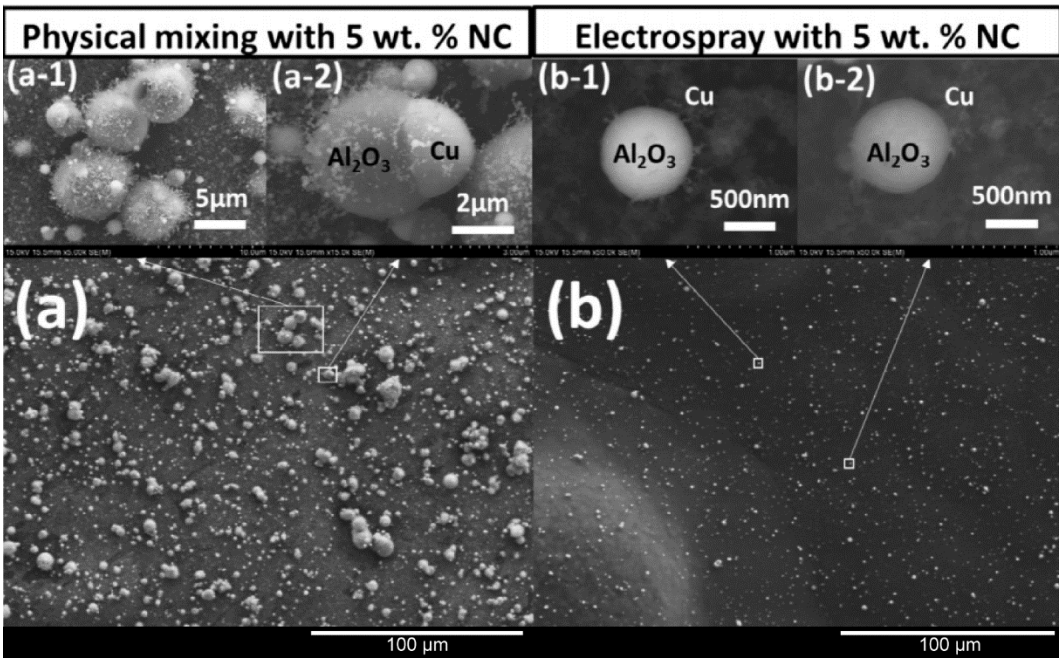

Figure 1.16. Product collected from the combustion of Al/CuO/NC nanoenergetics. The material for (a) was produced using a traditional nanothermite mixing technique (ultrasonication). Electrospray synthesis was used to form mesoparticles, which had increased overall performance and led to much smaller product as shown in (b). Reprinted from Combustion and Flame, 161, Wang, H. et al., Assembly and reactive properties of Al/CuO based nanothermite microparticles, 2203-2206, Copyright 2014, with permission from Elsevier.

While there is significant evidence for condensed phase reaction being an important mechanism, clearly more work is needed to explore all these issues discussed. Accordingly, a significant portion of this dissertation focusses on this mechanism. In Chapter 4 and Chapter 5 I make use of DTEM to observe the timescale of the nanoscale processes involved in nanostructure loss and condensed phase reaction. In Chapter 7, I investigate the effect of interfacial area on ignition in reactive multilayer systems. As will be discussed, these studies all further support and provide a better understanding of the condensed phase reaction mechanism.

1.5.3. Melt Dispersion Mechanism

The final of the possible reaction mechanisms to be discussed is the melt dispersion mechanism (MDM).[25,31,48] As described in brief above, the premise of this reaction pathway is the violent rupture of the oxide shell that coats Al-NPs, as shown schematically in Figure 1.17. This event has been theorized to be caused by volumetric expansion of the metallic core upon melting, which would lead to a high stress buildup in the still solid oxide shell. It follows, that for high heating rates, sufficient pressure could cause spallation of the core and shell. This material would be propelled forward and the Al would be readily able to react, which would drive high propagation rates. Considerable calculation and experimental analysis have been done to support this theory, much of which can be found in Reference 75 and is summarized in recent review article Reference 48. This includes a model used to calculate the amount of melt in the core needed to fracture the shell, which was found to predict experimental flame speeds in burn tubes. Given, these resources I will not go into much further detail on the theory.

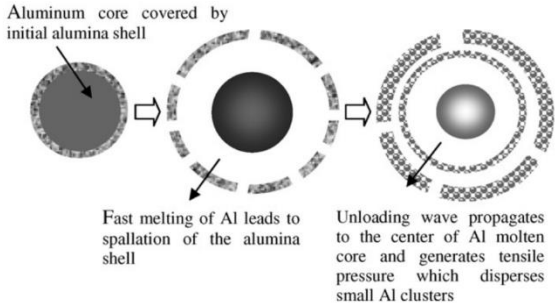

Figure 1.17. A schematic of the melt dispersion mechanism. Reprinted from Combustion and Flame, 156,Levitas, V. I., Burn time of aluminum nanoparticles: Strong effect of the heating rate and melt-dispersion mechanism, 543-546, Copyright 2009, with permission from Elsevier.

While this mechanism is fundamentally very different from the condensed phase discussed above, the two are not necessarily mutually exclusive. It is possible that one occurs when one set of experimental parameters are met and the other occurs under others. Alternatively, both could occur simultaneously, but with one dominating the overall process. For example, in the sample collection experiment by Jacob et al. discussed in the previous section, there were two size regimes for products.[24] It could be that the micron size particles were the result of condensed phase interfacial reaction, while the smaller nanoscale products resulted from MDM. Even if this small particle population only represents a small portion of the overall combustion, with MDM it could still be significant because of the high burn rate suggested by the theory.

However, there are several reasons why I find this mechanism to be an unlikely controller of nanocomposite thermite reaction. To start, there is all the evidence for the importance of the condensed phase reaction pathway discussed above. Further, several *in situ* studies, including my DTEM results to be discussed in Chapter 4 and Chapter 5 show no evidence for this phenomenon at heating rates of ~10^6 and ~10^{11} K/s.[16] While it has been argued that the former rate is below the threshold, those results were consistent with the higher heating rate experiments. Another potential issue is that the experimental support of MDM comes from burn tubes and taking the luminous front to be the reaction front,[48] but the recent work with partially filled tubes discussed above has shown that this may not be the case.[29,30] MDM also assumes perfectly spherical particles and shells, to allow for even stress loading. However, the most common commercial Al-NP synthesis methods allow for

significant agglomeration prior to the formation of the shell, which can produce necking and other irregularities in the shell.[76-78] One final limitation of MDM is that it does not provide any means for understanding the role of oxidizer size and composition, which has been found to be more important the fuel particle size for deterring flame speed.[12]

All of these issues are related to the notion that flame speed is directly proportional to how much melt is dispersed after spallation of the shell. Outside of that aspect, I do agree that the stresses in the particle upon melting of the core could lead to breakdown of the shell. However, rather than being a violent response, it seems more likely that the molten Al simply flows out, perhaps carrying along the Al_2O_3 pieces, which could explain the behavior observed during the *in situ* experiments mentioned.[16,54,79] This could explain how changing stresses within and damage to the oxide shell can effect performance, without necessitating melt dispersion.[80,81]

1.6. Summary and Motivation

The main points to take away from all the above discussion are as follows. First, nanocomposite thermites offer high energy densities and high reaction rates, which makes them desirable for a wide range of energetic applications. Second, the mechanisms that control combustion of these materials are not well understood. Reaction in particular could go through several different pathways, such as gas condensed heterogeneous or direct condensed phase reaction. Third, the challenging

nature of this combustion necessitates dynamic experimental systems capable of high heating rate.

With these in mind, it is the goal of this dissertation to use novel experimental techniques to probe nanocomposite thermite ignition and reaction. Of particular interest is the behavior of the material at the nanoscale, including the impact of dynamic morphological change and the role of interfacial area. I also address the impact that gaseous species have on combustion in terms of both secondary oxidation and heat transfer.

Chapter 2: Experimental and Computational Methods

2.1. Nanocomposite Thermite Sample Preparation

For most of the experimental procedures used throughout this dissertation, nanocomposite thermite powder samples were used for testing. As these materials are highly energetic and sensitive to ignition, careful handling and safety equipment were critical parts of sample preparation and use. For this reason, only small amounts (<100 mg) were produced at a time and handling of dry nanocomposite was minimized by keeping it in solvent (typically hexane) whenever possible. As nanoparticles have potential health risks,[82] it is also important to use a particle mask and gloves whenever handling them.

The nanocomposites were made by mixing nanoparticle fuels and oxidizers that were typically purchased from a commercial supplier (e.g., Sigma Aldrich, Novacentrix). Fuel and oxidizer were weighed out separately using a microbalance in a ratio based on the desired stoichiometry. For energetic composites, stoichiometry is generally discussed in terms of equivalence ratio, which is defined as $\varphi = \frac{m_{fuel}/m_{ox}}{(m_{fuel}/m_{ox})_{st}}$, where m_{fuel} is the measured mass of the fuel, m_{ox} is the measured mass of the oxidizer and the bottom ratio is for a the stoichiometric mixture. Thus φ=1 is a stoichiometric mixture, φ>1 is fuel rich, and φ<1 is fuel lean. In order to accurately reproduce the desired equivalence ratio, it is important to account for the oxide shell which naturally forms on nanoparticle fuels. For example, the Al-NPs used in much of this dissertation were only 70% active by mass, which means the remaining mass is oxide.

Once weighed, the nanoparticles were transferred to a glass vial. In order to intimately mix the two materials, the vial was filled with solvent (typically hexane or ethanol) and ultrasonicated (Branson 2510) for ~20 minutes. If the material was needed dry, the vial would then be left dry in a fume hood until all the solvent had evaporated. When handling dry, electrostatic discharge causing accidental ignition is a major concern, so it was important to make sure everything, including myself, was grounded. A blast shield visor and a protective sleeve for the glass vial was used for additional safety as well.

2.2. Temperature Jump (T-Jump) Heating

As was mentioned several times in the introduction, the heating rate plays a critical role in controlling the reaction mechanism of Al-NP based energetics.[21,22] Accordingly, it is important that the experimental methods produce rates that can simulate those found during free combustion. One technique used for this purposed is referred to as temperature jump (T-Jump), which can achieve rates of ~$5x10^5$ K/s. This approach uses a thin platinum filament (76 μm diameter) that is soldered to two electrical leads in a way that typically leaves a length of ~10 mm free between them. Then, using a custom built power supply, a tunable DC electrical pulse (~2-20 ms) is applied to the wire to achieve resistive heating up to ~1500 K. During the heating, an oscilloscope is used to directly record the voltage across the wire and record the current through a Tektronix AM 503 Current Probe Amplifier system. These values can be converted to a time resolved temperature using platinum's well-known relationship between resistivity and temperature.[83]

Sample can be deposited onto the wire through a variety of methods, including electrospray and sputter deposition. For powder samples, the most commonly used technique involved creating a weak suspension in some solvent (typically hexane or ethanol) and using a micropipette to extract a highly concentrated small volume. Droplets can then be produced on the tip of the pipette, which can be repeatedly run over the middle length of the wire to deposit the material.

2.2.1 Optical Emission and Ignition Studies

One experiment that can be performed with the T-Jump platform is the measurement of optical emission using a high speed camera (Phantom v12.1). Generally this camera was set to a resolution of 256x256, which allowed for a framerate of 67066 fps (1 frame every ~15 μs). The camera was set to trigger at the same time as the T-Jump heating pulse using a pulse generator (Stanford Research DG 535) so that the video could be directly correlated to the wire temperature. An example of this type of experiment is shown in Figure 2.1a. Using Matlab, the integrated intensity of each frame can be taken to create a plot of the integrated intensity with time as shown in Figure 2.1b. In order to account for any differences in wire length or distance from the camera, this data was always normalized by the peak intensity of a background run of the same wire heated again with the same pulse after the sample run. The sample run is the blue line, the background is the green line, and the red is the difference. The quantitative value of these plots is somewhat limited as it is dependent on the amount of material deposited and there is significant run to run variation in shape and peak intensity. However, the plots are highly useful for

gauging the order of magnitude of the reactivity and making qualitative comparisons between samples.

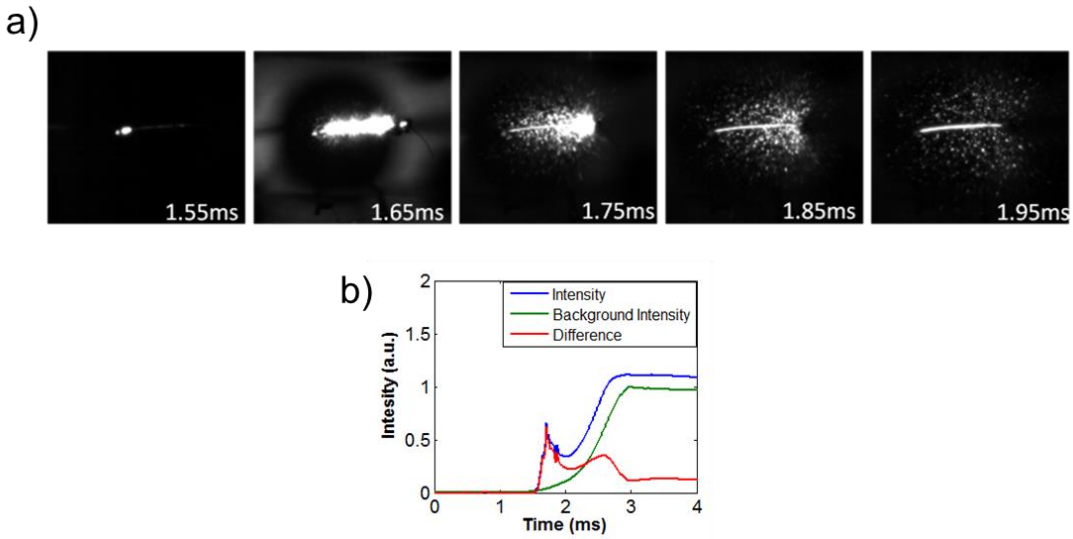

Figure 2.1. Example results from high speed video of a T-Jump experiment. Part a) shows frames from an Al/CuO nanocomposite heated at ~10^5 K/s. The first frame shows the point of ignition. The integrated intensity can be taken for each frame and plotted versus time as shown in the blue line of part b). The wire can be heated again to take the background intensity (green line), which is used to normalize the data and can be subtracted out to get the intensity generated by the sample (red line).

The primary use for this experiment is to determine the ignition temperature of a material. Ignition appears, as in the first frame of Figure 2.1a, as a discontinuous jump in intensity along the length of the wire and can also be observed as the onset of the signal in Figure 2.1b. As mentioned, the time of ignition observed in the video can be directly related to the wire temperature, to get the ignition temperature. This value is generally repeatable to +/-50 K, so multiple runs are required to get an accurate value.

This experimental setup can be run in a variety of environments using a pressurizable chamber. The chamber can be pumped down to 1 mTorr and then purged with whatever gas is desired. Oxygen and argon are common choices for

oxidizing and inert environments respectively or it can be left open to air. Alternatively the experiment can be performed in the vacuum of the mass spectrometer discussed in the next section.

Product collection is one other valuable experiment that can be performed with this T-Jump heating setup.[24] For this purpose, a carbon tape substrate can be positioned some distance (~2-4 cm) from the wire in order to collect material which is ejected from the wire. The high speed camera can be used to measure this distance and to observe the transit time of the material from the wire to the substrate. This product is then analyzed using SEM. The wires themselves can also be saved and analyzed, but the remaining material is not necessarily representative of the reaction product. This is because the wire takes ~100 ms to cool down after heating as determined through heat loss estimates and high speed video. Therefore material left on the wire will stay hot for much longer than it would in an actually combustion event.

2.2.2 Time of Flight Mass Spectrometry (TOFMS)

Nanocomposite thermites and their oxidizers produce significant gas during the heating and reaction process. To better understand how these gases evolve and what roles they play it is necessary to have an instrument that can probe these species with temporal resolution comparable to the timescale of combustion. The time of flight mass spectrometer (TOFMS) system used throughout this dissertation was developed within this research group with this goal in mind.[55,84]

A schematic and photo of this system is shown in Figure 2.2. This system works by ionizing the gaseous species in the vicinity of the T-Jump probe using an

electron gun typically set for 70 eV and 1 mA. Then a series of three plates are used to create an electric field which accelerates the ions up into the electric field free TOF tube. At the top of the tube, species are detected by a microchannel plate detector (MCP). As all the species are given roughly the same amount of energy by the applied voltage (assuming a single charge), the velocity of a species in the tube will be proportional to the square root of the 1 over the mass, since kinetic energy is equal to mass times the velocity squared (mv^2). Thus the time it takes for a species to travel the tube can be used to determine its mass. As calculation assumes that the species travel uninterrupted up the TOF tube, it is important to have the system under high vacuum (~10^{-7} Torr).

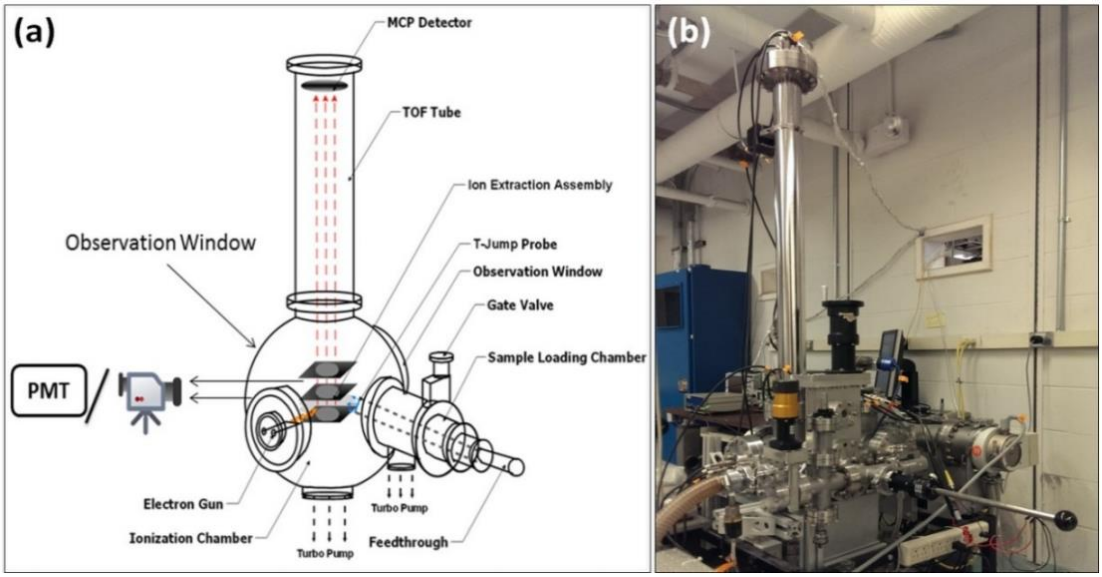

Figure 2.2. A schematic and photo of the TOFMS spec system are shown in a) and b) respectively. This figure is reproduced from Reference 85.

The process of ionization, acceleration, and detection is enabled by pulsing the voltage of the middle ion extraction plate. The bottom plate is always held at

ground while the top plate as well as the liner of the tube and the MCP are held at -1500 V. For the 3 µs ionization period, the middle plate is left at ground, which provides a field free zone for the electrons produced by the e-gun to ionize the gaseous species. Then, the plate is changed to -200 V, which prevents further ionization and establishes the field which accelerates the species. This process is repeated every 100 µs to produce spectra which are recorded with an oscilloscope that is triggered by the same source as the T-Jump heating and the highs speed camera so all the diagnostics are synced. A MATLAB code is then used to convert the TOF information into mass over charge. An example of the data produced by this instrument is shown in Figure 2.3.

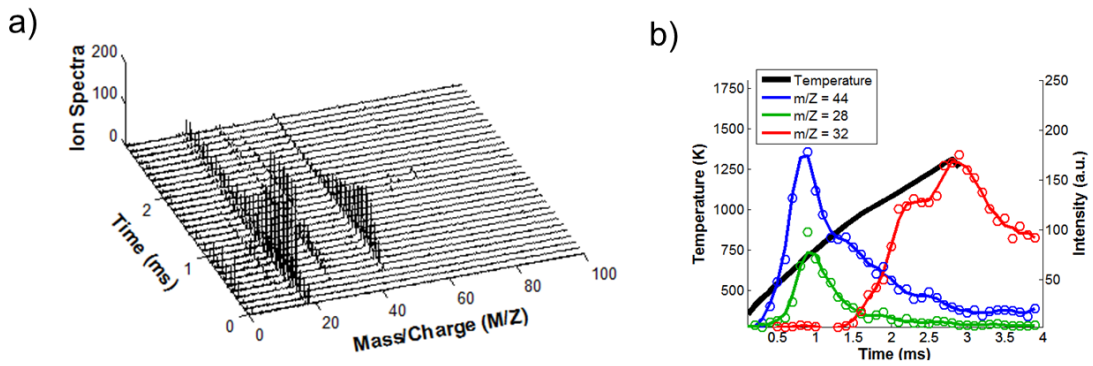

Figure 2.3. Example data from a T-Jump TOFMS experiment on CuO nanoparticles. a) shows a series of mass spectra (1 recorded every 100 µs) with time in a 3D plot. b) shows intensity of specific species with time, along with the temperature calculated from the voltage and current.

2.2.3. Magnetron Sputter Deposition onto T-Jump Wires

While the most common method of sample deposition for T-Jump experiments was touched on above, the set of experiments discussed in Chapter 7 required a more involved process. The goal was to incorporate the relatively simple geometry of reactive multilayers into the T-Jump system in order to study the effect

of interfacial area on the condensed phase reaction. Reactive multilayers, also known as nanolaminates, are typically produced through physical vapor deposition (PVD) by alternatingly depositing thin films of fuel and oxidizer.[15,61,86] This allows for a great deal of control over diffusion distances and interfacial density (interfacial area per unit volume or mass). For the T-Jump study, my collaborators Dr. Edward Mily and Dr. Jon-Paul Maria at North Carolina State University used a custom magnetron sputter chamber to deposit Al and CuO in alternating layers onto the Pt wires. A schematic of this chamber is shown in Figure 2.4. The two sputtering targets (Al and CuO) are positioned opposite each other with a shutter that can cover either. The wires are placed in the center of the chamber on a rotating stage (6 rpm) to allow for uniform coverage.

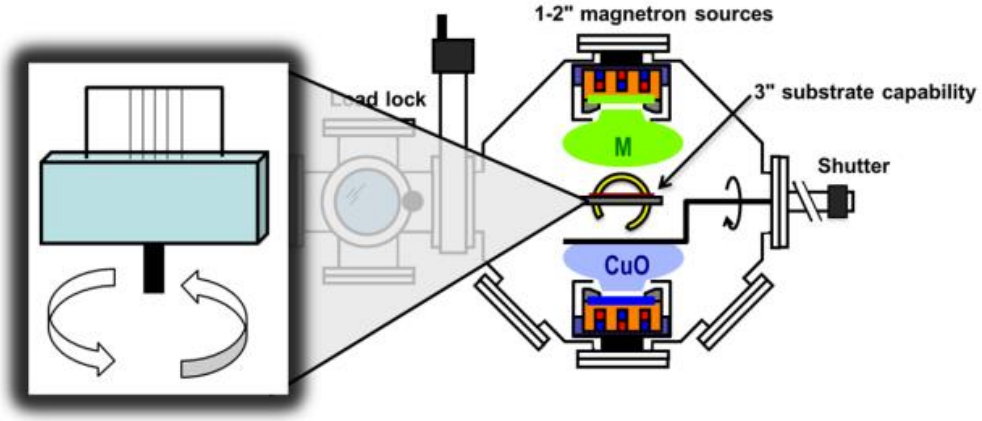

Figure 2.4. The sputter chamber designed and used at North Carolina State University by Dr. Edward Mily of the Maria group for magnetron sputter deposition onto the Pt wires used in T-Jump experiments. Figure reproduced from Reference 87.

Sputter deposition works by applying a negative bias to the sputtering target, which is typically made of the material one wishes to deposit. Inert gas (typically Ar) introduced into the vacuum environment will be ionized by the free electrons repelled

by the target. Upon ionization, the ions will be driven towards the target where atoms of the target material will be ejected towards the deposition substrate.[88] Magnetron sputtering adds a strong magnetic field to the system which traps the free electrons near the sputtering target which greatly enhances the probability of ionization of the gas and thereby greatly speeds up the sputtering process. Radio frequency (RF) sputtering can be used for nonconductive targets to prevent charge buildup in the target, which works by rapidly alternating the bias.

For T-Jump experiments the Pt wires in the center of the chamber were ~25 mm long and masked so that only ~8 mm in the center of the wire were exposed to the sputtering sources. This allowed for film free parts of the wire for soldering to the T-Jump electrical leads.

2.3. Constant Volume Combustion Cell

In order to better gauge the bulk reactivity of nanocomposite thermites, a constant volume pressure cell that had been previously designed to record optical and pressure signals was used.[45] This experimental setup provides a means of observing combustion, while still using a small enough amount so that it is safe to handle. A schematic of this experimental setup is shown in Figure 2.5. For an experiment, a small pile (~25 mg) of material is placed into the center of the 13 cc cell and ignited using NiCr wire, which is joule heated using a power supply. As this wire only heats part of the powder pile, the produced combustion event includes both reaction and propagation as would occur during free combustion. In the confined space, high temperature and gas production creates a pressure build up, which is observed with

the piezoelectric pressure transducer. Simultaneously, a tube lens array directs any produced light into a fiber optic cable which leads to a Si photodetector. The signals from both sensors are recorded by an oscilloscope which is triggered by the sudden increase in optical signal that occurs upon ignition.

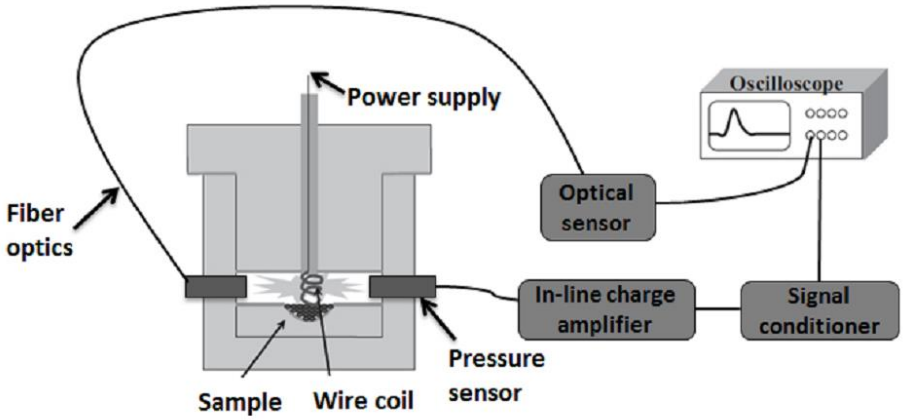

Figure 2.5. A schematic of the constant volume combustion cell setup. Figure taken from Reference 85.

An example of data taken with this set up was shown in Section 1.5.1 in Figure 1.7. A known calibration allows for the voltage signal recorded with the pressure transducer to be converted to pressure units. One of the most important aspects of combustion learned from this experiment is the timescale of the event. This property is quantified with the use of the rise times of both the pressure and optical signals, which are defined as the time of signal peak minus the time when the signal first reached 5% of its maximum. The full width at half the maximum (FWHM) of the optical signal is referred to as the burning time and is considered representative of the overall length of the event. Another important value is the pressurization rate, which is defined as the peak pressure divided by the pressure rise time. This value best

captures the overall reactivity of the sample and correlates to the flame speed observed in a burn tube.[9]

2.4.In situ Electron Microscopy

Electron microscopy is a critical technique for the study of nanoscale materials, since they possess features that are too small to resolve with traditional optical microscopes. Scanning electron microscopes (SEMs) build up an image by moving the electron beam to different locations all over the sample and detecting secondary and/or back scattered electrons in each spot. Transmission electron microscopes (TEMs) image the electron beam after it has been transmitted through a thin specimen.[89] SEMs are generally useful to resolve features ~10 nm and larger, while TEMs allow for atomic scale imaging. Both allow for elemental analysis using energy dispersive X-ray spectroscopy (EDS or EDX), which works by recording the energy of X-rays generated when the sample is excited by the electrons in the beam. TEMs also allow for additional characterization techniques, such as selected area electron diffraction (SAED) and electron energy loss spectroscopy (EELS). SEM images give a better sense for the topography of a sample.

2.4.1. Electrically Heated Sample Holder

The type of *in situ* electron microscopy experiments that are most useful to the study of nanocomposite thermites are ones which provide heat that can drive reaction and simulate the combustion environment with high heating rates. This can be achieved using the Aduro system from Protochips Inc., which allows for heating up to

1200 ºC at rates of ~10^6 ºC/s. The system is based on chips which can pass a current through a thin membrane that supports the sample. An example of a heating chip is shown in Figure 2.6a, where the gold electrical contacts are visible and lead to the transparent membrane in the center, which is the only part of the chip that heats up. Each chip is individually calibrated by the manufacturer and comes with a calibration file so that the software can provide a predefined current to achieve the desired temperature. These chips can be integrated into both TEM and SEM holders (Figure 2.6b and c respectively), which feature spring loaded electrical leads which hold down the chip and make the electrical connection. The support membranes are fabricated with an array of holes (illustration inset to Figure 2.6c) in order to facilitate TEM imaging. The chips is also covered with a thin film of either C or SiN that spans those holes and supports sample.

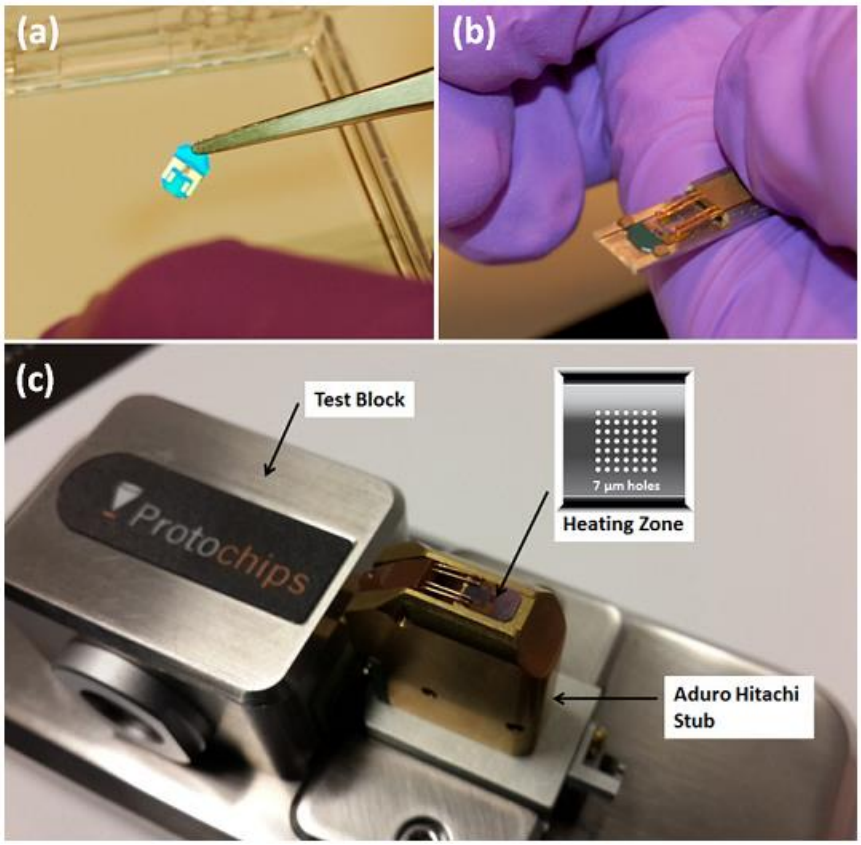

Figure 2.6. a) shows an example of the Aduro chips used in these experiments. b) and c) show a chip inserted into a TEM and SEM holder respectively. This figure was taken from Reference 85 with parts a), b), and the inset of c) taken from the Protochips website (http://www.protochips.com/).

A typical nanocomposite thermite experiment is prepared by using a micropipette to dropper of suspension of the material. Then the chips are ramped to the desired temperature and held for ~1 ms. This prevents quenching the material as the low thermal mass of the film leads to cooling at roughly the same rate as heating.

2.4.2. Dynamic Transmission Electron Microscopy (DTEM)

Electron imaging occurs on the order of ~0.5 s and longer. For TEM this limit comes from limitations in source brightness. To build up an image with sufficient contrast, the charge-coupled device (CCD) camera is exposed for longer to allow in more electrons. Thus in the fast heating stage experiments discussed above, only

before and after images are recorded. In order to image fast events with electrons, a group at Lawrence Livermore National Laboratory (LLNL) has developed a dynamic transmission electron microscope (DTEM), which uses short laser pulses to trigger electron generation from the TEM cathode.[90-94] The produced pulses of electrons are intense enough so that just one ~15 ns long pulse can create an image.

The system (an illustration of which is shown in Figure 2.7) is based on a JEOL JEM-2000FX that has been significantly modified for this purpose. A window and internal optics direct the UV (213 nm) laser up the Ta based cathode. Based on an arbitrary waveform generator (AWG), this laser can be shaped into a series of pulses with defined duration (typically 15-50 ns) and spacing. Through photoemission of the cathode, the UV pulses produce electron pulses of the same shape. These laser pulses are timed to a specimen drive laser which is used to heat the sample. The heating pulse is typically ~12 ns long, has a $1/e^2$ beam width of 135 μm, and has a wavelength of 1064 or 532 nm. Assuming the sample reaches ~1500 K, this corresponds to a heating rate of ~10^{11} K/s.

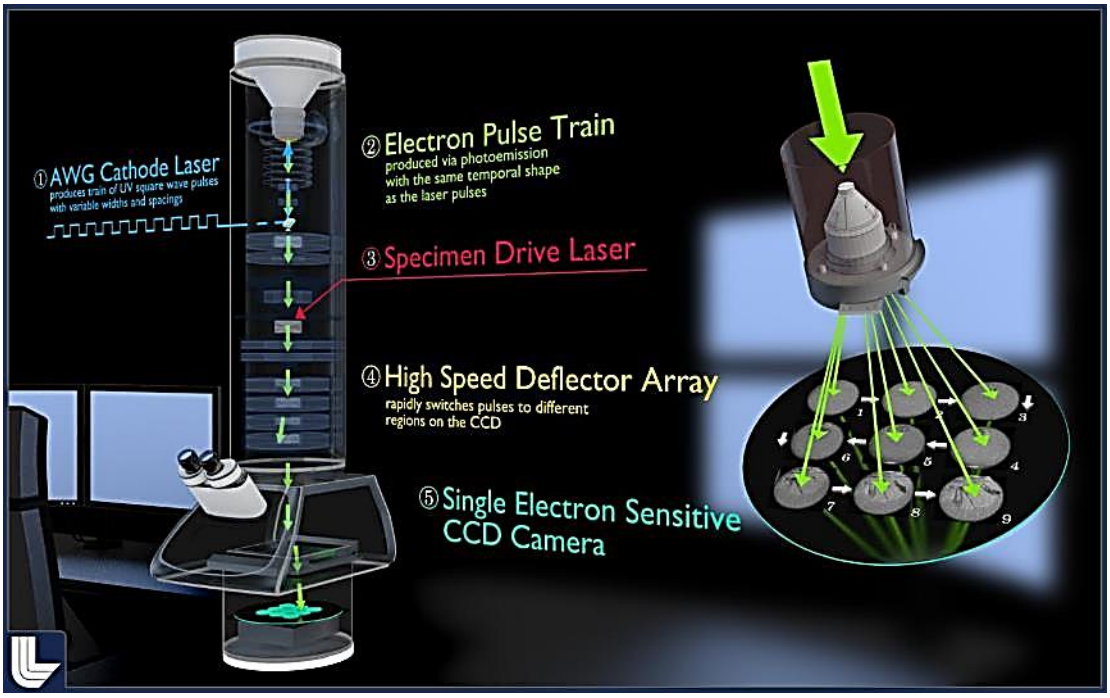

Figure 2.7. An illustration of the DTEM as it has been modified for movie-mode. Figure adapted with permission from Lagrange, T; Reed, B. W.; Masiel, D. J., Movie-Mode Dynamic Transmission Electron Microscopy, MRS Bulletin, 40, 01, 22-28, 2015.[94]

Originally this system operated in single shot mode, with a single time resolved electron pulse taken for each experiment. This limitation came primarily from the slow read out time of the CCD camera. To overcome this, a high speed deflector system was integrated into the system. This deflector is timed to the electron pulses in order to direct each pulse to a different location on the CCD in a 3 x 3 array, as shown on the right side of Figure 2.7. This produces 9 time-resolved sequential frames in what is essentially a movie. Thus this technique has been dubbed, movie-mode DTEM (MM-DTEM). For more detail on both single shot and movie mode DTEM, please refer to References 92-94.

Given the large number of electrons (~10^8-10^{10}) in each pulse, stochastic electron-electron scattering limits the spatial resolution. However traditional

continuous wave (CW) mode based on electrons generated by thermionic emission in the cathode can be used as well. Therefore, in the studies discussed in Chapter 4-Chapter 6, the procedure was to take before, during, and after images with pulsed mode as well as before and after images with CW mode. An example of such an experiment is shown in Figure 2.8.

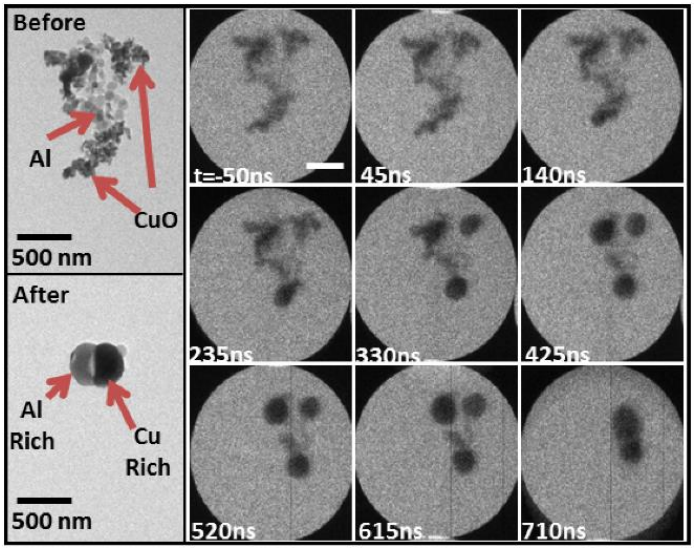

Figure 2.8. An example MM-DTEM experiment on Al-CuO. The before and after images were taken with CW mode. The 9 movie frames were taken with 15 ns pulses and the time listed is with respect to the peak of the heating pulse.

2.5. Equilibrium Calculation Software

Equilibrium calculations are a valuable tool for understanding the combustion products. The principle of this computation is to use the thermodynamic properties of all the possible species that could be produced by a system, to determine what state will be most stable. This calculation can be performed under a variety of conditions, but adiabatic (no energy lost to the environment) calculations are most common for energetic materials, as reaction tends to be far faster than heat loss to the environment. Under these conditions, the energy released by an exothermic reaction

will go into raising the temperature of the product, as well as any phase changes or decompositions. The final temperature calculated is referred to as the adiabatic flame temperature.[95] Typically, an additional assumption of constant volume or constant pressure is made. In the constant volume case, no work is done by the system, so energy is conserved. For constant pressure, work is needed to expand its volume and maintain the constant pressure, so enthalpy is conserved but not energy. Accordingly the adiabatic flame temperature of the constant energy and constant volume (UV) case will generally be higher than the constant enthalpy and constant pressure (HP) case. Along with temperature information, these calculation give the final product concentrations. Of particular interest for the study of nanocomposite thermites, is the gas production, as that has been shown to correlate well with flame speed.[10,96]

While such calculations can be done by hand if you assume a small number of products, software with large database of species make the process far simpler and more accurate. These programs work iteratively to minimize the free energy of the system while conserving all the chosen values. In this dissertation, CHEETAH 6.0 developed at LLNL was the most frequently used software. The JCZS library was used for all calculations because previous studies have found it to produce the best results for thermites.[10] NASA's chemical equilibrium with applications (CEA) was also used in certain cases when its library had a species not contained in the CHEETAH one.

Besides UV and HP calculations on energetics, TP (constant pressure and temperature) calculations can be useful for analyzing the decomposition behavior of a particular material. For example, testing CuO at a wide range of temperatures indicate

that it will remain stable through low temperatures, but will eventually decompose to Cu_2O and O_2. At higher temperatures it will decompose further to Cu and O_2.[45]

While calculations such as these are helpful for understanding the combustion process, it is always important to not take them entirely at face value and to carefully consider their real world relevance. In particular, one should think about if all the potential species are included in the library, if constant volume or constant pressure is more appropriate, and if non-equilibrium behavior could have a more significant impact on experimental results.

2.6. Thermogravimetric Analysis and Differential Scanning Calorimetry

Thermogravimetric analysis (TGA) and differential scanning calorimetry (DSC) are techniques that provide a wealth of valuable information on the behavior of energetic materials, but suffer from slow heating rates (~1-50 K/min). While they were not employed frequently in this dissertation, they are important enough to the field of nanoenergetics to warrant discussion. Both techniques work by subjecting the material to a prescribed temperature ramp, typically while flowing a gas over the material. Often, they are incorporated into a single instrument, such as the SDT Q600 from TA Instruments used by this group. TGA is based on accurately measuring the weight change in the sample while DSC measures the energy needed to reach the desired temperature of the sample in comparison to an empty specimen holder. This allows observation of a variety of different physical and chemical process. For example, oxidation of Al from a gas flowed over the sample will result in an

exotherm and weight gain, while melting will present as an endotherm with no weight change.

Chapter 3: Calculations on the Viability of Heat Transfer Mechanisms*

Summary

The combustion of nanothermites is a complex multiphase process that is still not well understood. One important aspect that is in need of further examination is the heat transfer mechanisms that drive combustion. Here, I present some simple calculations to critically analyze the viability of conduction, convection, and radiation mechanisms of heat transfer as it relates to reaction propagation in nanothermites. While convection has generally been accepted as the critical mechanism for heat transfer, I show that the movement of hot gases cannot account for the required energy flow. Instead, it is illustrated that the movement of condensed phase material plays the critical role in heat transfer and should be accounted for in future models.

3.1. Introduction

As was discussed in Section 1.3, there is good amount of experimental evidence that points towards a convective/advective heat transfer mechanism being dominant in nanocomposite thermite combustion.[7,10,13,27] That is, hot gases or other materials are being propelled by high pressure gradients into the unreacted zones where their heat is deposited. Despite significant support for this mechanism, it is not entirely clear whether hot gases or condensed phase material is most responsible for

* The results presented in this chapter have been previously published and are reprinted from: Egan, G. C.; Zachariah, M. R., Commentary on the heat transfer mechanisms controlling propagation in nanothermites. Combustion and Flame **2015**, 162 (7), 2959-2961 with permission from Elsevier

transporting this energy. Gases are far easier to conceptualize and model, but they do not generally hold much energy compared to condensed material. In order to better understand these possible mechanism, including the unlikely ones (conduction and radiation), I present here a series of straightforward calculations. These look at energy transfer rates and total energy content allowed through the various mechanism, which enables determination of a mechanisms viability. In doing so, I find that hot condensed phase material being advected forward is the only reasonable heat transfer mechanism.

3.2. Calculation

3.2.1. Calculation Parameters

To make this process as simple as possible, all the calculation parameters are derived from an Al/CuO burn tube experiment, which involves loosely packed material in a large length/diameter ratio tube.[7,10,27,29] When ignited, the pressure and/or luminous front can be observed as it propagates forward through unreacted material. For the calculation, I assume a tube with 3.2 mm inner diameter and packed to 6% theoretical maximum density of Al/CuO mixed to an equivalence ratio of 1.[10] To account for the oxide shell, the aluminum nanoparticles are assumed to be 70% active by mass. Therefore the reactant mixture is 17.1% Al, 75.6% CuO, and 7.3% Al_2O_3 by mass, and there is 2.4 mg of this mixture for every linear millimeter of packed tube.

In order for reaction to propagate, the cold and unreacted material must be heated to the point of self-sustaining reaction (i.e., ignition). For simplicity, I assume no exothermic self-heating occurs prior to this point, which is reasonable given the short times scales involved in the overall combustion process.[31] I also assume that ignition occurs at 1050 K as found in high heating rate (~10^5 K/s) experiments.[38] Based on the data in the NIST WebBook, the energy needed to raise the temperature of the reactants from 300 K to the ignition temperature is 1.5 J per linear mm of packed tube. [97] All of the values discussed so far can be found summarized in Table 3.1. From this base of values, it is possible to make estimates on the timescales and heating rates that can be achieved with the different mechanisms of heat transfer.

Material system	**Tube inner diameter**	**Packing density**	**Assumed ignition temperature**	Mass per unit length of tube	Energy needed for reactants to reach ignition temperature
Al/CuO	**3.2 mm**	**6% TMD**	**1050 K**	2.4 mg/mm	1.5 J/mm

Table 3.1. Parameters used in the calculations and estimations made in this section. Values in bold were chosen based on the experiments in References 10 and 38. The other values were calculated based on those parameters.

3.2.2. Conduction

I first address conduction based on an upper bound estimate of fully dense aluminum, which has a thermal conductivity of 237 W/mK.[98] From experimental measurements of pressure rise times and flame speeds, the reaction front thickness in a burn tube has been calculated to be 10 mm thick, which lines up reasonably well with values of 10-40 mm measured from temperature rises observed in pyrometry experiments.[7,29,99] From this, I estimate a thermal gradient of 2.7x10^5 K/m based on a temperature drop from 3000 K to 300 K over this distance. Fourier's law then gives a

heat flux of $6.4x10^7$ W/m^2, which when multiplied times the cross-sectional area of the tube gives 515 W. The maximum flame speed that could be achieved by this heat transfer can then be calculated by dividing that heat flow by the energy needed to reach ignition per unit length to give 0.34 m/s. This is orders of magnitude slower than the burn speeds typically observed in burn tubes (>500 m/s), and significantly slower than even those found for open configuration experiments (>5 m/s).[10,36] Additionally, consider that I assumed fully dense Al for conduction when, in reality, the porous nanoparticle beds found in these experiments have effective thermal conductivities an order of magnitude lower than bulk.[33,34] Additionally, inclusion of CuO, which has an order of magnitude lower thermal conductivity than Al, would have a similar detrimental effect. For a one order of magnitude drop in conductivity from bulk Al, a reaction velocity of 10 m/s, maintained by conduction alone, requires a reaction zone length (temperature drop distance) of just ~30 μm, rather than the ~10 mm observed in experiments. Therefore in the combustion of these materials, conduction cannot account for the observed flame speeds.

3.2.3. Radiation

For radiation, I again greatly simplify the system in order to find an upper bound for heat flow. While nanoparticles have high specific surface area, during combustion they are surrounded by many equally hot particles. So for heat transport, the only radiation that will matter is that which travels forward into unreacted material. Therefore I can reduce the problem to just two cylinders of material with radiation passing through the presenting ends. If I assume black bodies with one hot (3000 K) and the other cold (300 K), then the heat flow can be calculated from the

Stefan-Boltzmann law as $\dot{\boldsymbol{Q}}_{\mathbf{rad}} = \boldsymbol{\sigma A}\left(\boldsymbol{T_1^4 - T_2^4}\right)$ where σ is the Stefan-Boltzmann constant and A is the cross-sectional area of the tube. This yields a radiative heat flow of just 37 W, which is an order of magnitude less than what was found for conduction and implies an even slower flame speed. Again, this is an upper bound, since in practice the local temperature difference would be less extreme.

3.2.4. Convection of Gases

In the previous two sections, I used timescale arguments to rule out conduction and radiation. For the remaining sections, I will focus on the amount of energy transferred by moving material from a hot region to an equal volume cold region. Equilibrium calculations have shown that the Al/CuO nanothermite reaction can produce ~4 mol/kg of gas, which is >95% Cu vapor.[10] This corresponds to 9.6×10^{-6} mol in a 1 mm long section of burn tube. Now if I assume that this gas is moved forward from the hot reacted zone to a cold unreacted zone, it transfers heat in equilibrating with the new zone and cooling down. Here I will neglect condensation, which will be addressed separately below, and use the constant pressure heat capacity of Cu vapor from the JANAF tables. The constant volume heat capacity may be more relevant, but C_p is higher than C_v and I want an upper bound estimate. Based on these assumptions, the process of cooling 3000 K Cu vapor to the 1050 K ignition point, liberates 0.4 J/mm which is only 27% of the 1.5 J needed for an equal volume of reactants to reach the ignition temperature.

It has also been suggested that, rather than Cu vapor, intermediate species (O_2 primarily) could drive the initial pressurization observed during combustion.[12,45,55,100] As diatomic gas molecules have higher heat capacities, this point is worth

considering. As these species are non-equilibrium, I use results of Al/CuO burn tube experiments that have observed pressures of ~1900 PSI (130 atm) and temperatures of ~3000 K [10,29]. Therefore based on the assumed tube diameter, a 1 mm section at those conditions will contain $4.2x10^{-6}$ mol of gas based on the ideal gas law. Assuming this gas is entirely O_2, cooling it in the manner discussed above liberates only 0.3 J/mm, or 20% of the ignition threshold energy, and less than that generated assuming equilibrium conditions. Based on these results, it is not accurate to model heat transfer as nanoparticles sitting in a hot gas, since the gases produced do not have enough thermal mass to make this process feasible.

Another process that must be considered in the transport and cooling of gases is that they typically contain a significant portion of condensable metal vapor, as mentioned above. Returning to the equilibrium calculations, the ~4 mol of copper gas per kg of reactant produced at constant pressure (1 atm) will liberate heat when condensed.[10] Using the heat of condensation of copper gas (~300 kJ/mol) yields 2.9 J/mm, which is ~190% of the ignition threshold energy.[97] Thus the condensation of copper could theoretically account for all the necessary heat transfer of combustion. However, there are several other factors that reduce the impact of this process and make it unlikely to be the dominant mode of energy transport.

First, the assumption of 1 atm constant pressure is erroneous because, as discussed above, pressures of ~1900 PSI (130 atm) have been recorded for Al/CuO in burn tubes. These extreme pressure waves indicate that gases are generated faster than they can dissipate, which means that constant volume calculations are likely more realistic. Under a constant volume constraint, equilibrium calculations for

Al/CuO at 6% TMD give just 0.31 mol of copper gas per kg of reactant. This only liberates 0.2 J/mm, which is only 15% of the energy needed to reach ignition.

Furthermore, copper vaporization is the last step in the reaction, and it is this that limits the adiabatic flame temperature to the Cu boiling point (2840 K at 1 atm). Therefore, the equilibrium concentration of copper vapor will only exist when the reaction is 100% complete. So for this gas to participate in heat transfer, reaction must occur significantly faster than the heat transfer. However, this does not seem to be the case as material in extended burn tubes has been found to burn for ~3 ms.[30] In comparison, flame speeds have been found to be >500 m/s in burn tubes and >5 m/s in open configurations.[10,36] If I assume a 10 mm reaction zone, this corresponds to propagation timescales of 20 μs and 2 ms. This implies that propagation occurs much faster than, or at least on a similar timescales of reaction, which means that it is likely that a significant portion of the equilibrium concentration of copper vapor is not available to participate in heat transfer. Similar observations are part of what led to the suggestion that intermediate gaseous species could drive pressure rise as discussed above.[12,45,100] This is further supported in Chapter 8, where the intermediate gas production of Al-Cu_2O is found to be far more significant than the equilibrium gas production.

Finally, I have assumed that 100% of the gases produced move forward into unreacted material, which is clearly not the case for open configurations for which this analysis is equally valid.

Thus, I conclude that neither straight convention nor heat of condensation of metal vapor can account for the totality of the heat transport necessary to support

combustion. While these calculations were based on Al/CuO, the impact of gases should be commensurate or even diminished for other thermites as Al/CuO is one of the highest gas producing thermites on a mol/kg basis.[101]

3.2.5. Convection of Condensed Phase Material

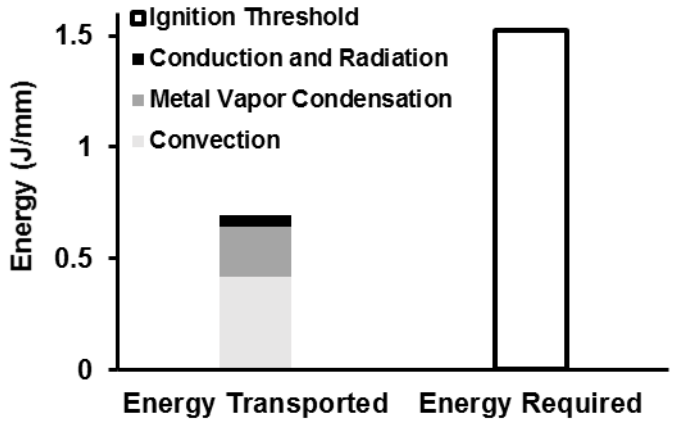

Figure 3.1. Estimated energy available from each form of heat transfer compared to the ignition threshold for 1 linear mm of burn tube material. Note that conduction and radiation were analyzed in terms of rates above, so the energy plotted is the amount delivered in 0.1 ms. That corresponds to the characteristic time for 1 mm of material and a flame speed of 10 m/s. Higher flame speeds will correspond to shorter times and even less energy. The value shown for condensation of Cu is based on the amount of vapor found for a constant volume 6% TMD equilibrium calculation.

The preceding results are summarized in Figure 3.1, which takes the reasonable upper bound measurement for each mode of heat transfer discussed so far. For metal vapor condensation, the absolute maximum was considered implausible as discussed above, so the constant volume approximation was used instead. This figure clearly illustrates that the critical ignition threshold cannot be reached by the modes of heat transfer discussed so far. The one mechanism that remains is the movement of hot solid and molten material. Such behavior has been suggested previously. For example, with Al/MoO_3 it was observed that peak flame speed coincided with the highest production of gas above the melting point of Mo, which indicated that molten

metal was important to propagation.[35] Additionally in an open configuration, material was observed to have been thrown forward and to have ignited the unreacted material discontinuously.[36] Such behavior is not entirely surprising given the small stokes numbers of the nanoparticles will lead to significant entrainment.[30]

To give this process a similar treatment to the previously discussed heat transfer mechanisms, I examine the transport and cooling of molten Cu and Al_2O_3 from 3000 K to 1050 K (including solidification), which liberates 77 kJ/mol and 410 kJ/mol respectively.[97] The 2.4 mg/mm in the tube corresponds to $2.3x10^{-5}$ moles of Cu and $7.7x10^{-6}$ moles of Al_2O_3 per linear mm of burn tube. Therefore, to achieve the 1.5 J/mm necessary for ignition, only 31% of that quantity must transported. While the transport of condensed phase material has as yet not been quantified by experiment, recent work does show that a small compact of reactants can expand >1.5 meters down an unfilled tube before burnout.[30] The long burn times (~3 ms), relative to the initial expansion, observed in that experiment suggest that a mechanism involving the fast release of intermediate gaseous species causes pressure buildup and unloading that propels hot material forward, which then continues to burn. This result suggests that heat transfer involving the movement of condensed phase material offers a reasonable explanation, particularly after consideration of the other possible heat transfer mechanisms, to explain the high propagation velocities observed in nanothermites.

3.3. Conclusions

In this work, I have, based on scaling arguments, ruled out conduction and radiation as significantly contributing heat transfer modes for the propagation of nanothermite combustion. I also showed that the convection of gases alone is unlikely to account for all the energy transported, even after accounting for metal vapor condensation. While these mechanisms undoubtedly contribute to combustion, these results indicate that the movement of condensed phase material will play a dominant role.

Acknowledgements

This work was supported by the Army Research Office and the Defense Threat Reduction Agency.

Chapter 4: *In Situ* Imaging of Loss of Nanostructure in Aluminum Nanoparticle Aggregates with Nanoseconds Temporal Resolution*

Summary

The word "nanoparticle" typically elicits a vision of an isolated sphere; however, the vast bulk of nanoparticulate material exists in an aggregated state. When such particles are exposed to high temperature and rapid heating conditions, they become susceptible to morphological changes which can reduce surface area, often to the detriment of functionality. Here, I report on thermally-induced coalescence which can occur in aluminum nanoparticle aggregates subjected to rapid heating (10^6-10^{11} K/s). Using dynamic transmission electron microscopy (DTEM), I observed morphological changes in nanoparticle aggregates occurring in as little as a few nanoseconds after the onset of heating. The time-resolved probes reveal that the morphological changes initiate within 15 ns and are completed in less than 75 ns. The morphological changes were found to have a threshold temperature of about 1300 ± 50 K, as determined by millisecond-scale experiments with a calibrated heating stage. The temperature distribution of aggregates during laser heating was modeled with various simulation approaches. The timescale of this loss of nanostructure process was far faster than any found for Al combustion, which implies that it could have a significant effect on reactivity.

---

* The results presented in this chapter have been previously published and are reprinted with permission from: Egan, G. C.; Sullivan, K. T.; LaGrange, T.; Reed, B. W.; Zachariah, M. R., *In situ* Imaging of Ultra-fast Loss of Nanostructure in Nanoparticle Aggregates. Journal of Applied Physics **2014**, 115 (8).

I would like to thank my co-authors in that paper for all their hard work and input that made the paper and this chapter possible.

4.1. Introduction

While there are many processing methods that form isolated nanoparticles,[102,103] aggregates are prevalent in many applications as both intentional assemblies for beneficial properties[102] and unavoidable artifacts of most commercially viable synthesis techniques.[76,78,104,105] Although stabilizing agents can be used to mitigate aggregation, they typically decompose or volatilize at elevated temperatures.[106-108] While particle size is commonly reported as the average size of the primary particles, the behavior, be it mechanical, optical, or chemical, of nanoparticulate material will likely be impacted by the size and morphology of the aggregates. Furthermore, in high temperature applications aggregated nanoparticles will be thermodynamically driven to coalesce (or sinter)* to produce characteristically larger particles which, depending on the material properties and transport time scale of this process, could be rapid and precede the intended nanomaterial dynamics. While coalescence may be desirable in certain applications, such as bottom-up fabrication[109,110] or as a sensing method,[111] for many other applications, which demand a large surface to volume ratio, the loss of surface area caused by coalescence will decrease a material's effectiveness.[102,103] Whether one is trying to exploit or prevent coalescence and sintering, it is important to have a good

* The process discussed in this paper involves core-shell particles and the transport involving both liquid Al and solid Al2O3. As a result, the strictest definitions of both sintering and coalescence are not fully descriptive of the coarsening mechanism. However, I feel coalescence is a broader term and thus it is primarily used to refer to this process

understanding of the mechanisms, including the threshold temperature, the time scale, and the effect of aggregate size and morphology associated with this process.

While there has been extensive study of sintering mechanisms at moderate temperatures and over long periods,[106,107,111-113] these results are not necessarily scalable to much higher heating rates where the time scale of thermal and mechanical relaxation may become comparable, or even slower than, the characteristic heat transfer time scale. This becomes a concern in applications such as those involving optical excitation[114,115] and exothermic reactions,[3,16,22,116] where materials are subjected to rapid heating and will thermodynamically be driven to coalesce to minimize the free energy through the reduction of surface area. In such cases, the transient evolution is poorly understood due to the experimental difficulties associated with probing the very small length and time scales inherent to these processes. As a result, not much is known about the dominant mechanisms governing aggregate coalescence in this regime, or their individual time scales. Recent advances in *in situ* diagnostic techniques, such as dynamic transmission electron microscopy (DTEM),[90,117-119] have enabled the visualization and measurement of phase transitions and nanostructural evolution on otherwise unachievable length and time scales. Further, since DTEM utilizes laser heating, very rapid (10^{11} K/s) thermal heating rates can be applied. Thus, the technique is well suited to probe the processes associated with nanoparticle coalescence and sintering under rapid heating.

For this study, aluminum nanoparticles (Al-NPs) serve as a valuable and interesting test material, because of their wide availability and common use in a variety of material applications such as hydrolysis, sensing, nanocomposites, and

solar cells.[120-124] However the primary interest in this material in regards to this dissertation is its use as a high energy density fuel in combustion, propellants, or explosive formulations.[3,58,125,126] In these applications, aluminum particles undergo rapid heating, and it is critical to understand the onset temperature and time scale of coalescence, as these parameters will directly impact the mechanism of oxidation. For example, if the coalescence time scale is significantly faster than the combustion time scale, then aggregates will coalesce prior to combustion. This would warrant the need for a different combustion model than if the aggregate burned as an ensemble of individual nanoparticles. When exposed to air, aluminum particles form a 2-5 nm amorphous oxide shell.[3,22,23,58,125,126] While such thin oxide layers are common to most metal particles, and often insignificant on large scales, they can dominate the behavior when the particles are small and the shell is a substantial fraction of the volume. Aluminum has a melting temperature of 933 K, while the aluminum oxide melts at 2327 K. Upon melting, the aluminum will undergo a volumetric expansion (~6 vol%), while the oxide shell will remain solid. The resultant mechanical and thermal stresses will govern the material's behavior – a point that has led to conflicting opinions about the material dynamics occurring upon rapid heating.[22,23] In particular, it has been theorized that these stresses can induce material rupture in a process termed melt dispersion, leading to the unloading of high-velocity molten aluminum droplets which can then be oxidized.[22] The thermal ramp ($>10^6$ K/s) provided by DTEM can allow for the direct experimental examination of these theories.

Herein, I report on the in-situ heating of aluminum nanoparticle aggregates at rates of 10^6-10^{11} K/s, and the morphological changes that result. The use of DTEM allows for both qualitative visualization of the nanostructural evolution of aggregates and direct measurement of the time scale associated with this process. Modeling and more conventional *in situ* TEM measurements are also included and provide a more straightforward measurement of the temperature dependence. The results are used to draw conclusions about the onset temperature, time scale, and possible mechanisms driving the coalescence event in core-shell nanoparticle aggregates. In particular, I show that the sudden rupturing and dispersal necessary for the melt dispersion mechanism does not occur even up to heating rates much higher than those typical of combustion.

4.2. Experimental Details

Samples were prepared by adding ~5 mg of Al-NPs (80 nm primary particle size, Novacentrix) to a vial with 10 mL of ethanol. Previous thermogravimetric analysis measured the active content of the Al to be 73 wt%, with the other 27 wt% representing the oxide shell. The slurry was ultrasonicated for several minutes and then pipetted onto a TEM grid. Two types of support were used: Formvar-coated copper grids and silicon nitride membrane grids (SPI supplies).

Experiments were performed using the dynamic transmission electron microscope (DTEM) at Lawrence Livermore National Laboratory (LLNL), the details of which have been previously reported[90,117-119] and are discussed in Section 2.4.2. Note that movie mode as not operational at the time of this study so single shot mode

was used. The DTEM is a TEM equipped with a pulsed laser which strikes the cathode and leads to the photoemission of ~10^9 electrons, allowing an image to be captured within the ~15 ns duration of that pulse (roughly equal to the pulse width of the cathode laser). A second sample drive laser (1064 nm wavelength) was used to induce rapid heating of the sample, and this was synchronized with the electron pulse plus or minus an adjustable delay. Zero delay corresponds to the time when the peak intensities of both pulses are coincident at the sample. Due to the limited electron source brightness and stochastic electron-electron scattering during transit down the TEM column, the images taken with these 15 ns electron pulses are inevitably less resolved than an image taken with a continuous wave (CW) thermionic source used in conventional TEM. While this is a necessary sacrifice for temporal resolution, the spatial resolution of the pulse images is sufficient to observe the morphological transition of interest to this study. However, as the DTEM is capable of operating in both modes (pulsed and CW), images were also taken in CW mode to provide detail on the finer structural changes of the samples.

Further experiments were performed with the Protochips Inc. Aduro stage with silicon nitride coated e-chips, which allowed for *in situ* heating at rates up to ~10^6 K/s (discussed in Section 2.4.1). Modeling of the aggregate temperatures was also performed using both T-matrix[127,128] and finite element approaches. The details of this can be found in the Supplemental Information (Sections 4.S.2 and 4.S.3).

4.3. Results and Discussion

The general effect of high heating rates on the morphology of Al-NP aggregates can be seen with the CW images in Figure 4.1, which show an aggregate heated *in situ* with 12 ns laser pulses (~10^{11} K/s). Figure 4.1 (a) shows the aggregate of approximately 100 nanoparticles with average size of 80 nm prior to heating, and Figure 4.1 (b) shows that aggregate after a single heating pulse. Each subsequent image (Figure 4.1 (c)-1(h)) shows the morphological evolution of the aggregate after an additional laser pulse. As can be seen from these images, the heating led to significant morphological changes in the aggregate which can be described as the coalescence of the discrete nanoparticles into larger structures. This change in size corresponds to a loss of surface area, which is estimated to be ~40% from Figs. 1(a) to 1(b) (see Section 4.S.1 for the details of this estimation-Supplemental Information). This process continues through the rest of the series of pulses but with markedly diminished amounts of change after each additional pulse. Compared to that initial loss of 40%, the subsequent total loss only reaches 65% up through Fig. 1f, after which continued heating resulted in the loss of mass by evaporation. As a point of reference, complete sintering of the aggregate into a single sphere would correspond to roughly a 78% loss in surface area (i.e. with $n_1 \sim 100$ and $n_2 = 1$, as defined in the Section 4.S.1-Supplemental Information).

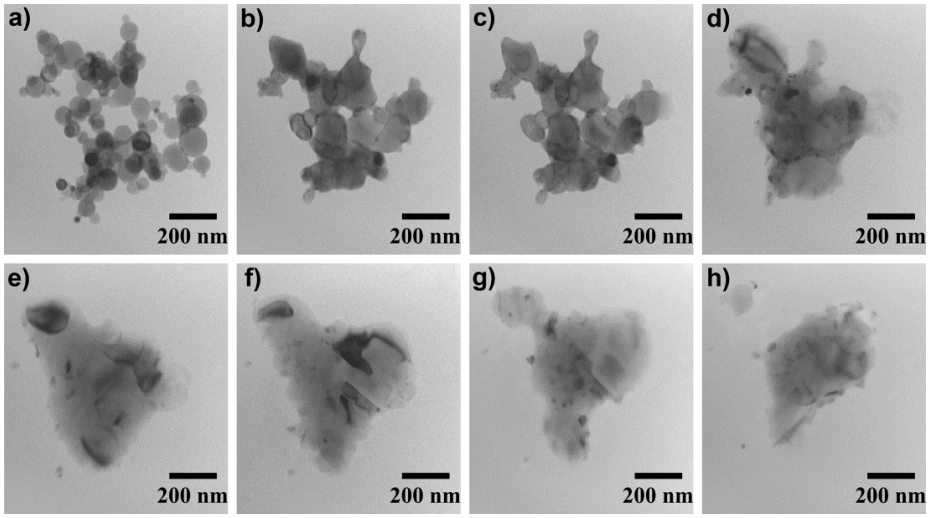

Figure 4.1. An aggregate of Al-NPs before (a) and after (b-h) successive heating with 12 ns laser pulses with fluence 1.23 kJ/m^2. Images were taken with the DTEM in CW mode with long pauses between pulses for the taking of the micrographs.

Time-resolved experiments were conducted by acquiring three pulsed mode images of the aluminum nanoparticle aggregates; before laser heating, during heating, and after cooling to visualize the final morphology. Complementary conventional CW TEM images of the clusters were obtained before and after laser heating to assist the interpretation of the pulsed mode images. Such experiments were performed on multiple sample regions, containing a total of ~50-100 such clusters for each of the various experimental parameters to establish a reasonable sample size. Figure 4.2 is a series of time-resolved images and micrographs taken in CW mode (Figure 4.2(a,b)), showing the change in the nanostructure character of the aggregate before and after heating with a single laser pulse. The laser fluences for these experiments (1.52 kJ/m^2) were slightly higher than those used to produce Fig. 1 (1.23 kJ/m^2), leading to a higher degree of coalescence. After one pulse, most of the aggregate's nanostructure character has been lost, reducing the surface area by approximately 68% (details are described in Section 4.S.1-Supplemental Information). Though having low signal to noise ratios,

the time resolved images of Figure 4.2(c-e) show the general trend in coalescence behavior with rapid pulsed laser heating and can be compared with conventional TEM images in Figure 4.2(a,b). Within the 12 ns period of the laser pulse (i.e., 0 time delay in which the temporal peaks of the electron and laser heating pulses coincide at the sample position), the cluster undergoes significant coalescence and loses its nanoscale features. The type of experiment shown in Figure 4.2 was repeated with various delays, ranging from -20 ns to 150 ns. As expected, at times before -10 ns, no coalescence was observed, confirming the calibration of time zero. For delays 75 ns and greater, no significant morphological differences were observed between the intermediate and after images, indicating that coalescence completes in less than 75 ns for a single shot.

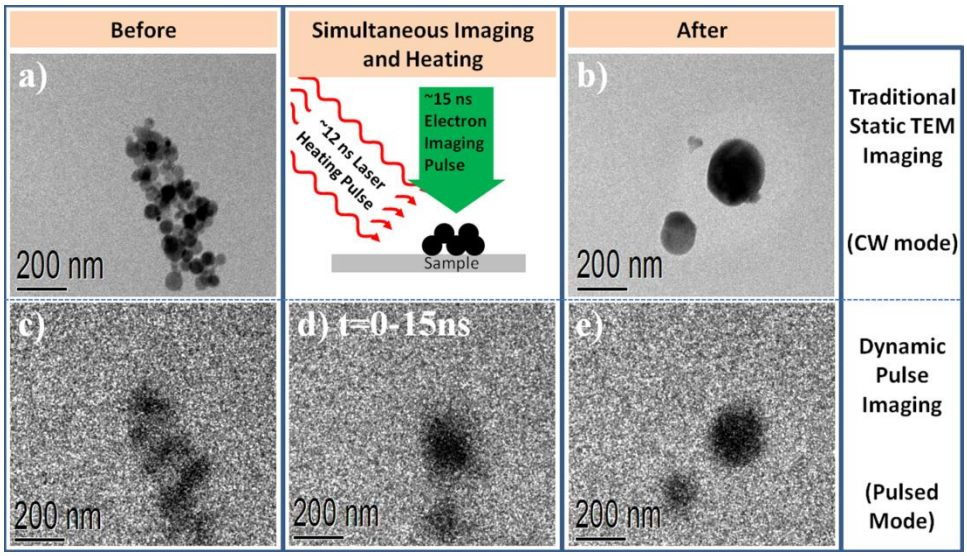

Figure 4.2. An aggregate of Al-NPs before (a,c), during (d), and after (b,e) a 12ns sample drive laser pulse of 1.52 kJ/m^2. Images a and b were taken with the DTEM in CW mode and images (c-e) were taken with time resolved pulse mode. The intermediate image (d) was taken with a 0 ns delay from the initiation of the heating pulse

Complementary to the laser heating experiments, *in situ* TEM studies of nanoparticle coalescence were also performed using a high heating rate TEM stage based on small-mass micromachined heaters (Aduro, Protochips Inc.). As described

in Section 2.4.1, this system resistively heats a silicon nitride (SiN_x) substrate at rates as high as 10^6 K/s. Samples were heated to various temperatures at 10^6 K/s, held at temperature for 1 ms, and then quenched, cooling at approximately the same rate. Interestingly, the threshold temperature for coalescence was not the melting point of either the aluminum core (933 K) or the oxide shell (2327 K) but an intermediate temperature of 1300 +/- 50 K in agreement with previous work.[16] Figure 4.3(a,b) shows the before and after images of a sample heated to 1173 K. Several particles show a large change in contrast after being heated, consistent with melting and resolidification of the aluminum core, though there was no indication of significant coalescence. Only upon heating to temperatures of 1323 K (Figure 4.3(c,d)) were notable morphological changes observed, with multiple particles coming together to form larger particles in a manner qualitatively similar to Figure 4.1.

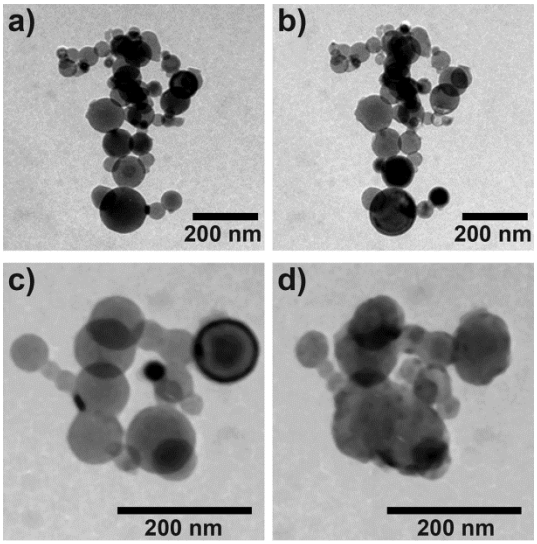

Figure 4.3. Two aggregates of Al-NPs before (a,c) and after (b,d) heating with the hot stage to high temperatures and being held there for 1 ms. The aggregates in (a,b) and (c,d) were heated to 1173 K and 1323 K respectively. The images were taken with the DTEM in CW mode. Note that for images (a,b), while no coalescence occurred, there were significant changes in contrast (most obvious in the group of 5 nanoparticles towards the bottom of the images) which suggests that there was melting in the metal cores. This is in contrast to images (c,d) where significant morphological change is obvious.

While having a threshold temperature at relatively low heating rates provides a lower bound estimate for the coalescence temperatures involved with the laser heating experiments, a deeper understanding of aggregate temperature is desired. To this end, several approaches were employed to model the laser absorption process. While the optical properties of aluminum are well known,[129] the near-field interaction of the light with the fractal aggregate shapes and support films can be complex and non-uniform[127] making accurate temperature data difficult to calculate. This type of interaction leads to local enhancement in absorption[127] and can cause hotspots in the aggregate which could act as initiation points for sintering. The necessity of these hotspots is revealed by first considering the aggregate as a group of non-interacting isolated spheres and calculating their absorption through Mie theory. This approach gives peak temperatures of only 550K, well below both the melting point of Al and the observed 1300 K threshold for sintering.[16] To understand the absorption of the aggregate on the whole, Mackowski's Multiple Scattering T-matrix Code[127,128] for generalized fractal aggregates was employed. Modeling details and theory can be found in the Section 4.S.2-Supplemental Information. This modeling showed the range of absorption efficiencies that exist in an aggregate, with those particles in the most densely packed areas absorbing far more than the rest.

To correlate absorption hotspots with spatial variation in temperature, one must account for heat transfer between particles and to the supporting film within the period that the nanosecond pulse hits the sample, as well as for other factors not considered in the T-matrix calculation, such as the oxide shell. For this, finite-element simulations in COMSOL™ were employed. While corroborating the need for

multiple particles and hotspots to reach the sintering threshold, these simulations showed that peak temperature was highly dependent on both the exact sizes and shapes of the gaps between spheres (see Figure S4.3(b)) and the laser absorption properties of the substrate. Further, the oxide layer was found to have an effect, albeit a relatively small one. More detail on these results can be found in the Section 4.S.3-Supplemental Information.

The models are in good agreement with the experimental results and help explain why, under the same heating pulse, larger aggregates were far more likely to coalesce than small (<10 particles) aggregates, such as in Figure 4.4. This is likely because larger aggregates have more particle-particle interfaces and are much more likely to feature hotspots and will, relative to their masses, lose heat to the substrate much more slowly. However, the model results also indicate that the laser absorption and peak temperature change can only be predicted to a fairly rough approximation, with values varying by a factor of ~2-3 or more depending on the details of the size and shape of the Al-NP aggregate, the precise geometry of the hot spots, and the contact points between the aggregate and the substrate. While these quantities can be determined experimentally to some extent, for example by tomographic reconstruction, the nanometer precision required for characterization of the hot spot geometries is exceedingly challenging. Indeed this wide variation in temperature response is supported by the experimental observation which shows superficially similar aggregates behaving differently when exposed to identical laser pulses (see Figure 4.4). However, I can still estimate upper bound temperatures using the T-matrix calculation for a specific aggregate with the assumptions that there are no

spaces between the metallic spheres (i.e. they meet at tangent points, which maximizes the intensity of a hot spot assuming all particles are spherical) and that heat loss to the substrate is negligible on the 12 ns time scale of heating. By this metric, the upper bounds for the temperatures achieved for the aggregates in Fig. 1 and Fig. 2 are 1310 K and 1690 K, respectively. The details behind these calculations can be found in the Section 4.S.2-Supplemental Information.

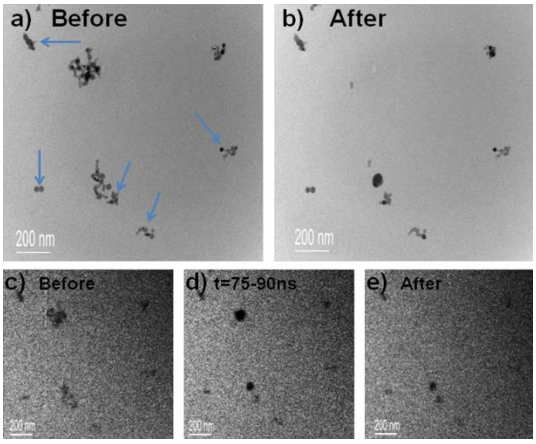

Figure 4.4. Aggregates of Al-NPs before (a,c), during (d), and after (b,e) a 12ns sample drive laser pulse of 1.52 kJ/m^2. Images (a,b) were taken with the DTEM in CW mode and (c-d) were taken with time resolved pulse mode. The intermediate image, B, was taken with a 75 ns delay from the initiation of the heating pulse. These images illustrate the disparate response of aggregates to the same heating pulse, and how large aggregates are far more likely to coalesce than the smaller ones. The arrows indicate aggregates that did not change from the heating laser pulse.

These results allow us to draw some conclusions about the sintering behavior of Al-NPs. Foremost is that coalescence begins within ~10 ns of the onset of rapid heating and is essentially complete within ~50 ns. The threshold temperature for sintering at high heating rates is 1300 K, which is between the melting points of the metal core and the metal oxide shell. This result provides direct experimental evidence that the volumetric expansion upon melting is not sufficient to cause spallation of the aluminum oxide shell. Also, the lack of any evidence for spallation

and the qualitatively similar results for both laser and resistive stage heating, despite the several orders of magnitude difference in the heating rates, conflicts with the occurrence of the melt dispersion mechanism.[25,31,48] Alternatively, sintering may result from aluminum diffusing through or into the oxide shell along with oxygen diffusing into the core.[46,49] This could produce a reduced oxide, thereby softening the oxide shell and lowering its melting point and removing it as a barrier to coalescence. Such a process has been predicted to occur on the nanosecond time scale in molecular dynamic simulations[17] but would require very fast diffusion rates (effective diffusivity of ~10^{-9} m^2/s for Al and O to pass through 2-3nm oxide shell faster than the ~10ns time scale of sintering). Such high diffusivity may be achieved at higher temperatures, and if the process is assisted by the electric field developed from the charge imbalance between the oxide shell and core, i.e., a Cabrera-Mott mechanism.[46] In the case of laser heating, the physics is further complicated by the large oscillatory electric fields present in the hot spots, which can reach 10^8-10^9 V/m (see Section 4.S.3-Supplemental Information).

Another possibility is that the rapid coalescence observed under high heating rates may result from the formation of microfractures[37] in the shell, through which the molten Al core can flow and promote coalescence with the surrounding material. As these results show that the shell is not left behind as an empty container, such fracturing would not just let the core escape but would also have to promote the motion of the shell. This could occur through faster reduction of the shell once in contact with Al from both sides to create a lower melting, reduced oxide or if fractured into small enough pieces the shell could be pulled along with the flow of the

molten core. The later possibility may account for the irregular and rough shapes found in Figure 4.3d and the later images of Figure 4.1. A fracturing mechanism would operate under conditions of rapid heating in which both the hoop stresses in oxide are large and the oxide layer is softened due to the elevated temperatures. On length scales of only a few nanometers of aluminum oxide shell, failure of the oxide should be much faster compared to all other time scales. The threshold temperature would thus represent the point of sufficient stress and softening to allow this process to occur. Such a mechanism could explain why, in comparing the results of Figure 4.1(a,b) (laser heating, 10^{11} K/s) and Figs. 3(c,d) (resistive stage heating, 10^{6} K/s), the morphological changes are qualitatively similar despite the five orders of magnitude difference in heating rates and 2-3 orders of magnitude difference in cooling times (ms vs. multiple μs). If the coalescence were governed by a gradual process, one would expect more morphological changes in a material held at temperature for much longer. As this is not the case, a rapid mechanism, such as the one described, occurring at a defined threshold temperature seems more likely.

In combustion applications, fast coalescence has the potential to inhibit or enhance reactivity depending on the nature of the reaction. If the aluminum is isolated from other materials such that the oxidizer delivery rate is slow relative to the coalescence, then the loss of nanostructure will precede the bulk of the reaction. This is particularly relevant for aluminum particles oxidizing in a gaseous environment. Bazyn *et al*.[44] have measured burn times of aluminum on the order of tens of microseconds, even in a pressurized oxygen environment. My results suggest that the particles may coalesce well before they significantly combust. This could explain the

diminishing returns to burn times from reducing the size of Al particles,[56,58] as they can coalesce into larger particles prior to combustion, and thus do not retain the high surface-to-volume ratios needed for increased combustion rates. However, if the fuel is not isolated and is instead intimately mixed with nanoparticle oxidizer, fast sintering can facilitate the reaction by rapidly exposing a high surface area of molten fuel to the surrounding nanoparticle oxidizer matrix. Rather than coalescing towards a sphere, the mobile fuel could wet the contacted oxidizer, thereby increasing the amount of interfacial area and thus the reactivity, on time scales of ~10 ns. In the case of nanocomposite thermites (i.e., Al + CuO) in which nanoparticles of a metal oxide are mixed with the aluminum fuel, such a mechanism would support previous reports that the reaction proceeds, in part, via a reactive sintering mechanism.[16]

4.4. Conclusions

In situ high heating rate experiments on aluminum nanoparticle aggregates revealed that the nanostructure of the samples severely coarsened upon heating in a manner consistent with simple coalescence driven by the reduction of surface energy. When subjected to heating rates of 10^{11} K/s, aggregates were substantially coarsening within ~15 ns from the start of heating, and all significant changes were complete within 75 ns. Using a heating stage, it was determined that the threshold temperature for coalescence was around 1300 K, with qualitatively similar morphological changes despite a five order of magnitude difference in heating rate, indicating similar mechanisms taking place on the nanosecond and sub-millisecond scales.

These results allowed us to qualitatively assess the relevance of different mechanisms proposed for rapid combustion of Al-NP aggregates. Specifically, a mechanism resulting from the pressure induced spallation of the molten core of aluminum nanoparticle seems very unlikely, given that no such behavior was observed even at heating rates much faster than those typical for rapid combustion. Rather, the early-stage evolution appears to be a simple surface-energy-driven coarsening process, facilitated perhaps by fracturing or softening (via thermal and/or interdiffusion mechanisms) of the oxide shells. This process is sufficiently fast (~75 ns to completion given sufficient heating rates) to alter the combustion kinetics and reduce reaction rates by decreasing the surface area to volume ratio of the nanoparticle aggregates. This may help to explain the deviations from expected scaling of combustion rate with particle size and lower than expected reaction rates at particle diameters below ~100 nm. The observed phenomena and insight gained by these studies may extend to other applications. For example, given the short pulses that are sometimes used for optical excitation of nanoparticles, such as in hyperthermia and spectroscopy, the peak temperatures may be considerably higher than expected due to absorption hot spots in dense aggregates and the inability to conduct sufficient heat into the surroundings during the short time scale. This could lead to unexpected sintering and thus the loss of nanoscale structure. In short, competition between fast coalescence, which reduces the advantageous properties of nanoparticle systems, and reactions must be considered in the design and implementation of nanomaterials.

Acknowledgments

Experimental work was performed at Lawrence Livermore National Laboratory under the auspices of the United States Department of Energy by Lawrence Livermore National Laboratory under Contract W-7405-Eng-48 and was supported in part by the US DOE Office of Basic Energy Sciences, Division of Materials Sciences and Engineering under FWP-SCW0974. Work by BWR was supported by the US DOE Office of Basic Energy Sciences, Division of Materials Sciences and Engineering under FWP-SCW0974. Work by TL was supported by DTRA grant. Support for GCE and MRZ was from the Army Research Office.

4.5. Supplemental Information

4.S.1. Loss of Surface Area Estimation

The estimation for loss of surface area was based on a simplistic interpretation of the TEM micrograph results. Initial surface area of an aggregate was calculated assuming 80nm diameter particles and simply counting the number of particles (n_1) in the image. The surface area after heating is estimated by again counting the number (n_2) of distinct particles in the image, splitting the initial volume into that many spheres, and calculating the surface area of such spheres. The fractional loss of surface area is then the difference between surface area before and after heating, divided by the initial surface area, or $1 - (n_2/n_1)^{1/3}$. Obviously this method suffers from significant sources of error, from subjectivity in counting the number of particles to the fact that, after heating, the aggregates are clearly not equally sized

spheres (Figure 1b-f). However, these values are only intended as rough estimates and as aids in the comparison between sintering events. Since the relative size distributions are similar for different events, some of the systematic error will likely cancel out in effect when two such values are compared.

4.S.2. T-Matrix Modeling Approach and Upperbound Estimation

The upper bound estimate for temperature was calculated by using Mackowski's Multiple Scattering T-matrix Code[127,128] on an arbitrary 100 particle aggregate with fractal dimension of 2.5 and 80 nm Al particles to determine absorption efficiencies. The results of this are shown along with the Mie theory calculation for a single isolated 80 nm Al-NP in Figure S4.1. These results indicate that an aggregate will absorb far more energy than an isolated sphere, with most of the energy being absorbed towards the center of the aggregate. The minimal amount of contact between particles in an aggregate causes a contact resistance, which may prevent equilibration of the temperature over the short span of the 12 ns laser pulse and thus can lead to hotspots in the aggregate.

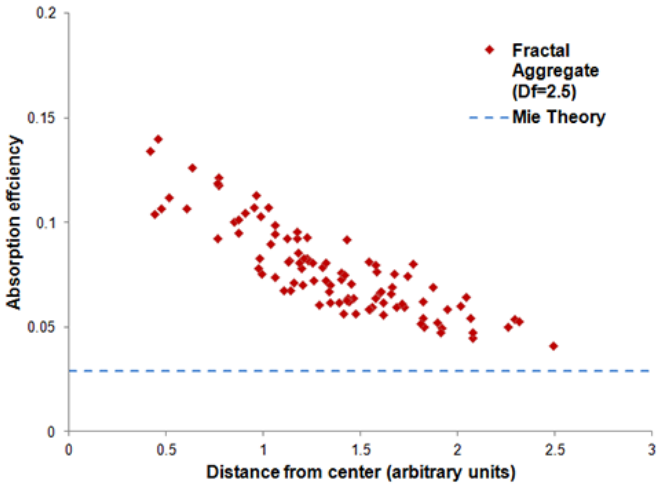

Figure S4.1. The Absorption efficiency of particles in an aggregate versus distance from the center as calculated with the T-matrix method. Df is the fractal dimension of the aggregate.

For the purpose of my estimation, I took the average absorption coefficient of the cluster of five particles including the most absorbing particle and those adjacent to it. These particles had an average absorption coefficient of 0.124. The experimental laser parameters were then applied assuming 74 nm Al core with 3 nm oxide shell and a 12 ns laser pulse and the absorption efficiency was allowed to increase with temperature during heating in line with the results of References 130 and 131. These calculations give a maximum for the temperatures that can be reached in the aggregate, but it is likely that this temperature is never reached because of conductive heat transfer between particles outside of the small cluster of five and to the substrate, which was ignored for this estimation. The actual temperature may also be lower because the enhancement to absorption is shape dependent and thus not all aggregates will have hot spots with such significant enhancement. It was also assumed that the cores were touching which has a large impact as will be seen in the next section

4.S.3. Finite Element Modeling Approach*

While the T-matrix method works well for calculating the laser absorption in a large and complicated arrangement of spheres, it is also important to understand the role of several elements not accounted for in these simulations. These elements include the roles of the oxide layer on each nanoparticle, heat diffusion during the laser pulse, and the substrate. To address these, a series of simulations were performed in the finite-element package COMSOL™, using methods that have been reported on previously[119] to calculate the laser absorption and thermal transport in nanostructured materials. As before, the laser absorption was calculated by solving Maxwell's equations in a scattered-wave formalism, using perfectly matched layers and scattering boundary conditions to implement the boundary condition that no waves were inbound from outside the simulation volume apart from a specified plane wave representing the laser pulse. The laser conditions were matched to typical values from the experiment: 1.06 μm wavelength, 42.5° incident angle from normal, 6 μJ per pulse, p polarization, Gaussian profiles in space and time, 12 ns FWHM pulse duration, and 135 μm $1/e^2$ spatial diameter. Since the laser beam was much larger than the region of interest, the laser profile was approximated by a uniform plane wave with an intensity equal to the intensity at the center of the Gaussian pulse used in the experiment. While the previous calculations[91] were two-dimensional, the current simulations are three-dimensional, but otherwise the methods are essentially identical. All material properties were taken to be linear and temperature-independent, consistent with the purpose of the calculations which was to estimate

* Please note that the work in this section was primarily done and written up by Dr. Bryan W. Reed, formally of LLNL Physical and Life Sciences Directorate

peak temperature rises typical of the widely varying experimental conditions (which, as is shown below, varied so much among the various scenarios that more precise handling of material parameters was unwarranted). The calculations were performed with aluminum radii of 20, 40, 60, 80, and 100 nm. The typical radius of the spheres used in the experiments was 40 nm.

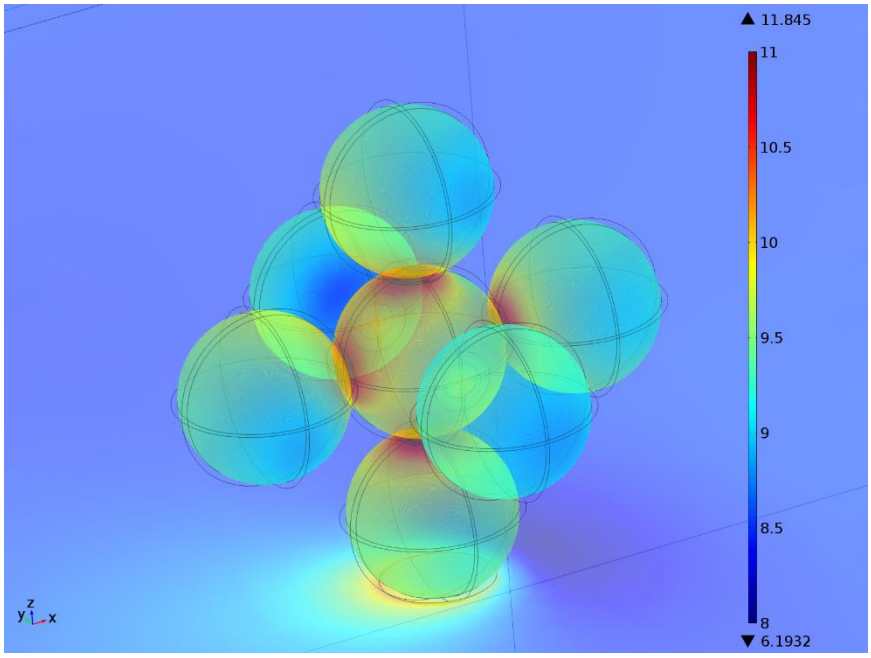

Figure S4.2. Finite-element laser absorption in joules per cubic meter, represented on a base-10 logarithmic color scale, for a cluster of seven 40-nm-radius spheres with the bottom sphere embedded in the formvar substrate. Result is shown for a 1 nm gap between spheres. The four-fold azimuthal symmetry is broken by the 42.5º incident angle of the laser.

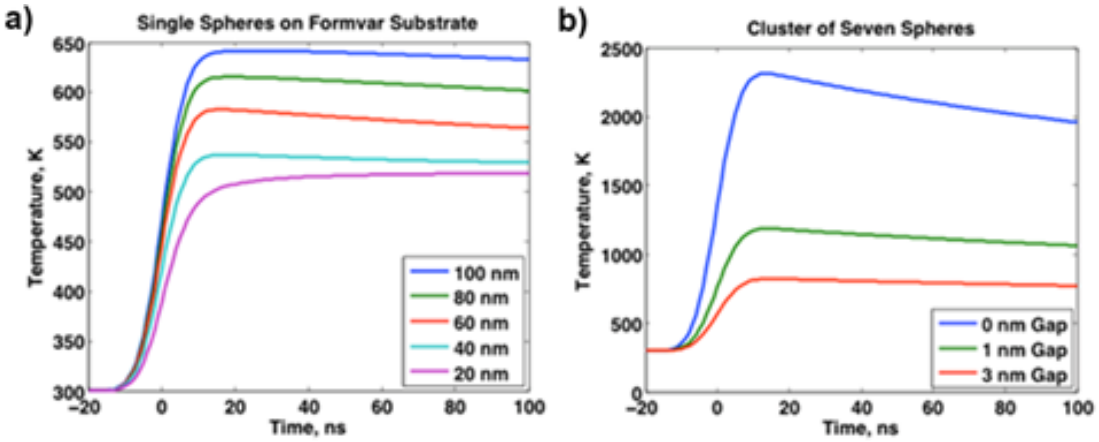

Figure S4.3. Finite-element laser heating calculations for formvar substrates with varying geometries. (a) As a function of aluminum sphere radius, not counting the 3 nm Al_2O_3 layer. (b) For a cluster of seven 40 nm spheres with varying intersphere gaps. While these are the mean temperature across all of the volume of aluminum, the plots of maximum and minimum aluminum temperatures would be essentially indistinguishable on this scale. The peak temperature for the 40 nm radius sphere approaches the 550 K value calculated from Mie theory, indicating relatively little heat loss to the substrate on the time scale of the laser pulse for this case. Note that formvar absorbs a significant amount of 1.06 μm light, so that most of the substrate itself peaks at a temperature of ~500 K.

In addition to the specified radii of the Al spheres, a 3-nm-thick Al_2O_3 layer was added. The substrate was modeled as a 1.5 μm x 1.5 μm x 30 nm uniform plane of either formvar or Si_3N_4 (both of which were used in the experiments; all calculations shown in the figures were performed with formvar substrates except where explicitly noted). The edge of the substrate was fixed at a temperature of 300 K. This boundary condition had relatively little effect until rather late in the simulation, where it affected the shape and time scale of the cooling rate curve. Since the peak temperature achieved during the laser pulse is the primary interest, the effect is negligible. For all simulations shown here, one of the spheres was embedded into the substrate to a depth equal to one-sixth of the radius of the aluminum (not counting the Al_2O_3 shell, which therefore accounts for an additional 3 nm). When more than one sphere was used, the spacing between the aluminum spheres was controlled,

again not counting the oxide, filling the remaining intervening space with Al_2O_3. Gaps chosen were 3 nm (i.e. the 3 nm oxide shells fully overlapped), 1 nm, and 0 nm (i.e. with the metal spheres meeting at a point; this limiting case introduces a geometrical singularity that produces somewhat mesh-dependent results, but the results are included nevertheless for the sake of completeness). Results from a cluster of seven spheres of radius 40 nm, arranged to have six absorption hot spots on the center sphere, as an idealized cluster of moderately high density, are shown in Figure S4.2. The results of varying the particle size and gap between metal spheres is shown in Figure S4.3. Tests were also run with varying materials, e.g. replacing the Al_2O_3 with additional aluminum, and replacing the formvar with Si_3N_4. These results are shown in Figure S4.4.

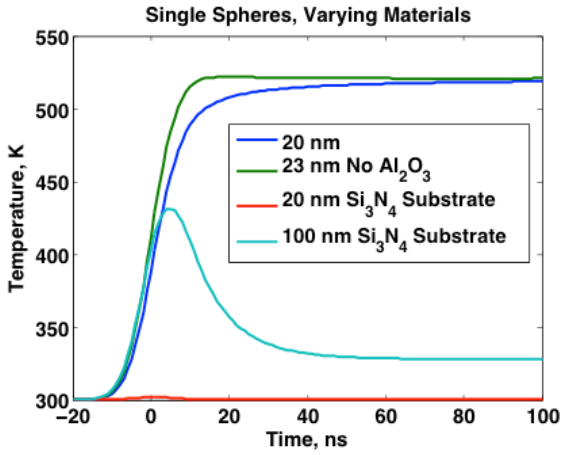

Figure S4.4. Same as Figure S4.3, but varying the materials. As above, substrates are formvar except where noted otherwise. The lack of absorption in the Si_3N_4 proves to be extremely important, especially for smaller spheres, in that it provides a high-capacity 300 K heat sink in close proximity to the aluminum. Note the 20 nm Al sphere has a 3 nm oxide shell and is thus the same total size as the 23 nm pure-Al sphere.

The finite-element results reveal a number of interesting things. First, for all of the sphere sizes considered (which were all much smaller than the laser

wavelength), the absorption per volume increased with the radius, and thus the absorption per sphere increased at a rate faster than the cube of the radius. Second, the influence of the oxide shell on the absorption of a single sphere is not very significant. While replacing the oxide with aluminum does accelerate the heat transfer between the sphere and the substrate, the effect on the peak temperature is fairly small. Third, the thermal conduction within each aluminum sphere is extremely fast, such that the temperature difference between the hottest and coldest points in the aluminum is only very rarely more than ~1-2 K. This is unsurprising, given the thermal diffusivity of aluminum and the duration of the laser pulse; the associated characteristic distance for heat conduction is roughly 1 μm. Fourth, the fact that the Si_3N_4 substrate does not absorb 1.06 μm light makes an enormous difference in the peak temperature reached by spheres in contact with it; in fact the 20 nm sphere on the Si_3N_4 substrate hardly heats at all, and even the 100 nm sphere only heats by ~130 K. Fifth, while a single sphere can attain a temperature rise ~300 K under the conditions of the experiment, it will never reach the much higher temperatures required for sintering. To do this requires hot spots such as those that occur when two spheres are extremely close together. Sixth, as shown in Figure S4.3a, the hot spot intensity is a very strong function of the exact size and shape of the hot spot. The dependence is so strong that the temperature rise associated with a hot spot cannot be confidently calculated and can only be roughly bound (e.g. within a factor of ~2 for a typical simulation) based on *a priori* knowledge of the material geometry. This is especially troublesome when considering that, at the peak of the laser pulse, a hot spot may reach a temperature well over 1000 K while it is subjected to an oscillating

electric field of $5x10^8$ V/m (the value obtained for the 1 nm gap) or even higher, and it can be expected that the material may undergo local melting, interdiffusion, dielectric breakdown, electromigration, and other complex effects that would further complicate any modeling efforts.

In short, the finite-element calculations show that, while the peak temperatures will vary over quite a large range in the laser absorption experiments, it is definitely possible to obtain the temperatures inferred from the experiment (~1300 K) in the case of a dense cluster of particles with a center of mass a significant distance (~100 nm or more) from the nearest heat sink.

Chapter 5: Time-Resolved Nanosecond Imaging of Nanoscale Condensed Phase Reaction*

Summary

The reaction between metallic fuel and oxygen carriers produced by the laser heating of aluminum and copper oxide (CuO) nanoparticles (NPs) was investigated using Movie Mode Dynamic Transmission Electron Microscopy (MM-DTEM), which enables multi-frame imaging with nanometer spatial and nanosecond temporal resolution. Nanothermite materials heated *in situ* at ~10^{11} K/s showed significant morphological changes on timescales of 0.5-5 μs. The resulting structures were typically phase-separated into adjoining spheroids. Further analysis with energy dispersive spectroscopy (EDS) and selected area electron diffraction (SAED) was used to determine the extent of reaction. Bulk scale reaction experiments using temperature jump wire heating (~10^5 K/s) revealed that both the reaction products and general processes were comparable to the reactions driven by the DTEM laser heating. These results indicate that condensed phase interfacial reactions are fast and are a dominant mechanism in nanothermite combustion.

5.1. Introduction

As discussed in Chapter 1, energetic mixtures made from metal fuel (e.g., Al, B, Si, Mg) and metal oxide oxidizer (e.g., CuO, Fe_2O_3, Bi_2O_3, MoO_3) nanoparticles

---

* The results presented in this chapter have been previously published and is reprinted with permission from: Egan, G. C.; LaGrange, T.; Zachariah, M. R., Time-Resolved Nanosecond Imaging of Nanoscale Condensed Phase Reaction. *Journal of Physical Chemistry C* **2015,** *119* (5), 2792-2797. Copyright 2015 American Chemical Society

I would like to thank my co-authors in that paper for all their hard work and input that made the paper and this chapter possible.

are known as nanocomposite thermites or metastable intermolecular composites (MICs) and have many commercial and research applications due to their high energy density, relatively low gas release, and fast reaction rates.[3,132] Recent research efforts have focused on developing high performance systems with higher burn rates as well as more controllable heat release, though optimization of nanocomposite thermite systems requires a better understanding of the combustion mechanisms and the times scales of the salient processes. Combustion dynamics are primarily influenced reaction pathway which can follow several different mechanism such as heterogeneous gas-condensed phase (burning particles in oxygen),[55,133] interfacial condensed phase (oxygen transfer across a boundary between two molten or solid materials),[16,24,134] or a more complex material response.[20,31,32] The gas phase reaction pathway occurs by the reduction of the metal oxide (e.g., $Fe_2O_3 \rightarrow Fe_3O_4$, $CuO \rightarrow Cu_2O$, $Co_3O_4 \rightarrow CoO$), which releases gaseous oxygen[55], thus allowing the Al-NP fuel to burn ($Al \rightarrow Al_2O_3$) in a high pressure oxidizing environment. Alternatively, condensed phase reactions occur by the diffusion of oxygen through solid and molten phases of these materials across their shared interfaces. In such reactions, the initial energy release drives sintering and coalescence, which creates larger interfaces and drive reaction faster (a process dubbed reactive sintering).[16] Lastly, a more complex response has been proposed, which involves the spallation of the aluminum from pressure build up within its native oxide shell.[20,31,32]

Some insight about the mechanisms involved in these processes has been gained through controlled "bulk" reaction experiments, though these results are difficult to interpret due to the multiphase, rapidly evolving, non-equilibrium

propagation of the reaction. The potential effects of different mechanisms often overlap, leading to varying interpretations of the results and contradicting theories.[20,23] Our lack of knowledge of the underlying mechanisms stems from the difficulty to experimentally observe the nanoscale changes occurring in these materials on the relevant timescales associated with the rapid heating rates and high temperatures intrinsic to the reaction and combustion dynamics. The dynamic transmission electron microscope (DTEM) at Lawrence Livermore National Laboratory (LLNL) enables the direct observation of morphological changes in nanocomposite thermites under very rapid heating conditions which can exceed 10^{11} K/s.[90,91,117,118] This allows one to isolate and probe the fundamental mechanisms and unit processes of combustion. Laser heating effectively enables instantaneous heating relative to typical reaction rates and heat losses. Further, these experiments occur in vacuum, which prevents any significant heterogeneous gas-condensed phase reaction. Thus such an experiment can capture the interfacial condensed phase interaction of these nanoparticle systems, without the convoluting effects of gas phase chemistry and heat transfer to and from the environment.

This approach provides information about the underlying properties of the condensed phase mechanism, which in turn allows for determination of what role it plays in the bulk combustion of nanocomposite thermites. Proper characterization of the extent and timescale of chemical reaction will determine if this mechanism is responsible for generating enough energy to drive fast self-sustaining combustion. The observed physical response will also indicate if any complex behavior such as the spallation of the molten metal fuel occurs.[20,31] Further, if the physics observed

through DTEM are occurring during bulk reaction, the products of both classes of experiments must be consistent.

5.2. Experimental Details

Al/CuO was chosen as a test system because of its wide use and the large number of studies pertaining to these materials. The aluminum nanoparticles purchased from Novacentrix were spherical and had a nominal particle size of 80 nm. The CuO was obtained from Sigma Aldrich and had a primary particle size of <50 nm. Samples were prepared by adding Al with roughly three times the amount of CuO to ethanol, ultrasonicating for ~5min, and then dispersing the suspension onto TEM grids.

The primary diagnostic tool was the DTEM which had been recently modified to allow multi-frame acquisition (Movie Mode DTEM or MM-DTEM) over large temporal ranges from a few nanoseconds to hundreds of microseconds. The details of this instrument were described in Section 2.4.2 and can also be found in previous articles.[90,91,117,118] In short, MM-DTEM is equipped with a pulse shaping laser and a high-speed deflector system. The pulse shaping laser produces a series of ultraviolet laser pulses with user-defined pulse durations and delays that produces a defined electron pulse train via linear UV photoemission. Each pulse captures an image of the sample at a specific time. The high-speed electrostatic deflector located below the sample directs each pulse (image) to a separate patch on a large, high-resolution CCD camera. At the end of the experiment, the entire CCD image is read out and segmented into a time-ordered series of images, i.e., a movie. The current

technology produces 9-frame movies and for these studies, 20 and 50 ns electron pulse durations and delays between the starts of subsequent pulses of 95 and 550 ns were used.

The TEM specimens were flash heated by a second laser ($1/e^2$ diameter of 135 μm) operating at a wavelength of 532 nm and a pulse duration of 12 ns to initiate the reaction between the Al nanoparticle fuel and CuO oxidizer nanoparticles. Stochastic electron-electron scattering events within the high intensity electron imaging pulses cause a reduction in spatial resolution of Movie Mode. The DTEM can also function in a traditional thermionic emission mode (i.e., continuous wave (CW) mode) to obtain higher spatial resolution images of pre-reaction and postmortem microstructure to observe in more detail the initial structure and final morphological changes after the specimen has cooled to ambient temperatures. Further analysis on the samples heated in the DTEM was performed using another TEM (JEOL JEM 2100F) with scanning and energy dispersive x-ray spectroscopy (EDS) capabilities, and the crystalline structure was analyzed with selected area electron diffraction (SAED). Additionally, bulk combustion experiments were performed using a temperature jump (T-Jump) wire heating setup at heating rates of ~$5x10^5$ K/s as described in Section 2.2. . The experiments were done in air and in the time of flight mass spectrometer (TOFMS) with ~100 μs resolution.[52,55,135]

5.3. Results and Discussion

Figure 5.1 shows an example of a small (~500nm) aggregate of Al and CuO that, under rapid heating, reacted and evolved within a period of 600 ns. Figure 5.1a

shows a thermionic CW mode image of the aggregate prior to heating. The aluminum particles, being a low atomic number material, are weakly contrasted in the image, spherically shaped (left and bottom sides of the aggregate), and easy to distinguish from the darker more irregularly shaped CuO particles (central region of the aggregate). Figure 5.1b shows a CW image of the resulting morphology after heating the aggregate with a 0.3 kJ/m^2 laser pulse. The original nanostructured morphology has been lost, having transitioned from <50 particles into 3 larger, phase-separated regions. Being denser, the copper-rich center region appears darker, while the two surrounding lighter areas are aluminum rich with a morphology that partially resembles the initial configuration of the aggregate. Figure 5.1c shows a series of time resolved images taken with the Movie Mode pulsed electrons. Morphological changes are observed to initiate within 45 ns of the laser heating pulse. Within 235 ns, the central CuO region was fully molten and spherical in shape, while Al particles can be discerned as distinct shapes, even with the low signal to noise ratio. By 425 ns, the Al-NPs coalesced towards the CuO region, losing their initial nanostructured character and reducing their specific surface area. At 615 ns, the morphology of the reacted aggregate is similar to that of Figure 5.1b, and no further significant changes in overall structure were observed. While further chemistry or morphological changes that are beyond the limited spatial resolution may have occurred past this time, such behavior is assumed to be negligible in regards to the overall reaction process. This assumption stems from the fact that anything other than minimal reaction or evolution of the structure would be associated with high temperatures,

which would drive further coalescence that could be observed with the resolution of the pulsed electron images.

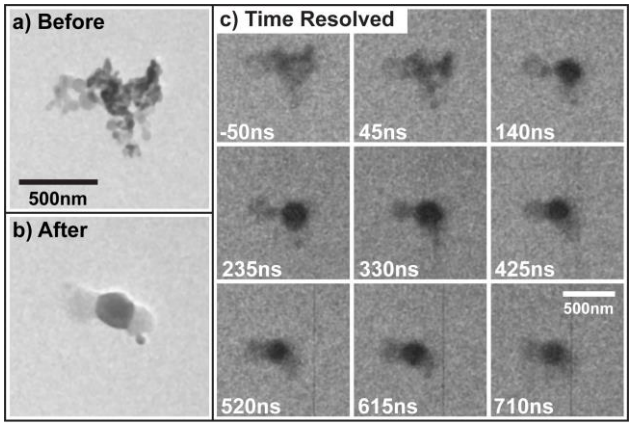

Figure 5.1. Morphological changes of Al and CuO NPs heated with a 532 nm laser (Pulse length=12 ns; Peak laser fluence = 0.3 kJ/m^2). (a) and (b) were taken in conventional TEM thermionic CW mode and the images of (c) were taken with pulsed electrons. (a) shows the aggregate prior to heating while (b) shows the resulting reacted material morphology. (c) Movie Mode DTEM image sequence showing the change in morphology with time. Each frame was taken with a ~20 ns electron pulse duration and 95 ns time delay between pulses. The listed times are relative to the peak intensity of the ~12 ns sample heating laser pulse. The same scale is used for both (a) and (b) with another scale shared by all the images of (c).

Through repeated experimentation with many different aggregates, the general characteristics of the microstructural evolution shown in Figure 5.1 were consistently observed. That includes the product morphologies always being phase separated into distinct regions and the most significant observable morphological change starting in the CuO regions with first melting and then coalescence. Under conventional, slow-rate heating, Al particles, having a melting point of 933 K, melts before CuO, which has a much higher melting point of ~1600 K. However, the laser pulse heated nanoparticles behave differently. Al nanoparticles have a 3 nm thick native oxide (mp= 2345 K) shell, which delays the onset of particle coalescence to above 1300 K.[54] Secondly, as verified by calculations using the Mie solution to Maxwell's

equations for 75 nm diameter particles, a CuO particle absorbs ~3 times more energy of 532 nm light than an Al particle.[136,137] Thus, being hotter, CuO particles are expected to melt first under laser heating. Figure 5.2 shows another example of a slightly larger aggregate going through the same general process seen in Figure 5.1 and described above.

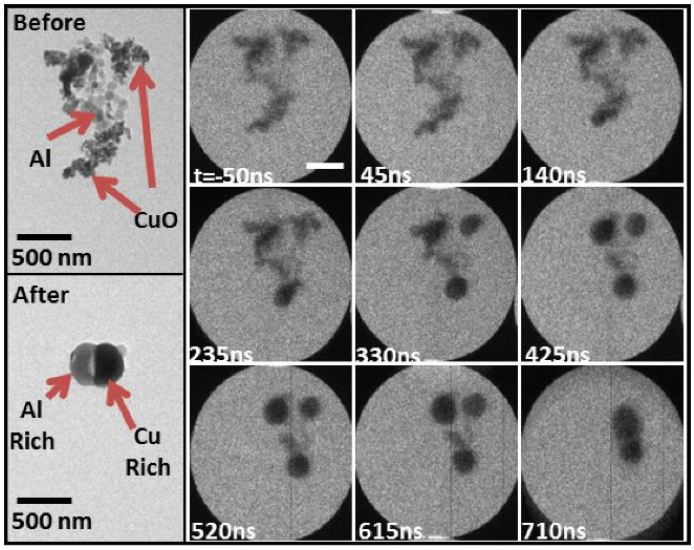

Figure 5.2. Another example MM-DTEM experiment on Al-CuO, heated with the same laser parameters as Figure 5.1. The before and after images were taken with CW mode. The 9 movie frames were taken with 15 ns electron pulses and the time listed is with respect to the peak of the heating pulse. The scale is the same for all frames in the movie, with the bar in the first frame representing 500 nm.

While the general morphological progression was consistent between experiments, time scales of the observed behavior were significantly affected by aggregate size and morphology. For example, in Figure 5.1 few significant changes were observed after ~600 ns in these small aggregates, but the morphological change was not yet complete by 710 ns in Figure 5.2. Even larger aggregates were observed to evolve over much longer periods of ~6 μs. Part of this slower response was that the observed onset of melting in large CuO particle regions was delayed significantly in

some large aggregates, For example, in the case shown in Figure 5.3, no discernible morphological changes were observed until 4.3 μs after the laser heating pulse. In comparison, small CuO aggregates (<500nm) melted fast (within ~100 ns). Relative to these timescales, melting should be instantaneous (on the order of the 12 ns laser heating pulse), which suggests that the CuO was not yet hot enough to melt. Therefore, the observed melting at longer delays occurred by heat released from reaction raising the temperature to the melting point and/or due to achieving a reduced melting temperature from alloying and/or oxide reduction.

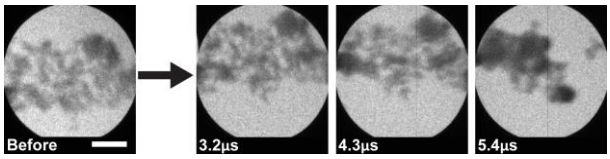

Figure 5.3. Morphological change of an Al-CuO aggregate that was significantly delayed (Heating laser pulse length=12 ns; Peak laser fluence =0.3 kJ/m^2). No discernible changes were observed until 4.3μs. All images were taken with ~50 ns electron pulses with 550 ns delays between images. The scale is the same for all images with the scale bar representing 500 nm.

The initial energy deposition from the laser heating pulse occurs within 12 ns, thus any additional heating occurring within this delay results from the exothermic reaction of Al and CuO. If one assumes the case where exothermic reaction raises the material to the melting point, the delay is an approximate measure of the diffusion rate of oxygen across the interface between the two materials. Such behavior could be accompanied by local morphological changes too small to be resolved in the pulsed electron images. Additionally, if this delay was caused by exothermic reaction, when testing pure CuO by heating with the same laser pulses, it would either melt instantaneously (i.e., within the pulse duration of the heating laser) or not at all, since there is no possible exothermic reaction without the Al fuel. However, experiments

using only CuO-NPs contradict this expectation. Indeed, size dependent delays did occur in a manner that was qualitatively similar to the Al-CuO samples (an example of this can be found Figure S5.1 of Section 5.5-Supplemental Information). In this case, the material was at its peak temperature immediately following the irradiation by the sample drive laser pulse, and thus the delay in melting must be ascribed to oxide reduction, as CuO nanoparticles, upon sufficient heating in vacuum, will reduce to Cu_2O, and eventually to Cu, both of which have lower melting points than CuO.[138] To test that this chemical evolution occurred within the TEM vacuum conditions used in these experiments, selected area electron diffraction (SAED) patterns were taken for the laser heated CuO. From these observations, the presence of Cu_2O and Cu in the products was confirmed (for more detail see Figure S5.2 of Section 5.5-Supplemental Information), indicating that laser heating alone was sufficient to cause reduction, which likely triggered the melting.

Assuming that the observed delay is associated to the timescale for oxide reduction, the size dependence may derive from temperature rise from laser light absorption being less for the large aggregates. Given the dense packing of the CuO-NPs, the particles on the upper layers of the aggregate scattered and absorbed much of the impinging laser light, and thus the particles in the deeper layers of the aggregate absorbed less energy, which reduced the average, equilibrated aggregate temperature. As a point of comparison, from Mie scattering calculations, as CuO particle size increases above 175 nm, the absorption efficiency per volume decreases with diameter.[136,137] Thus the larger, dense aggregates will have a lower average

temperature, and therefore slower reduction kinetics, which can increase the length of the delay.

To probe this process a little further, I turn to the characteristic diffusion time, which is defined as $t = \frac{l^2}{D}$, where l is the characteristic length scale and D is the diffusion coefficient. The important length scale here is the primary particle size radius. For a 30 nm diameter particle, the observed delays of 500 ns and 5 μs correspond to effective diffusivities of ~4.5×10^{-6} and ~4.5×10^{-7} cm^2/s respectively. While these values are high compared to the reported oxygen diffusivities in copper oxide (~10^{-9} cm^2/s for O in Cu_2O at ~1500 K),[139] at high temperatures and under vacuum conditions, CuO is far outside of equilibrium stability.[138] Assuming an activation energy of ~1-2 eV (typical values found for copper oxide)[43,135] for diffusion, the difference in estimated diffusivities can be accounted by a ~200-350 K difference in temperature between the two cases, which is consistent with the difference in absorption noticed by treating these large dense aggregates as single particles with Mie theory as described above. These kinetics could be better understood by more accurately modeling the laser heating, but unfortunately light absorption by the NP aggregates is very complex, and nanometer differences in shapes can lead to ~1000 K differences in modeled temperature, thus providing large uncertainties (See Section 4.S.3 in the previous chapter for more information).

This explanation implies that exothermic reaction was not necessary to promote the morphological changes observed in these experiments. To evaluate this further, elemental analysis was performed using energy dispersive X-ray spectroscopy (EDS) line scans as in Figure 5.4. These results clearly confirm that the

light areas are Al rich and the darker areas are Cu rich. Further, they indicate that the aluminum was significantly oxidized. In addition there appears to have been some alloying between the Al and Cu, which confirms that there was significant interaction between the Al and CuO, including the exchange of oxygen for reaction. However, it should be noted that the total amount of oxygen is diminished in comparison to the amount of Cu present. This loss of oxygen is consistent with an initial reduction to Cu2O, which led to both coalescence and subsequent reaction.

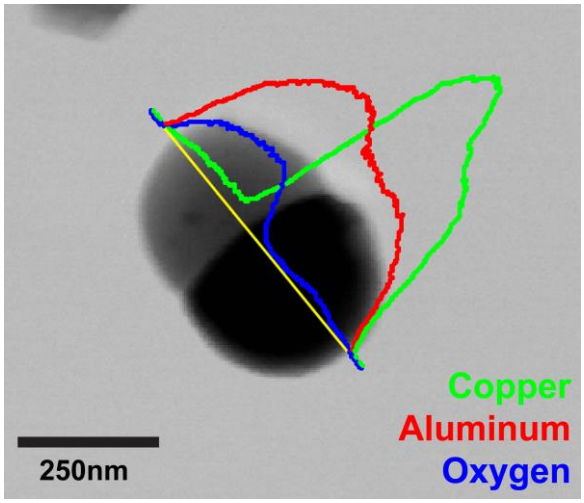

Figure 5.4. Post-reaction product from an Al/CuO laser heating experiment that was analyzed with an EDS line scan. The red line indicates the intensity of the Al signal, green represents Cu, and blue represents O. The results indicate a lighter Al/O phase and a darker Cu/Al phase.

Though laser heating was non-uniform due to compositionally driven variation in the optical absorption, the DTEM experiments compared well with reaction dynamics observed in nanocomposite thermally driven at lower rates. Figure 5.5 shows results from T-jump experiments where CuO-NPs and Al/CuO nanothermites were coated on a 76 micron diameter Pt wire and rapidly heated at a rate of 3.5×10^5 K/s, with oxygen evolution monitored by a mass spectrometer (see Section 2.2.2 for more detail).[52,55,135] These results show that the oxide alone can

release O_2 at slightly lower temperatures than the ignition temperature for the thermite. Further, a significant amount of gaseous oxygen was present in the system during the Al/CuO reaction. Thus any condensed phase interaction between the two materials must involve the CuO reduced phase.

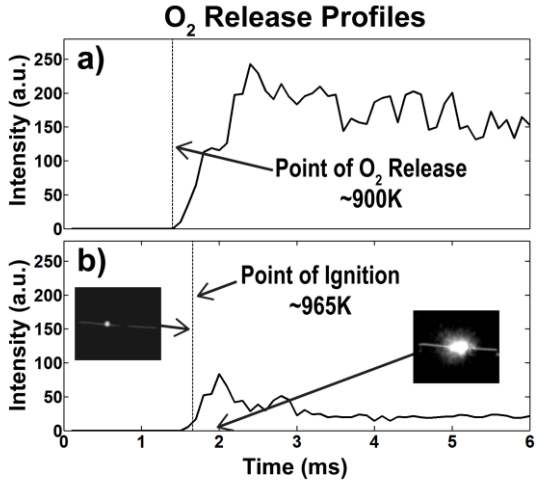

Figure 5.5. O_2 temporal evolution from T-Jump mass spectrometry in arbitrary units (a.u.) of intensity of (a) CuO and (b) Al/CuO. Samples were heated at ~$3.5x10^5$ K/s on a platinum wire and the temperature was calculated from the wire resistance. The temperatures listed are the average of several runs and the point of ignition was measured with a high speed video camera, frames of which are inset on (b). Note that CuO particles first released oxygen at temperatures below ignition followed by a rapid release of O_2 during combustion. Note that the fluctuation in signal intensity can be attributed to measurement noise.

The mass spectrometry study showed that violent reaction was possible despite loss of oxygen from the oxygen carrier to the vacuum environment (the O_2 signal). This result is supported by energetic calculations for this system. It requires 265 kJ to heat 2 Al and 3 CuO moles of reactant (which forms 1 mole of Al_2O_3) from room temperature to 1300 K, the temperature at which Al nanoparticles sinter and molten Al escapes the oxide shell and well above the ignition point of Al-CuO.[54] The heat of reaction for that same amount of material is -1208 kJ, which means only ~22% of the reaction enthalpy is required to heat a neighboring reactant of equal

volume to the ignition temperature and promote the propagation of the reaction. Even if it is supposed that reduction of CuO to Cu_2O is a prerequisite to ignition, still only 38% of the total energy is necessary. Figure 5.6 provides a schematic diagram of the energy released during these reactions. Therefore, a reaction involving diminished amounts of oxygen may play a large role in the overall propagation of the reaction, with further oxidation occurring heterogeneously with oxygen released from the earlier reduction of CuO over a longer timescale (~1 ms).[16]

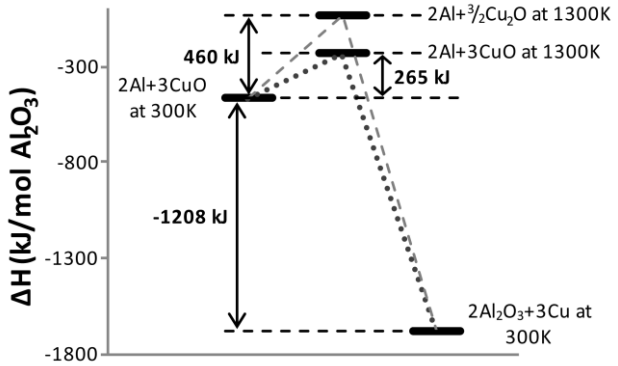

Figure 5.6. An energy diagram for the system. The elevated states represent the reactants heated to 1300 K. In the highest level 3CuO has also decomposed to 3/2 Cu_2O+3/4 O_2. In both cases the energy needed to reach that point is only 22-38% of the total energy released from reaction.

Another indication that the DTEM experiments are representative of bulk reaction processes is the similarity in morphologies observed under these very different conditions. Figure 5.7 shows quenched (~300 μs) reaction products from Al/CuO nanothermite mixture ignited on the Pt wire in air.[24] These products, which represents the majority of product volume, exhibits the same characteristic phase-separation found in the product phases of the DTEM experiments, with the two phases existing as adjoining spheres as in Figure 5.4. In this case, due to the large quantities of material, considerable coalescence results in much larger particles.

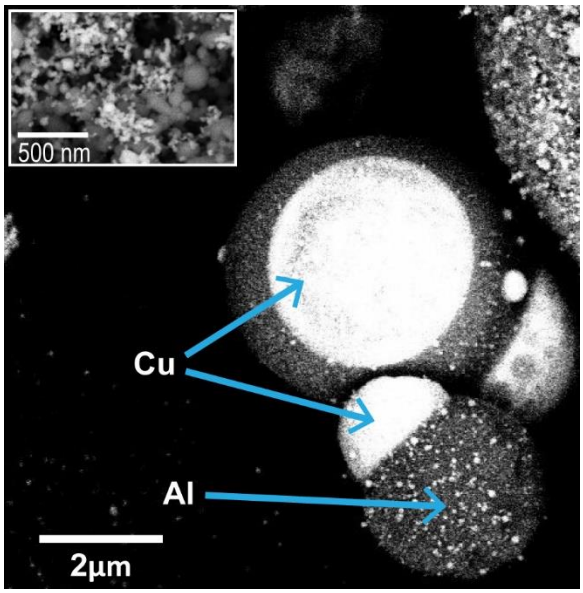

Figure 5.7. Products of Al/CuO T-jump wire ignited combustion that was quenched with a reaction time of ~300 µs. The image was taken with backscattered electrons (BSE) in an SEM, which show higher atomic mass material as brighter. Thus the bright phases are copper rich while the darker ones are Al rich. The inset image was also taken with BSE and contains the reactant prior to ignition, which shows the nanoscale nature of the reactant that was lost during reaction. More details of the experimental procedure can be found in Section 2.2 and a previous publication.[24]

From the above considerations, it is reasonable to apply the times scales observed in the DTEM experiment to bulk combustion processes. Al-NPs burn on time scales of 100 µs and longer in pressurized, oxidizing environments.[56,58] Thus the observed timescales of 0.5-5 µs for reaction indicate that condensed phase reactions are much faster than heterogeneous gas-condensed reaction, suggesting that they may play a dominant role in the rapid propagation of the reaction during combustion. Indeed, during constant volume combustion of Al/CuO nanothermite in pressure cells, pressures reach their peak in ~10 µs, which is consistent with the timescales reported here.[45] Further, none of the DTEM experiments contained any evidence of spallation of the metal fuel which would be indicative of the melt dispersion

mechanism.[20,31,32] Therefore a condensed phase "reactive sintering" process is likely.[16]

To apply these DTEM results in a broader manner, a characteristic diffusivity for reaction can be extracted. From the elemental analysis, the oxygen is seen to be homogeneously dispersed throughout the Al region. Therefore, to estimate diffusivity I treat the Al as an oxygen sink in a one dimensional system with an initial uniform concentration using the following expression:

$$t = \frac{(1.5l)^2}{D}$$

where t is the timescale of depletion, l is the length of the region, and D is the characteristic diffusivity.[43] With the characteristic timescales and diffusion lengths corresponding to the DTEM experiments, the average D is ~ $5*10^{-4}$ cm^2/s. This value is much higher than those typically discussed for thermite reactions, but compares well to the timescales required to diffuse O in molten Cu at temperatures of ~3000 K, as is expected for reaction of these materials.[140]

In the preceding discussion, I have only considered the length scales related to the size of the aggregate. However, the aggregate size is not well defined nor a defining quantity for bulk combustion where the materials exist as a millimeter sized powder compact. In this case, the extent of mixing in the powder components controls the kinetics of condensed phase reaction. Indeed, that is also the case for the DTEM results as the larger aggregates studied also had larger areas of segregation. This effect can be seen by comparing Figure 5.1 and Figure 5.3. Figure 5.3 is defined by a ~1000 nm long section of Al in its center, while the regions in Figure 5.1 are only about 300 nm. Bulk combustion studies have shown that mixing has a huge

effect on the performance of these nanothermites, which further supports the importance of the condensed phase interaction.[71]

5.4. Conclusion

In this study, I reported on the direct observation of the morphological changes that occur upon heating of Al/CuO nanothermites with *in situ* dynamic TEM. The creation of phase-separated adjoining spheroids was found to occur on the order of ~0.5-5 μs, a large temporal range observed to depend on the aggregate size. A partial reduction of CuO leading to a melt state occurred prior to significant reaction and morphological change. It was found that significant interaction between the two materials occurred, including reaction and alloying. While some of the original oxygen content was lost to the environment, the total energy of this system was such that even ~1/3 of the heat of reaction may have a significant impact on propagation. The products and overall process of the reaction were found to be comparable with the reaction of bulk phase material. Al NPs burned at faster rates in the DTEM experiments than in gaseous oxidizers, suggesting that the condensed phase reaction may be the dominant mechanism in bulk propagation rather than heterogeneous gas-condensed reaction or melt dispersion.

Acknowledgments

Work conducted by M.R.Z and G.C.E has been supported by the Army Research Office and the Defense Threat Reduction Agency. DTEM Research was

supported by the U.S. Department of Energy (DOE), Office of Science, Basic Energy Sciences (BES), under FWP# SCW0979, and the work conducted at LLNL was performed under the auspices of the U.S. Department of Energy by Lawrence Livermore National Laboratory under Contract DE-AC52-07NA27344. I also acknowledge the support of the Maryland NanoCenter and its AIMlab.

5.5. Supplemental Information

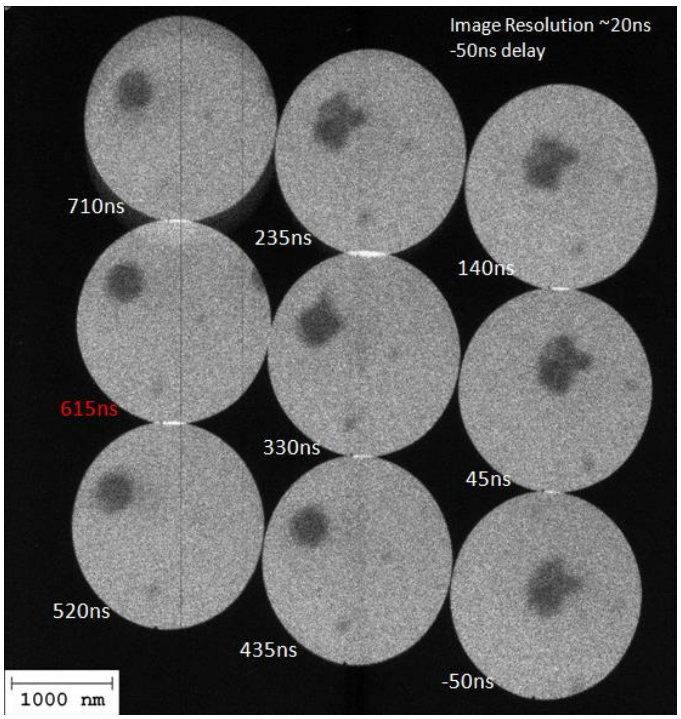

Figure S5.1. CuO-NPs heated with a 0.3 kJ/m^2 laser pulse. As observed in the first 4 frames (starting in the bottom left and moving up), there is no significant morphological change until the 330 ns frame, after which the material quickly coalesces to completion by 615 ns (highlighted in red). Note that this figure represents the raw image created by MM-DTEM.

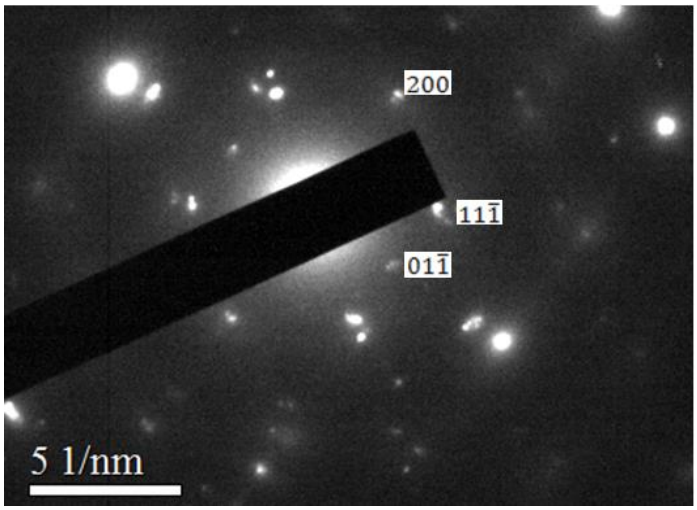

Figure S5.2. Selected area diffraction pattern from the product of CuO-NPs heated with a 0.3 kJ/m^2 laser pulse. As is clear the pattern is rather complicated because of size differences and multiple phases. However the primary pattern as indexed corresponds to Cu2O with a zone axis of 011. The multiple spots for some indices were likely a result of double diffraction.

Chapter 6: Direct Observation of Tantalum Nanoenergetic Material Subjected to High Heating Rates*

Summary

Recent studies have indicated that for some metal fuels, coalescence and sintering can occur faster than combustion, which can hinder reaction by decreasing available surface area. Tantalum is an interesting fuel in regards to this process because it only melts at high temperature (~3280 K), which means it could maintain its nanostructure for longer into reaction. In this study Ta based nanocomposite thermites (Ta-CuO and Ta-Bi_2O_3) were subjected to rapid laser heating (~10^{11} K/s) and the morphological response was observed with movie mode dynamic transmission electron microscopy (MM-DTEM). In these experiments, Ta was found to coalesce in under 400 ns, while reaction required significantly more time. Product from temperature jump (T-Jump) experiments was found to be significantly larger than for aluminum based nanocomposite thermites, which supports that coalescence is an important part of Ta nanocomposite combustion.

6.1. Introduction

Nanomaterials hold great potential for composite energetic material applications, which are those that combine fuel and oxidizer in separate phases to rapidly produce large amounts of energy. In particular, the increased specific surface area and decreased diffusion distances provided by nanoparticles have been demonstrated to produce reaction rates that are orders of magnitude faster than

* I would like to thank my collaborators for this study, Dr. Joseph Mckeown, Dr. John Roehling, Jeffery Delisio, and Rohit Jacob, for all their hard work and input that made this chapter possible.

micron scale equivalents.[3,6,13,125] However, several recent studies have shown diminished returns to this performance enhancement as particles are made smaller and smaller.[11,56,58] This comes in part from the proportional increase in the native oxide, which forms as 2-5 nm layer when the metal fuel is exposed to air. For particles 50-100 nm large, this oxide can represent a ~20-30% reduction in active fuel.[6,141] However, the diminished returns have been observed as well in oxide free cases, where it has instead been attributed to the coalescence of aggregates.[18] During both synthesis and handling, nanoparticles end up agglomerating into complex shapes that can be microns wide.[105,142] When heated, the large amount of surface energy intrinsic to nanoparticles will drive sintering and coalescence into larger particles.[17,69] Such behavior has been observed to occur very fast (<100 ns) relative to the typical timescales of combustion, which means that the nanostructure of the material will be lost before it can be accessed by the reaction.[54,79] Thus, the kinetics will be determined by the size after coalescence rather than the size of the initial primary particles, which explains the diminished improvement from further decreases to size.

In overcoming this process of nanostructure loss, one approach has been to structure the energetic with a gas generator in order to disperse the aggregates and prevent the majority of coalescence.[68,73,74] While these composites may have additional benefits, they also add complexity and additional steps to production. A simpler solution may be to find fuels with high melting points, so that the kinetics of coalescence and sintering will be slower and only occur after significant reaction. This way the small diffusion distances and high surface area will remain active through a significant portion of the reaction. For this purpose, tantalum (Ta) is of

great interest with a melting point (3280 K) that is higher than its adiabatic flame temperatures in most energetic composites (e.g., Ta-CuO at 1 atm constant pressure: 2840 K).[101] While, thermite composites with micron scale tantalum have been previously investigated, the properties of Ta nanoparticles (Ta-NPs) have not yet been well explored.[143,144] To determine the feasibility of this approach to minimizing the effect of nanostructure loss, more must be known about how the timescale of reaction compares to the timescale for sintering and coalescence.

In this chapter, I investigate Ta nanocomposite thermite reaction and nanostructure loss with *in situ* laser heating (~10^{11} K/s) experiments. The morphological response of the composite is observed using movie mode dynamic transmission electron microscopy (MM-DTEM), which allows for a sequence of 9 micrographs to be taken within ~750 ns. The high spatial and temporal resolution afforded by this technique enables direct measurement of the timescale for nanostructure loss. This process was found to start within in 10 ns and complete in <400 ns. Additional elemental analysis allowed for the determination that reaction was a slower process. The observed timescales and behaviors were related and compared to constant volume combustion cell and temperature jump (T-Jump) heating experiments.

6.2. Experimental Details

The tantalum nanoparticles were obtained from Global Advanced Metals and had a nominal particle size of 50 nm. The CuO and Bi_2O_3 were purchased from Sigma Aldrich and had primary particle sizes of <50 nm and 90-210 nm respectively.

For TEM samples, the fuel and oxidizer were mixed to be roughly equal in total volume, then suspended in ethanol and ultrasonicated for mixing. A micropipette was used to deposit the suspensions onto Ted Pella, Inc. TEM silicon nitride support films (50 nm thick, 0.25 x 0.25 mm window). For reactivity tests, the fuel and oxidizer were mixed stoichiometrically (assuming the Ta was 70% active by mass) in hexane using ultrasonication.

In situ experiments were performed using the dynamic transmission electron microscope (DTEM) at Lawrence Livermore National Laboratory (LLNL), which is capable of multi-frame acquisition (Movie Mode DTEM or MM-DTEM) over large temporal ranges from a few nanoseconds to hundreds of microseconds. The details of this instrument can be found in Section 2.4.2 and previous publications.[90-94] In short, the instrument functions by using UV laser pulses incident on the TEM cathode to drive photoemission in order to generate electron pulses with high enough intensity to produce an image. A high-speed electrostatic deflector located below the sample directs each pulse (image) to a separate patch on a large, high-resolution CCD camera. At the end of the experiment, the entire CCD image is read out and segmented into a time-ordered series of images, i.e., a movie. The current technology produces 9-frame movies and for these studies an electron pulse durations of 20 ns with 75 ns delays between the end of one pulse to the start of the next were used. The imaging electron pulses were timed with respect to a ~15 ns pulse from a second laser (wavelength = 532 nm; Gaussian beam profile with $1/e^2$ diameter of 135 μm) that was used to heat the sample.

The spatial resolution of images taken with the high intensity electron pulses is limited by stochastic electron-electron scattering events. The DTEM is also capable of operating in a traditional thermionic emission mode (i.e., continuous wave (CW) mode) to obtain higher spatial resolution images. This mode was employed for investigating the initial structure before heating and the final morphology after the specimen had cooled to ambient temperatures.

Further analysis on the samples heated in the DTEM was performed using another TEM (JEOL JEM 2100F) with scanning and energy dispersive x-ray spectroscopy (EDS) capabilities.

Bulk combustion product collection experiments were performed using a temperature jump (T-Jump) wire heating setup at heating rates of ~$5x10^5$ K/s as described in Section 2.2.[24,38,55] Sample was coated onto platinum wires, which were heated with 3 ms pulses to cause ignition. A carbon tape substrate positioned ~3 mm from the wire collected the product thrown from the wire, which was then analyzed using scanning electron microscopy (SEM).[24]

Reactivity was measured using a constant volume (13 cc) combustion cell described in Section 2.3.[45] 25 mg of material was ignited with a NiCr wire inside the cell and the resulting pressure and optical signals were recorded.

6.3. Results

A representative result from a MM-DTEM experiment on Ta-CuO is shown in Figure 6.1. The image taken before heating (Figure 6.1a) shows that the fuel and oxidizer possessed features <50 nm in size and there is intimate contact between the

two components. While both materials produced similar contrast, the two can be readily distinguished by their differences in morphology. The Ta, which is primarily on the right side in this image, was less densely packed and featured well-defined primary particles. In comparison, the CuO on the left was tightly packed with less clear delineation between particles. Fig. 1b shows the time resolved images taken with pulsed electron. Time=0 corresponds to the peak of the heating laser pulse (total 38 μJ delivered) in regards to the middle of the 20 ns imaging pulse. As the 15 ns heating pulse was shorter than the imaging pulse, the entire heating process is captured in that first frame and it can be seen to have produced morphological change even within this short time. By 95 ns, the CuO rich left side and Ta rich right side have independently coalesced. Through 285 ns, the two sides joined together and became one single ~500 nm particle. Having lost nearly all of its nanostructure by 380 ns, there were no more major morphological changes that occurred through the remaining frames. However, the edge of the particle underwent minor changes that continued past 760 ns, as evidenced by the shape in the final frame of the video being different from the after image (Figure 6.1c). Additionally, in the later frames of the movie, a thin spot in the center of the particle can be seen to form, perhaps as the result of gas release. The results from an EDS line scan along the arrow in Fig. 1c are shown in Fig. 1d. Quantification of points at the peak of Ta signal and peak of the Cu signal along the line gave atomic compositions of 50% Ta, 27% Cu, 23% Oxygen and 2% Ta, 75% Cu, 23% O respectively. This result suggests that the material did not fully react before cooling, since the Ta is not fully oxidized (Ta_2O_5 corresponds to 29% Ta and 71% O) and the CuO was not fully reduced to Cu.

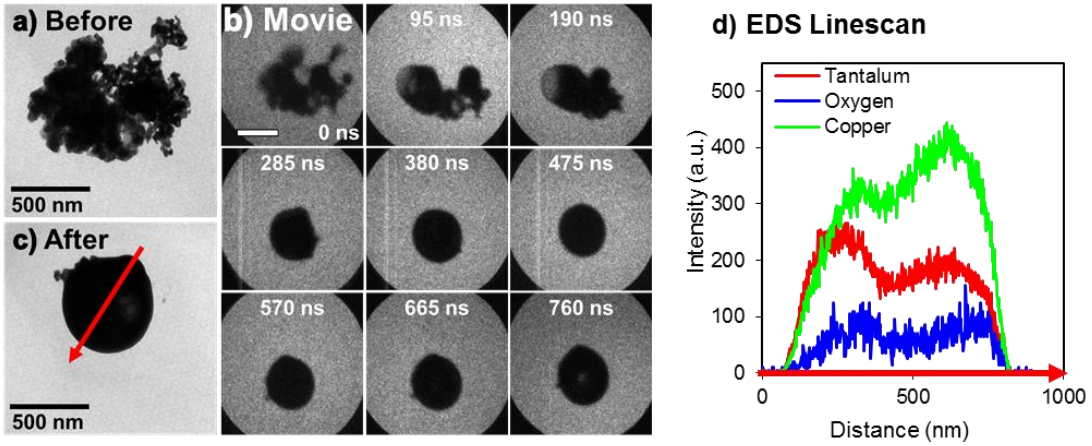

Figure 6.1. Example of the morphological response to a laser heating (38 µJ) pulse observed with MM-DTEM a) shows the aggregate prior to heating. b) shows the frames of the time resolved movie. The scale bar in the first frame corresponds to 500 nm and the scale is the same for all frames. The times given are for the middle of the (20 ns long) imaging pulse with respect to the peak of the 15 ns laser heating pulse. c) shows the final morphology after cooling. a) and c) were taken with the CW mode in comparison to the pulsed mode used for b). d) shows the results of an *ex situ* EDS linescan along the arrow shown in c). The weak oxygen signal was multiplied by a factor of 5 for readability.

The general behavior shown in Figure 6.1 was observed consistently for Ta-CuO. This included dramatic change within the first 95 ns, often with significant changes visible in the frame coincident with the heating, which indicates a timescale of ~10 ns (since the material won't be very hot during the first half of the imaging). The loss of nanostructure process was typically complete by ~400 ns, but many samples continued to undergo more minor shape and contrast changes past the time of observation (760 ns). This suggested that the material was still hot and mobile through that time. In a couple of cases, the mobility was such that two separate bodies of material would come in contact and coalesce, leaving a drastically different morphology from the time of the last frame to the taking of the after image. An example of this is shown in Figure 6.2. In the movie (Figure 6.2b), it can be seen

from 380 ns and 760 ns only minor observable change occurred, suggesting completion of the process. However, the after image in Figure 6.2c clearly shows a major change occurred afterwards, with the two separate bodies joining. More of the Ta coalesced as well, which suggests that the joining process significantly raised the temperature of the metal, either through reaction or by the other body simply being hotter. Another change that occurred was that the material slightly to the top right of the joined material in the images (copper as confirmed with EDS) wet the substrate, becoming wider and thinner. This behavior was observed in many samples and was often accompanied by the bubble looking features apparent in Figure 6.2c. This suggests that the copper material produced gas in its molten state, either through decomposition from CuO to produce O_2 or vaporization of the metal. Reaction with the silicon nitride substrate to produce Cu, N and SiO_2 is also possible. It was typically difficult to distinguish between different phases present in the final morphologies of Ta-CuO sample. The EDS map in Figure 6.2d reveals a clear delineation between a copper rich zone and a Ta rich zone, but the regions were generally not as well defined for other experiments. The fact that this example reached a further point in the reaction process, with the copper region being fully reduced, than other cases (as with Fig. 1) suggests that the reaction process requires more than 760 ns to complete. However, it should be noted that the tantalum is still far from fully oxidized.

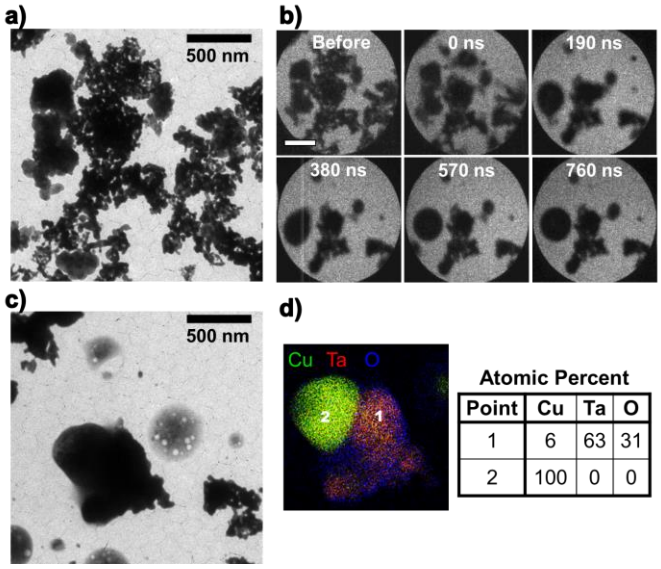

Figure 6.2. Another example of a MM-DTEM experiment performed on Ta-CuO, this one using a 40 µJ heating pulse. Part a) was taken prior to heating, as was the first frame in the movie shown in b). Note that the scale is the same for all frames in b) with the bar representing 500 nm. The after image shown in part c) indicates that major morphological change occurred outside of the recorded time frame. a) and c) were taken in CW mode, while b) was taken in pulsed mode. Part d) shows an EDS map of the sample along with the results of the quantification done at the two points shown on the map.

Experiments with Ta-Bi_2O_3 illustrated that it behaved in mostly the same way as Ta-CuO, except for a few key differences. The example shown in Figure 6.3 exemplifies these similarities and differences. For both materials, there was observable change occurring within frames coincident with the heating pulse (frame two of Figure 6.3b) indicating sintering and coalescence happening on the order of ~10 ns. The final morphologies for both systems were similar as well, with fuel and oxidizer products combined into as single large particle. Reaction also did not appear to occur to a significant degree, with oxygen more associated with the Bi rich areas than Ta region (see Figure 6.3d). Despite these similarities, there was a difference in overall time scale, as the final morphologies for Ta-Bi_2O_3 were generally stable after ~400 ns. Neither the subtle (e.g., bubbling, surface movement) nor drastic morphological changes that occurred over longer times in the CuO composites, were

observed for Bi_2O_3. The only observable change that occurred was the movement of material that had likely been launched by gas generation. This can be seen with the two particles to the top and right of the movie frames in Figure 6.3b. The particle coalesce within 95 ns, but then move out of frame at a speed of ~2 m/s. This behavior was commonly observed with the Bi_2O_3 cases, but not CuO.

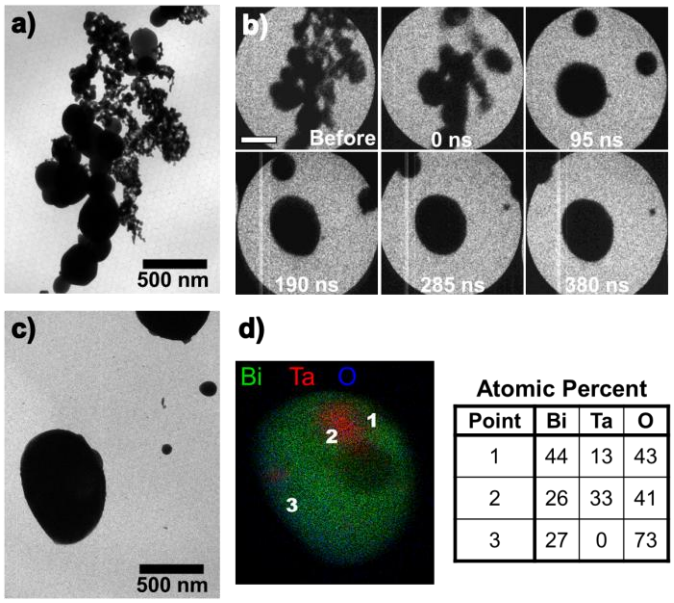

Atomic Percent

Point	Bi	Ta	O
1	44	13	43
2	26	33	41
3	27	0	73

Figure 6.3. An example of a MM-DTEM experiment performed on Ta-Bi_2O_3 using a 34 µJ heating pulse. Part a) was taken prior to heating, as was the first frame in the movie shown in b). Note that the scale is the same for all frames in b) with the bar representing 500 nm. The Bi_2O_3 can be easily distinguished from the Ta, by its much larger (>100 nm) primary particle size. c) was taken after cooling. a) and c) were taken in CW mode, while b) was taken in pulsed mode. Part d) shows an EDS map of the sample along with the results of the quantification done at the points shown on the map.

One other behavior that was unique to Bi_2O_3 systems was a violent "splattering" that occurred with higher laser energies. This occurred fast (<95 ns) and left particles of Bi_2O_3 and Bi as small as 10 nm dispersed around the original location of the material. An example of this is shown in Figure S6.1 in Section 6.6-Supplemental Information. This violent response was presumably caused by rapid gas generation from decomposition or vaporization within liquid Bi_2O_3. A milder version

of this process is likely also responsible for the launched material observed in Figure 6.3b.

To relate the nanoscale morphological changes observed with DTEM to those that occur during the bulk combustion process, product was collected from material ignited through a temperature jump (T-Jump) technique.[24] A carbon tape substrate was placed ~3 mm from a Pt wire coated in the thermite that was heated at ~$5x10^5$ K/s to 1300 K. Example results from Ta-CuO are shown in Figure 6.4. The lower magnification image (Figure 6.4a.) shows a wide distribution of particle sizes with many that have diameters greater than 10 μm. The particles are mostly spherical with many incorporating both Ta and Cu into a single particles. In Figure 6.4b, the particle has a clearly defined copper region (the smaller cap towards the bottom left as determined with EDS) while the bulk of the particle was oxidized Tantalum. The nanoparticles that are adorning the two particles towards the top of the image, likely formed from the vapor phase and deposited onto the surface.[24]

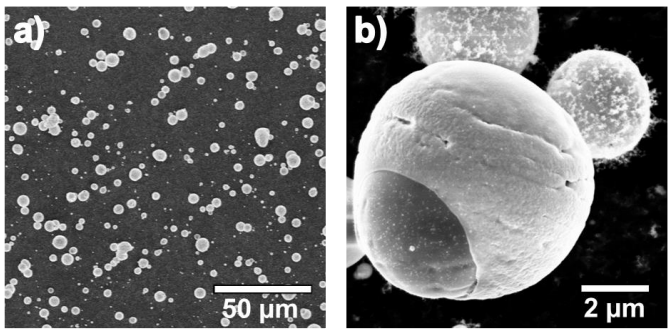

Figure 6.4. Low magnification (a) and higher magnification (b) scanning electron microscope (SEM) images of product collected 3 mm from a Ta-CuO T-Jump experiment.

As a point of comparison for the timescales observed with DTEM, constant volume combustion cell experiments were used to gauge the reactivity of the Ta based nanocomposite thermites. Example pressure and optical traces are shown for

both Ta-Bi_2O_3 and Ta-CuO in Figure 6.5. As can be seen, Bi_2O_3 was a better oxidizer than CuO in that it produced higher pressures and burned faster. The pressure rise time (time to peak pressure) and the burning time (full width half mas of optical signal) were 1.3 ms and 1.5 ms respectively for Ta-Bi_2O_3 and were 2.1 ms and 2.3 ms for Ta-CuO. This is about an order of magnitude slower than for the same oxidizers with Al-NPs, where the burning time is typically 100-200 µs (see Table 1.1).

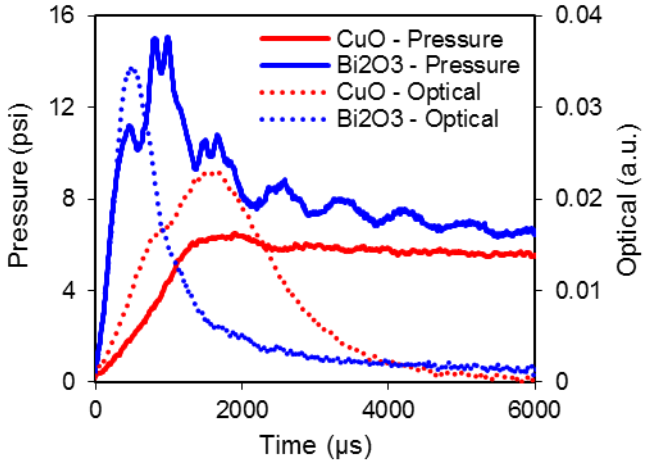

Figure 6.5. Example results from constant volume pressure cell on Ta-CuO and Ta-Bi_2O_3. Pressure signals are shown with solid lines and optical signals are shown with dotted lines.

6.4. Discussion

For both Ta thermites studied with MM-DTEM, loss of nanostructure started within 10 ns of heating and would be mostly complete within ~400 ns. In this time, condensed phase reaction was typically not complete as evidenced by the elemental analysis of the products revealing incomplete reduction of the oxidizers and lack of oxygen associated with Ta. In the case of Ta-CuO, bubbling and further movement continued past the timeframe of the movies, but no such behavior was clear for Ta-

Bi_2O_3. In either case, it is apparent that for these experiments, the high melting point of Ta does not preserve the nanostructure through to the reaction process.

From the combustion cell experiments, timescale of bulk reaction is on the order of a millisecond. Thus the observed nanostructure loss occurred 3-4 orders of magnitude faster, which suggests that it will be complete long before the majority of combustion occurs. But to better determine if the same behavior observed with MM-DTEM occurs during larger scale reaction, an understanding of the temperatures achieved through the laser heating is needed. Unfortunately, as a result of the complex shapes of these aggregates, the laser absorption process cannot be modeled accurately. As was shown in Section 4.S.3, even small changes to the geometry can lead to ~1000 K differences in absorption.[54] Thus knowledge of temperature must be restricted to rough estimates based on morphological behavior. As the Ta aggregates were observed to coalesce rapidly, even in the absence of oxidizer, it can be assumed that the used laser energies were sufficient for tantalum to reach its melting point (3280 K). However, calculations using CHEETAH 6.0 equilibrium code, show that the adiabatic flame temperature of the both thermite systems is much less than that temperature under constant pressure (1 atm) conditions, with a value of 2840 K for Ta-CuO and 2280 K for Ta-Bi_2O_3 assuming stoichiometric mixture and ignoring the oxide shell. This suggests that the morphological change driven by melting observed in the DTEM, may not be representative of typical combustion conditions. But, if some confinement is included in the calculation, such as 10% theoretical maximum density (TMD) constant volume condition, the adiabatic flame temperatures become 3260 K and 3590 K for Ta-CuO and Ta-Bi_2O_3 respectively, which makes melting of

Ta possible. A previous pyrometery study on nanocomposite thermite burn tube experiments showed temperatures significantly higher than the constant pressure value.[29] This makes sense given that there is an observable pressure rise that occurs in both burn tubes and combustion cells.[10,45] Therefore, the constant volume condition may be more applicable and it is reasonable that the material gets hot enough during the combustion process to behave as it was observed in MM-DTEM.

However, there is still a question of heating rates and when the material would reach this high temperature. In DTEM experiments, all the energy to drive morphological change and reaction is provided within the ~15 ns laser heating pulse. In free combustion, the heating rate is significantly slower. Even in the case of Al-CuO reaction, which is much faster than Ta-CuO, the fastest observed timescale is ~10 μs. If it is assumed that this represents the time it takes for a discrete set of material to reach the peak temperature, then this represents a 3 orders of magnitude slower heating rate than in DTEM. Since both the metal and oxide were found to significantly coarsen in 10-400 ns and this presumably occurs around their respective melting points, there will be a several μs period where the oxide has coalesced but Ta has not. During this time, the oxidizer could wet the Ta aggregate and access the high surface area for reaction. This would allow for a significant portion of reaction to occur prior to the loss of nanostructure, despite the short timescale of the process. For this reason it is not possible to determine how nanostructure of Ta is lost during combustion events from just these DTEM experiments.

Looking further into the process of combustion, Figure 6.4 clearly shows that the products of reaction are much larger than their starting size. This suggests that

condensed phase reaction and coalescence plays a large role in the reaction process. The particle size distribution was analyzed using micrographs at the same magnification as in Figure 6.4a and image processing in the same manner as in Reference 24. At these magnifications, small particles are not well represented, but previous analysis has shown that the large majority of product mass is held in the clearly visible large particles. Ignoring particles smaller than 500 nm, the average diameter of the product particles was 2.5 μm for Ta-CuO. This is larger than the average size of 1.6 μm found for Al-CuO using the same data set as in that previous study. This shift towards larger particles is more dramatic when considering that the amount of mass held in each particle will be proportional to volume. Having a larger mass means that particle contributed more energy to the overall reaction. The breakdown of the percent of total volume held in different size particles for both Al-CuO and Ta-CuO is shown in Figure 6.6. This shows that the Al system product had much more of its volume in small particles compared with Ta. In particular, no Al-CuO particles were larger than 10.5 μm, while 24% of the Ta-CuO system's volume, and thus mass, ended up in the particles larger than that. This analysis helps further illustrate the validity of ignoring smaller particles, as for Ta-CuO, particles between 0.5 μm and 1 μm make up 44% of the total number of particles, but they account for only 0.5% of the mass.

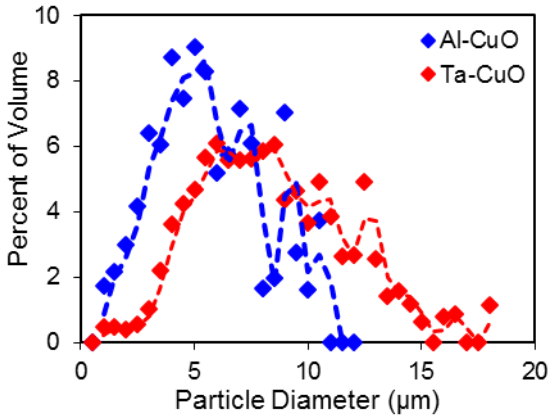

Figure 6.6. Volume analysis based on the particle sizes determined from product collection of Ta-CuO and Al-CuO. Particles were assumed to be spherical to calculate volume and were sorted into bins 0.5 μm wide. The dotted lines are trend lines formed from the moving average of data sets.

The size analysis data provides further evidence that the high melting point of Ta does not sufficiently inhibit coalescence and sintering. However, there is still no clear indication of when the loss of nanostructure happens for Ta. It is still possible that the oxide coalesces and wets the Ta aggregates, which then only lose their nanostructure after a significant portion of reaction. Since coalescence has been shown to be so fast, it is not clear that the product would look any different between the case of oxidizer coalesces→Ta coalesces→reaction and the case of oxidizer coalesces→reaction→Ta coalesces.

As for why the product is much larger than for Al nanocomposites, that may be related to the amount of gas produced. In the combustion cell, Ta-CuO produced a pressurization rate (peak pressure divided by pressure rise time) of 3.2 psi/ms, while previous Al-CuO studies produced 11000 psi/ms.[45] This difference in gas release is supported by equilibrium calculations as well, where at 1 atm constant pressure, Al-CuO produces 70 times as much gas as Ta –CuO (5.4 g/mol vs. 0.076 g/mol).[101] It follows that rapid gas release is needed to separate large agglomerates and prevent the

formation of very large particles. This type of behavior was previously observed with phase field imaging, with Al-Fe_2O_3, which doesn't produce much gas, forming much larger particles than Al-CuO.[16] Similarly, incorporating gas generators into nanoparticles has been shown to lead to smaller product and increased performance.[68,73,74]

6.5. Conclusion

MM-DTEM experiments on Ta nanocomposite thermites indicated that coalescence occurred significantly faster than reaction. For both Ta-CuO and Ta-Bi_2O_3, fuel and oxidizer lost significant portions of their nanostructure within ~10 ns of the laser heating pulse. The majority of this process was complete in less than 400 ns, however for Ta-CuO the material stayed hot and continued to shift and release gas. Post experimental EDS elemental analysis indicated that most samples did not undergo significant reaction. Despite the fast loss of surface area for Ta preceding reaction with laser heating, it cannot be conclusively determined if it occurs as such during combustion due to a several order of magnitude difference in heating rates. Product collected from T-Jump experiments indicated that a condensed phase reaction mechanism occurs and leads to a large degree of coalescence, likely in part because of a lack of gas production to separate aggregates.

Acknowledgments

Work conducted by M.R.Z and G.C.E has been supported by the Army Research Office and the Defense Threat Reduction Agency. DTEM Research was supported by the U.S. Department of Energy (DOE), Office of Science, Basic Energy Sciences (BES) and the work conducted at LLNL was performed under the auspices of the U.S. Department of Energy by Lawrence Livermore National Laboratory. I also acknowledge the support of the Maryland NanoCenter and its AIMlab.

6.6. Supplemental Information

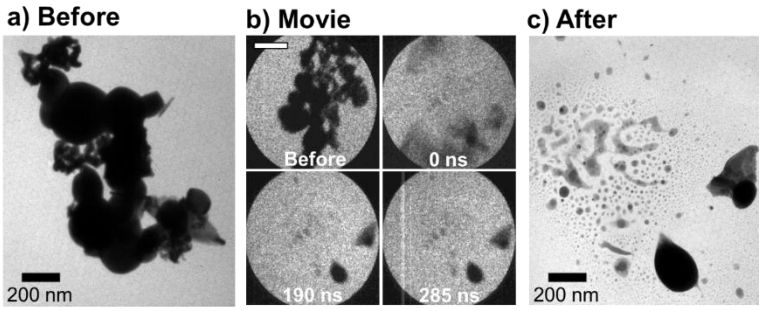

d) Elemental analysis

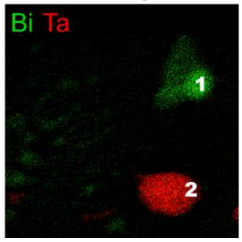

Atomic Percent

Point	Bi	Ta	O
1	17	0	83
2	0	42	58

Figure S6.1. An example of the "spluttering" behavior observed for some Ta-Bi_2O_3 cases. In this example a 38 µJ heating pulse was used. Part a) was taken prior to heating, as was the first frame in the movie shown in b). Note that the scale is the same for all frames in b) with the bar representing 500 nm. c) was taken after cooling. a) and c) were taken in CW mode, while b) was taken in pulsed mode. Part d) shows an EDS map of the sample along with the results of the quantification done at the points shown on the map.

Chapter 7: Reaction Dynamics of Al/CuO Nanolaminates at High Heating Rates*

Summary

Al/CuO reactive nanolaminate ignition was studied using temperature jump (T-Jump) heating for rates greater than 10^5 K/s. Multilayer samples were sputter deposited onto thin platinum filaments in alternating layers of Al and CuO. The filaments were resistively heated in a time of flight mass spectrometer (ToF-MS) while ignition and reaction were observed with high-speed video. A total deposited thickness of 1800 nm was maintained for all samples while the number of bilayers was varied from 1 to 12. Increasing this value decreased the diffusion distances and increased the amount of interfacial area across which reaction could occur, while keeping the overall energy of the system constant. From 2 to 6 bilayers the ignition temperature decreased from 1250 K to 670 K and the overall reactivity increased. Past 6 bilayers, the ignition temperature only decreased slightly and there was little impact on the overall reactivity. This behavior is consistent with a mass-transport model where the predominant diffusing species exhibits a low activation energy (50 kJ/mol). Ignition temperature, which depends upon bilayer thickness, is found to be a good predictor of flame speed.

---

* The results presented in this chapter have been previously published and are reprinted with permission from: Egan, G. C.; Mily, E. J.; Maria, J. P.; Zachariah, M. R., Probing the Reaction Dynamics of Thermite Nanolaminates. *Journal of Physical Chemistry C* **2015,** *119* (35), 20401-20408.

I would like to thank my co-authors in that paper for all their hard work and input that made the paper and this chapter possible.

7.1. Introduction

Incorporating nanomaterials into thermite systems significantly improves the strongly exothermic oxygen exchange reaction between the metal fuel and metal oxide oxidizer. Nanoscale materials offer decreased diffusion distances and high interfacial surface area compared to traditional micron scale powders.[3,125,132] As a result, nanostructured thermite compositions have lower ignition temperatures and react faster, with flames speeds up to 1 km/s.[12] Most formulations involve nanoscale powders, but an alternative approach that offers greater control of the resultant architecture is physical vapor deposition (PVD), in which alternating layers of fuel and oxidizer are stacked into planar structures, referred to commonly as reactive multilayers or nanolaminates.[15,61,86,145] Such structures are tunable and can be readily incorporated into MEMS processing, which makes them of interest for a variety of micropyrotechnic applications.[14,146] Regardless of the physical embodiment, much remains unknown about the processes and kinetics that control thermite ignition and reaction. Thus, the idealized form factor of nanolaminates provides a valuable avenue to explore this behavior. While reactive nanolaminates have been studied extensively at slower heating rates (~10 K/min) in differential scanning calorimetry or thermogravimetric experiments, complimentary work is needed for heating regimes that more accurately reflect the combustion conditions that will exist during application.

In order to quantify the behavior of these materials under rapid heating, a temperature jump (T-Jump) technique (~10^5 K/s) was applied to Al-CuO reactive nanolaminates. This approach involves resistively heating thin platinum filaments that

have been coated with the reactive multilayers. The ignition and reaction behavior of this material was observed with high-speed video and high temporal resolution time of flight mass spectrometry (TOFMS). The total thickness and the fuel-oxidizer equivalence ratio (experimental fuel to oxidizer mass ratio divided by stoichiometric fuel to oxidizer mass ratio) of the samples were kept constant so that the total energy of reaction of each sample (assuming each goes to completion) was the same. The number of layers was varied from 1 bilayer (i.e., one pair of a fuel layer and an oxidizer layer) up to 12 bilayers. This allowed us to probe the influence of interface-to-volume ratio and the average diffusion distance on the reaction properties.

The simple planar geometry of these systems is ideal for understanding and modeling the kinetics of the diffusion processes that controls reaction. Because of this, I was able to fit a straightforward, diffusivity-based model for ignition to the results. Such models create a foundation for condensed phase thermite reactions, which is important to a wide range of thermite applications. For example, arrested reactive milled (ARM) materials are also dense and restricted to condensed phase reaction and recent work has shown that porous nanopowder thermites follow a condensed phase pathway as well.[16,47,65,147,148] While the exact nature of the interfaces can vary between these materials, the results of this study may be applicable to a broader field than just the study of reactive nanolaminates.

7.2. Experimental Details

7.2.1. Sample Preparation

Nanolaminate layers were deposited onto a 76 μm diameter platinum filament using a dual magnetron sputtering chamber, which is discussed in Section 2.2.3 and in a previous publication.[61] Multilayer films were fabricated by the alternating the Al and CuO depositions allowing for 15 minutes between each deposition to allow the sputtering heat to dissipate. The sputter sources were 2" in diameter oriented 180° from one another with shuttered confocal sources. The sputter targets (Al and CuO) were acquired from Kurt Lesker. The CuO target was indium bound to a copper backing plate to assist in heat dissipation during the sputtering. CuO was sputtered using an RF power supply with 100 Watts of power with a sputter pressure of 0.27 Pa of argon (purity > 99.9999%). Aluminum was sputtered using a DC power supply at 20 Watts of power with a sputter pressure of 0.4 Pa of argon. In order to prepare radially uniform thin multilayer thermite films, the Pt wire substrates were rotated on an axis perpendicular to the plane of the magnetron sputter guns at a rotation rate of 6 revolutions per minute. Prior to deposition, the wires were cleaned via 15 minutes of ultrasonication in acetone and were then rinsed with deionized water, isopropyl alcohol, and methanol. They were mounted vertically and the center 10 mm of the wires were exposed to deposition where ~5 mm of the wire ends were masked to allow for Pt electrical contact needed by T-Jump analysis. The laminate morphology and thickness were characterized by scanning electron microcopy (SEM) cross-section analysis to obtain accurate deposition rates. The combination of small substrate diameter and rotation yielded deposition rates which were 40% lower in comparison to planar

deposition on a flat surface. The deposition rates were 3.7 nm/min and 3.3 nm/min for Al and CuO respectively. Reference samples prepared on flat surfaces using identical deposition parameters were analyzed by x-ray photoelectron spectroscopy (XPS) to estimate copper valence. The Cu $2p_{3/2}$ peak was routinely found to have shifted from 932.4 eV to 933.6 eV, which is consistent with CuO. Furthermore, satellite peaks were found at 961 eV, 941 eV, and 943 eV which are only consistent with Cu in its 2+ valence. X-ray diffraction (XRD) on the wire deposited samples (1 and 12 bilayer) confirmed that the phases were consistent with planar samples and invariant to number of bilayers.

All samples were deposited starting with the metal layer first and all had a total thickness of 1800 nm. At each interface between Al and CuO a pre-reacted barrier forms (typically 2-4 nm).[62,149] So while the total thickness of each sample was the same, the samples with more interfaces featured more barrier material, which would decrease the overall energy of the system. However, the impact of this was ignored as even for the sample with the most bilayers (12), this accounted for only a 5% decrease. The fuel-oxidizer equivalence ratio was maintained at 1.4, which is fuel rich.

7.2.2. Characterization

The T-Jump/ToF-MS experimental set up was the primary means to investigate ignition, the details of which is described in Section 2.2 and in previous papers.[38,52,55] The nanolaminate coated Pt filaments were heated resistively with 3 ms DC electrical pulses to ~1600 K. These pulses produced roughly linear heating rates of ~$4x10^5$ K/s. The voltage and current measured from the wire were used to determine the time resolved temperature based on the well-known relationship

between Pt resistivity and temperature.[150] This temperature was correlated to the behavior observed simultaneously with a high speed camera (Phantom v12.0, 67000 frames per second) and ToF-MS with spectra taken every 100 μs. The imaging allows for observation of visible combustion dynamics including overall optical intensity and ignition, which was considered as the first frame of sustained optical emission from the sample. After the first heating pulse and subsequent cooling, the wires were heated a second time to provide a background signal for video intensity and temperature.

Since Al deposited onto the platinum increases the net conductivity and the temperature is calculated from resistance, it is important to consider the impact of adding this initial layer. The cross-sectional area of a wire was 4.5×10^{-9} m^2 and the area of the thickest Al films (1 bilayer case) was 1.9×10^{-10} m^2, so the inclusion of the film represents only a 4% increase in area. But, given that the resistivity of Pt is ~5 times higher than bulk Al, this can decrease the overall resistance by 12%, which is significant, although the grain structure of the thin films may increase the resistivity and lessen the impact of this effect. Regardless, no ignition measurement was made for 1 bilayer (as will be discussed below), and the potential impact of this effect decreases to 6%, 4%, and 2% for the 2, 3 and 6 bilayers. Additionally this effect can be measured experimentally, with a comparison of the temperature of the experimental heating pulses and background pulses. The continuity and morphology of the Al layer would be destroyed by the experimental heating, so any effect on resistance would be removed for the background run. Thus if the diminished resistance from Al was significant, the experimental temperature reading at the start

of the heating pulse would be lower than the background case. This effect was noticed in the 1 bilayer case (~35 K difference in starting temperatures) and to a smaller degree in the 3 bilayer case (~15 K difference), but not in any of the other cases. As I did not use any temperature data from the 1 bilayer case, and the difference in 3 bilayers was small relative to experimental variation, this effect was ignored.

7.3. Results

A set of cross-sectional SEM images for the Al/CuO nanolaminate samples typical of this study is shown in Figure 7.1. The cross-sections, prepared by cutting a coated wire with scissors, reveal microstructures with a columnar appearance and coarse interface roughness. The roughness and degree of columnarity in the present samples is larger than is typical of Al/CuO films prepared on semiconductor substrates like Si.[15,86] Microstructures in the present samples have a coarsened morphology as result of the wire surfaces, which are orders of magnitude rougher than a Si substrate, and from the fact that some fraction of the deposition occurs off-axis (*i.e.*, deposition occurs on the sides and back side of the wire, but at a much slower rate than the leading surface). The kinetic energy of the species that deposit off-axis is lower and does not benefit from the additional atom mobility afforded by mild bombardment. The combination of these two effects produces this course grain morphology. Irrespective, the films are dense and continuous. It should also be noted, that the delamination visible in Figure 7.1a,d occurred during the cross-sectioning

process. Film further back from the cross-sectioned edge was well adhered to the Pt substrate as in Figure 7.1b,c.

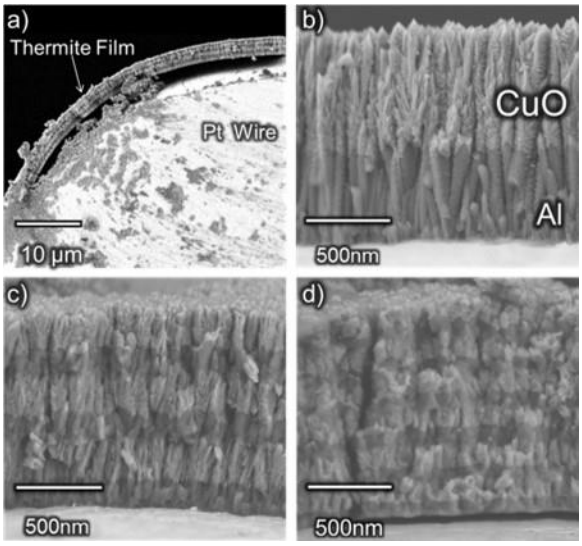

Figure 7.1. SEM images of Al/CuO nanolaminates coating Pt wires that were cleaved to show a cross-section. a) shows the curvature of the films as deposited. The visible deformation of the wire is a result of the cross-sectioning process. Higher magnification images of 1, 3, and 6 bilayer samples are shown in b), c), and d) respectively. All samples were deposited Al first and with CuO as the outermost layer.

For every sample, except the 1 bilayer nanolaminates, a clearly visible ignition and reaction could be observed from the high speed video. Figure 7.2 shows some frames taken from the high-speed video of experiments performed on 3, 6, and 10 bilayer samples. Each sample was subjected to a similar heating pulse, which means that the times indicated for each frame are proportional to the temperature of the wire at that instant. As can be seen, the 3 bilayer sample only reacted very weakly and at high temperatures. Comparatively, both the 6 and 10 bilayer samples reacted far more violently and at significantly lower temperatures. Based on these observations the samples could be grouped into two categories: weak and violent. The weak group was made up of the 1, 2, and 3 bilayer samples and was characterized by minimal emission and ejection of material from the wire. The violent group contained

the 6, 8, 10, and 12 bilayer sample, which all rapidly ejected large amounts of hot material from the wire surface as shown in Figure 7.2.

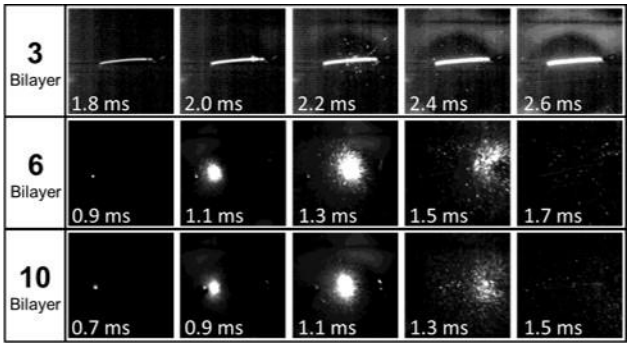

Figure 7.2. Frames from the high speed video of samples with 3, 6 and 10 bilayers. The brightness and contrast of the images for the 3 bilayer sample were digitally enhanced to make the reaction more visible. Frames shown were taken 0.2 ms apart and with 14 μs exposure time. The same scale was used for all images, with the bright wire in the 3 bilayer case being ~10 mm long.

The point of ignition is shown in the first frames for both the 6 and 10 bilayer samples in Figure 7.2. By correlating the time of this frame with the temperature data of the wire, the ignition temperature can be determined. For 2, 3, and 6 bilayers the ignition temperatures (+/- 50 K) were 1250 K, 1130 K, and 680 K respectively. The 8, 10, and 12 bilayer samples ignited at lower temperatures of 650 K, 670 K, and 620 K respectively. There is a general trend of decreasing ignition temperatures with increasing number of bilayers that appears to saturate for samples that have high interfacial area to volume ratios. As the total thickness of all samples was constant, the number of bilayers is inversely proportional to bilayer thickness, which has been found to be a controlling property for nanolaminate reaction.[62,151,152] In those terms, the weakly reactive 1, 2, and 3 bilayer samples had bilayer thicknesses of 1800 nm, 900 nm, and 600 nm respectively while the violently reactive 6-12 bilayer samples had thicknesses of 300-150 nm. Thus the comparative change in bilayer thickness

was much less significant from 6 to 12 bilayers, which could help explain the similar reactivity in the violent group and diminishing change in ignition temperature.

In order to better quantify the reactivity, the integrated intensity of each frame of the high speed videos was determined. This data was normalized by the peak intensity of the background run taken with a second pulse of each wire. Examples of this data as plotted temporally are shown in Figure 7.3. It should be noted that that there was some run-to-run variation in the shape and size of the peaks, but the ones shown are representative of the general trends observed. As mentioned previously, for 1 bilayer there was no ignition, which is reflected by the lack of any peaks in the intensity plot that are distinct from the background heating. Instead the signal has the same general shape as the background but slightly brighter. The increased brightness implies that some degree of exothermic reaction did occur, which led to a hotter wire. This was also reflected in the temperature profiles for these runs. The intensity profiles of 2 and 3 bilayer samples were similar to the 1 bilayer sample except with their ignition reflected by the small but distinct peaks prior to the end of the 3 ms heating pulse. They also reach higher peak intensities, suggesting more reaction occurring faster.

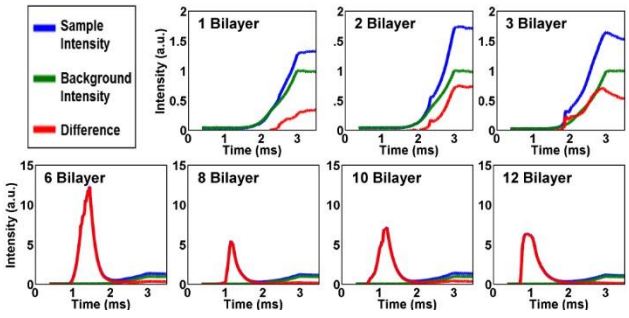

Figure 7.3. Integrated intensity taken from the frames of the high speed videos. Note the difference in scales between the two rows. The blue lines represent the heating and reaction of each sample, the

green line represents a second run of the same wire, and the red line represents the difference between those two results. All data is normalized by the peak of the background run.

The transition between the weak group and the violent group is apparent with the extreme jump in reactivity from 3 to 6 bilayers. Rather than the peak intensity coinciding with the end of the heating pulse, the samples with more bilayers had emission occurring prior to 2 ms that was 5-10 times larger than the background. One interesting feature of these plots is that the 6 bilayer samples featured the highest intensity, even though one might expect that the samples with the most bilayers would be the brightest and most reactive. Closer inspection of the images in Figure 7.2 reveals that while the 6 and 10 bilayer samples look similar, the visible material ejected from the 6 bilayer sample is coarser than that ejected by the 10 bilayer sample. Because of the camera settings, many of the pixels at the center of reaction were fully saturated. This means that the material thrown off the wire makes a disproportionate contribution to the integrated intensity measurement. Additionally, with finite camera resolution, finer bright material can get lost and larger bright material will contribute more to the overall intensity. As such, caution must be exercised when interpreting absolute intensity trends.

The transition in reactivity from weak to violent is also apparent in the mass spectra taken with the ToF-MS. Figure 7.4 shows the signal intensity of several species, along with the temperature of the wire for 3 and 6 bilayer sample runs. The mass spectra for the weak group (1-3 bilayer) were all qualitatively similar to the 3 bilayer case shown in Figure 7.4(a), with a major O_2 peak, whose onset (defined as 5% of maximum) occurred at 1050 (+/-50) K and preceded ignition (vertical dashed line). Samples that ignited prior to this O_2 release threshold (6-12 bilayer samples),

showed no or much less significant O_2 signals, which implies that the oxygen reacted with aluminum instead of being released to the chamber. It is likely that the oxygen signal observed for low bilayer samples resulted from the decomposition of the outermost layer of CuO ($2CuO \rightarrow Cu_2O+1/2O_2$). Such behavior has been observed to occur at 975 K in CuO nanoparticles under similar heating conditions, and is consistent with the relative stabilities of CuO and Cu_2O at high temperatures and low pressures.[38] Another significant feature of the low bilayer mass spectrum is the lack of significant peaks for the species that normally indicate reaction (e.g., Cu, Al_2O, AlO).[52,55] While Figure 7.4(a) does show some intensity for m/z=27 (labeled Al), there are organic compounds with that m/z (e.g., HCN, C_2H_3) that are more likely to be responsible as there were significant C, H, and N species detected at that same time (e.g., m/z=2, 12, 28, 44). The reason for this was likely surface contamination that occurred during handling.

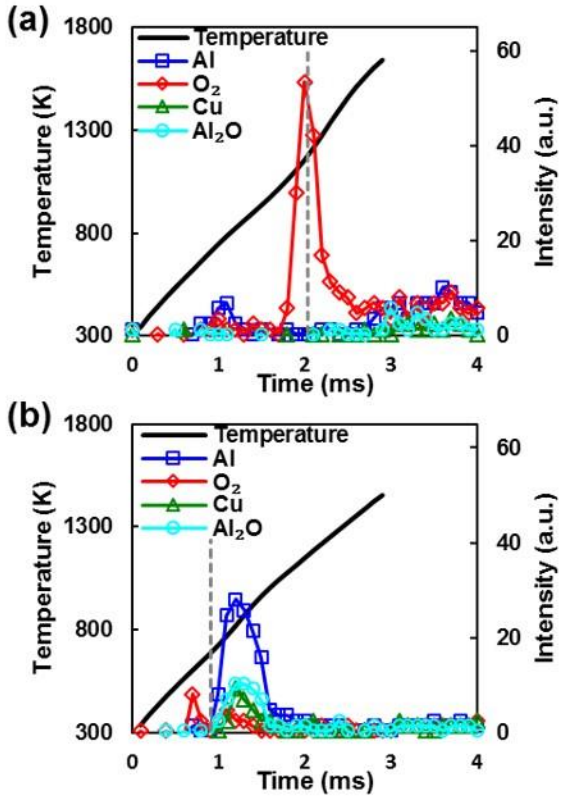

Figure 7.4. TOFMS results from experiments for samples with (a) 3 bilayers and (b) 6 bilayers. The vertical dashed line indicates the time of ignition as determined from high-speed video.

In comparison, the violent samples all showed spectra similar to the 6 bilayer case shown in Figure 7.4(b). These samples featured only minimal O_2 but had significant amounts of Al, Cu, and Al_2O. The onset of these peaks coincided with visible ignition observed with the high-speed camera. Since all the peaks shared the same profile and any organics contamination should have already decomposed, it is reasonable to assume that all these species were the supposed reaction products rather than organic contamination discussed above. For all samples with 6 or more bilayers, Al is the most significant vapor phase reaction species, which may at first seem unusual considering that CuO was the terminal layer in each case. However, at similar temperatures the equilibrium vapor pressure of Al is about twice that of Cu. Combining this information with the observation of violent delamination upon

ignition of these more reactive samples (see Figure 7.2) leads to a self-consistent understanding that upon ignition most of the multilayer material is ejected from the wire surface and the "history" of the initial layering sequence is lost. Thus, the high temperature properties of the constituent elements predominate the experiment.

In order to better understand the material being ejected, product collection was performed in a manner similar to that found in a previous paper.[148] A carbon tape substrate was positioned ~3 mm from the Pt filament, which was then heated at ~10^5 K/s. The product was analyzed using scanning electron microscopy (SEM) as is shown in Figure 7.5 for a 10 bilayer sample. Figure 7.5(a) shows the general product morphology, which is roughly spherical particles with average diameter of ~4 μm. Figure 7.5(b) shows a higher magnification of the product using backscattered electrons (BSE), which cause the heavier elements (Cu) to show up brighter. Energy dispersive X-ray spectroscopy (EDS) was used to confirm that the bright phase was copper and the darker phase was oxidized aluminum. The near spherical shape of the product particles indicate they are formed in a molten state, which is to be expected given that the adiabatic flame temperature for this system (~2800 K) is much higher than the melting point of Al_2O_3 (2345 K).[11] Also visible in this image, decorating the surface of the larger particle, are small nanoparticles (<50 nm) that were likely formed from vapor phase condensation.[148] This experiment was also performed on the 3 bilayer case, which showed the same characteristic morphologies but with far less material collected due to the less violent reaction.

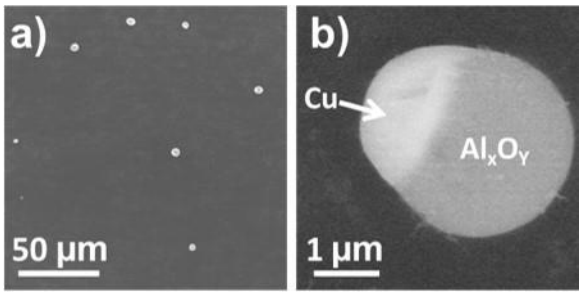

Figure 7.5. SEM images of product collected ~3 mm away from a 10 bilayer sample. (a) gives a view of the general morphology of the product. (b) is an image of a single product particle taken using backscattered electrons (BSE), which show heavier elements (Cu) as brighter.

7.4. Discussion

A primary benefit realized when studying reactive nanolaminates is that their geometrically simple embodiment facilitates studying and understanding the processes that controls reaction. Further, since they are dense, reaction can only occur through condensed phase diffusion. With these features in mind, I developed a model based on 1D diffusion for nanolaminate ignition. I focus only on the reaction leading up to the point of ignition, because as discussed above the violence of the ignition process destroys the morphology and changes the amount of interfacial area.

For this model, I assume a planar geometry as the thickness of the film (1.8 µm) is small compared to the diameter of the wire substrate (76 µm). I also assume that the entirety of the nanolaminate is isothermal with the wires. This is reasonable because there is good interfacial contact between the layers and the wire. Using the reported thermal diffusivities of Al and CuO ($8.3x10^{-5}$ and $5.1x10^{-6}$ m^2/s), a 1800 nm thick layer will have a characteristic time to thermal equilibrium (defines as length scale squared divided by the diffusivity) of ~40 and ~640 ns for Al and CuO respectively.[153] This is much faster than the 3 ms heating timescale of the wire. I also

assume that reaction is controlled by a diffusivity with Arrhenius behavior. This model focuses on the interfacial reaction that occurs leading up to the point of ignition, which is only a small portion of the overall reaction. Because of this I can neglect the oxygen loss that occurred prior to ignition in the 2 and 3 bilayer cases and the effect that the loss could have on the overall energy release of reaction. Any oxygen loss should occur from the surfaces open to the environment, which are farther than 100 nm from the reaction interfaces and thus should not affect the local interfacial oxygen concentration during the short timescale leading to ignition. Therefore, I can treat all samples the same despite the differences in reactivity discussed above.

From this basic framework I can model the change in temperature with the following three equations:

$$\frac{\mathrm{d}T}{\mathrm{d}t} = \frac{1}{C_p}\dot{Q}_{rxn} \qquad (7.1)$$

$$\dot{Q}_{rxn} = nA\ \Delta H_{rxn}\ J \qquad (7.2)$$

$$J = \nabla \mathrm{c}\ D_o\ e^{\left(\frac{-E_a}{RT}\right)} \qquad (7.3)$$

Equation 7.1 relates the temporal change in temperature to the rate of heat generation by reaction ($\dot{Q}_{rxn}$) divided by the heat capacity (C_p). The heat generated is evaluated in Equation 7.2, where n is the number of interfaces, A (m^2) is the surface area of each interface, ΔH_{rxn} (J/mol) is the energy released from each mol of reaction, and J (mol/(s·m^2)) is the flux of oxygen through each interface. The interfacial area, A, can be calculated based on a cylinder with the diameter of the wire to be $2.4\text{x}10^6$ m^2 for a 10 mm long film. The number of interfaces is related to the number of bilayers (N) through $n = 2N - 1$. While heat capacity is temperature dependent, the change is

relatively small over the range of ignition temperatures determined here. For simplicity, the value at the average ignition temperature (830 K) was used for all cases. Equation 7.3 is the Fickian diffusion flux through each interface, where ∇c (mol/m^4) is the concentration gradient across the interface, D_o is the pre-exponential to the diffusivity, and E_a is its activation energy. The concentration gradient is based on O anions going from zero to the concentration in CuO over the length of a typical interfacial Al_xO_y barrier layer (Δx_b~4 nm) to be 2.0x10^{13} mol/m^4.[62]

The process of achieving ignition is not well defined, but in these experiments ignition was observed as localized, very rapid increases in brightness that occurred discontinuously from the wire heating. As such, ignition marks a decoupling of wire and film temperatures, with the film temperature rapidly increasing above that of the wire. For this reason, I chose to define ignition temperature (T_{ign}) as the point at which the temperature rise from reaction (Equation 1) exceeds the heating rate from the wire (5x10^5 K/s). Combining Equations 1-3 and solving for ignition temperature gives:

$$T_{ign} = -\frac{E_a}{R}\left(\ln\left(\frac{(5\text{x}10^5\ \text{K/s})C_p}{n\ \nabla c\ \Delta H_{rxn}\ A\ D_o}\right)\right)^{-1} \qquad (7.4)$$

Apart from the two variables that define diffusivity (D_o and E_a), all other constants are well defined or can be reasonably estimated. Diffusivity is not as well known, because there is a wide range in the available data, and it is unclear which species is the primary diffusant. Therefore, the fit to the experimental data used D_o and E_a as tunable parameters. Additionally, all these values are temperature independent, except for concentration gradient (∇c), which would change as the

barrier layer (Δx_b) grows from reaction with $\nabla c(T) = \frac{\Delta c}{\Delta x_b(T)}$. The growth of the barrier layer is determined by the flux of oxygen ions, which thickens the Al_2O_3 side of the barrier and depletes oxygen from the CuO side. Therefore the change in barrier thickness can be written as:

$$\frac{d\,\Delta x_b}{dt} = J\left(\frac{1}{3}V_m^{Al_2O_3} + V_m^{CuO}\right) \qquad (7.5)$$

Here, $V_m^{Al_2O_3}$ and V_m^{CuO} are the molar volumes (m^3/mol) of Al_2O_3 and CuO respectively, and J (mol/(s·m^2)) is the flux as given in Equation 7.3. From this, with a known D_o and E_a, the barrier layer thickness can be modeled by numerically integrating with the constant heating rate. However, as the values of D_o and E_a are unknown to start, I employed an iterative model refinement approach to determining these parameters. To start, a constant concentration gradient was assumed and Equation 7.4 was fit to the experimental data, giving the values E_a=20 kJ/mol and D_o=9.0x10^{-13} m^2/s. Then the barrier layer growth was determined by numerically integrating Equation 7.5 with these parameters. Then a new fit was made based on a modified independent variable ($n\,\nabla c$) that combined the experimental number of bilayers with the concentration gradient predicted by the model for that value of n. This generated a new set of D_o and E_a that was used to start the next iteration. This process was continued until convergence, when the values for E_a and D_o remained constant through further iterations. More details on this procedure can be found in the Supporting Information Section 7.6.

The modeled ignition temperature is shown with the experimental data in Figure 7.6(a). The black solid line is the fit made from the assumption of a constant

concentration gradient (E_a=20 kJ/mol, D_o=9.0x10^{-13} m^2/s) and the dashed grey line is the result of the iterative refinement (E_a=49 kJ/mol, D_o=2.9x10^{-10} m^2/s) that takes into account the barrier layer growth shown in Figure 7.6(b). The barrier growth can be seen to be rather insignificant at the point of the lower ignition temperatures (~6 nm total thickness) but quite large by the upper end of the ignition range (~70 nm). The refined fit is slightly worse (R^2 coefficient of 0.91 vs. 0.94) than the other, but given the significant barrier accumulation over this range of ignition temperatures, it is a better representation of the physical process.

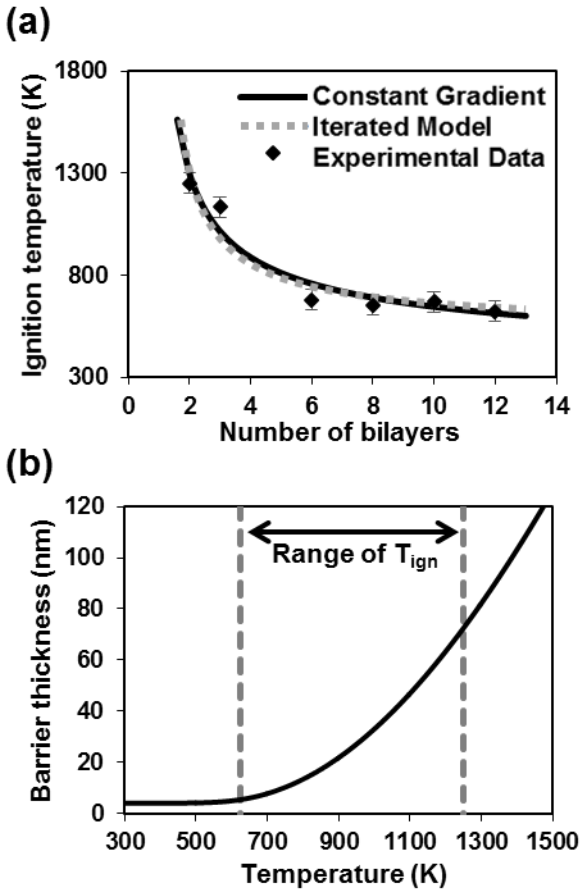

Figure 7.6. Results from the iteratively refined model. (a) shows the modeled ignition temperature with number of bilayers assuming a constant concentration gradient and from the refined model that included a dynamic gradient. (b) Shows the expected barrier layer growth determined from the numerical integration of Equation 7.5 and used in the iterated model fit shown in (a).

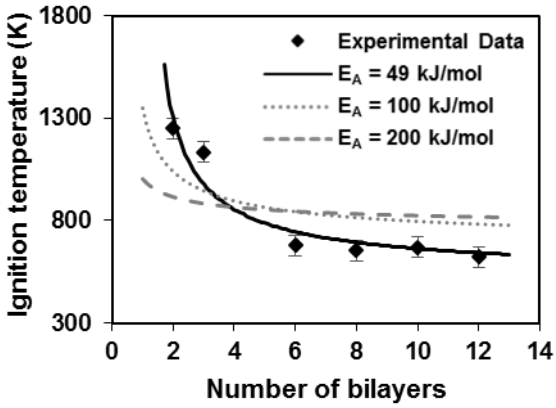

Figure 7.7. Experimentally determined ignition temperatures plotted with iteratively refined modelling results. The solid black line is the best fit model to the experimental data (E_a=49 kJ/mol, D_o=2.9x10^{-10} m^2/s). The dotted and dashed lines shown are model results with activation energies of 100 and 200 kJ/mol respectively, using D_o=1.2x10^{-7} m^2/s and D_o=1.3x10^{-1} m^2/s.

Figure 7.7 illustrates the sensitivity of this model to activation energy. The dashed and dotted lines represent the best fits that can be achieved (using the iterative refinement and oxide growth) when restricting E_a to 100 and 200 kJ/mol respectively. Assuming a higher activation energy results in energy release becoming far more sensitive to temperature, which in turn decreases the sensitivity to the number of bilayers. This effect is clearly seen in Figure 7.7 (dashed line) for E_a= 200 kJ/mol, where ignition temperature is relatively flat, meaning it is only weakly dependent on number of bilayers. With this in mind it is surprising that the value for E_a found here is so low, because the controlling process to ignition is presumably diffusion through the Al_2O_3 layer that forms between components during deposition.[61,62,145] While there is a wide range of values for the various diffusion mechanisms in Al_2O_3, activation energies are typically 200-600 kJ/mol.[154] However, most data on diffusivity in alumina is for the α phase, while the barrier layer that forms in nanolaminates is amorphous.[61,62,145] More recent results have shown a lower activation energy (116 kJ/mol) for that diffusion of oxygen ions in amorphous Al_2O_3, but even that is still

significantly higher than the value found here.[155] Previous results have shown that high heating rates can lead to a reduction in activation energy, although the exact origins of this low activation energy remains to be determined and will be a focus of further study.[135]

Regardless of how this occurs, these results imply that, at the high heating rates, condensed phase kinetics can be faster than what would be expected from reference diffusivity values. This could help explain some of the confusion over nanoparticle thermite combustion, where low diffusivities have been used to rule out certain modes of combustion.[20] These reactive nanolaminate results suggest that a condensed phase mechanism is fast enough to be responsible for the reactivity observed in nanoparticle thermites, given sufficient interfacial surface area. Both systems being driven by the same mechanism is further supported by the similarity between the product morphology shown in Figure 7.5 and that collected from Al/CuO nanoparticle reaction.[148]

As a final point, I discuss the implications of these results in terms of applications more general than uniform heating. In particular, I want to relate this data to freely propagating combustion measurements of flame speed that are commonly used to gauge reactivity.[62,151,152] To do so, I consider flame propagation as essentially a series of sequential ignitions and neglect any reaction prior to that point. Given some length (Δx) of nanolaminate, the amount of energy needed to reach ignition is proportional to the ignition temperature (T_{ign}). In keeping with the previous discussion of ignition, I assume that it occurs when the segment of film reaches a critical reaction rate on a per mass basis, with the number of bilayers

controlling the temperature at which that value is reached. Since this heat production at the point of ignition is bilayer independent, it is reasonable to assume that the heat flux forward into the cold film from that point is also constant, which implies a constant thermal gradient. Making this assumption, the time to reach ignition (Δt) will also be proportional to ignition temperature. This is represented schematically in the temperature versus time plot in Figure 7.8. The flame speed is the speed of the ignition front, which is then just $\Delta x/\Delta t$.

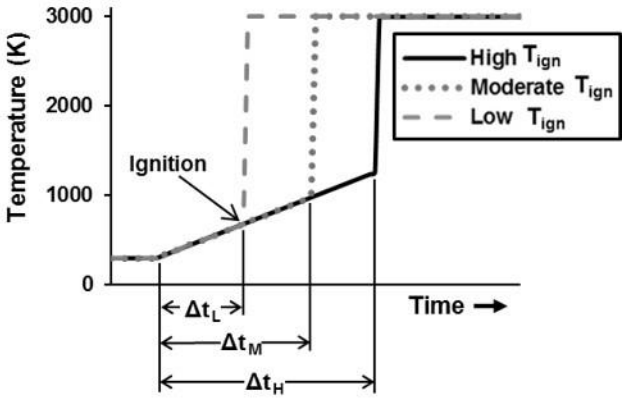

Figure 7.8. Schematic representation of the temperature profiles of some segment (Δx) of reactive foil as the flame front moves across it. The different lines represent the effect of different ignition temperatures on the timescale of ignition. Δt_{L}, Δt_{M}, and Δt_{H} are the time needed for a foil segment to reach a low, moderate, and high ignition temperature respectively.

Based on this approach, I calculate flame speed by taking the conductive heat flux and dividing it by the energy needed to reach ignition ($(W/m^2)/(J/m^3)$ → m/s). For simplicity, I assume that the heat flux is independent of bilayer thickness and estimate it based on Fourier's Law. I use the thermal conductivity of Al (240 W/mK) and base the constant thermal gradient on a temperature rise from 300 K to 650 K (the lower bound ignition temperatures) over a distance of 1 μm (chosen to fit data). The energy needed to reach ignition, is based on the change in standard enthalpy of formation from room temperature to the ignition point. The results of these

calculations are plotted in Figure 7.9 along with flame speed data for sputter deposited Al/CuO nanolaminates reported by Bahrami et al.[62] The values calculated here from ignition temperature show the same trend as the experimentally determined values. This suggests the flame speed, ignition temperature, and bilayer thickness can all be directly correlated to one another. As the amount of interfacial area per unit mass increases, ignition temperature falls while flame speed rises rapidly. This trend occurs because thinner bilayers have less mass per reacting interface, which promotes faster self-heating at lower temperatures. Further, the agreement shown in Figure 7.9 reflects that the heating rates used in these experiments (~10^5 K/s) sufficiently reproduce the kinetics of combustion.

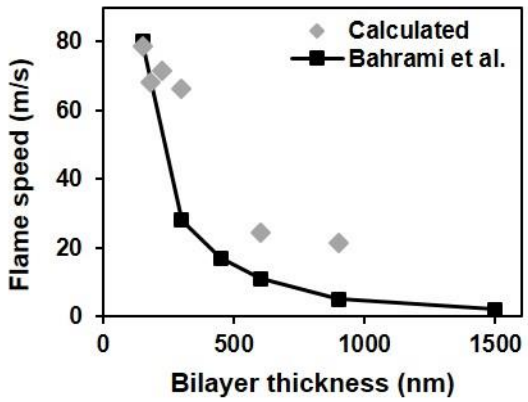

Figure 7.9. Flame speeds as calculated from the experimentally determined ignition temperatures. Also shown are experimental flame speed results as reported by Bahrami et al.[62]

7.5. Conclusion

Al/CuO reactive nanolaminates of a constant thickness but varied number of bilayers were sputter deposited onto Pt filaments. These filaments were heated at ~4x10^5 K/s and the reactivity was characterized with high speed video and ToF-MS. Increasing the number of bilayers, and thus deceasing bilayer thickness, was found to

enhance reactivity and lower ignition temperature. For samples with fewer than 3 bilayers, only O_2 and no other species expected from reaction were detected with mass spectroscopy. In comparison, the strongest signals for samples with 6 or greater bilayers were Al, Al_2O, and Cu. A simple diffusion based model was developed and fit to the experimentally determined ignition temperatures. From this model it was determined that a low activation energy (50 kJ/mol) was likely controlling the ignition process. With similar analysis, the experimentally determined ignition temperatures were used to calculate flames speeds. The results of these calculations were found to be in good agreement with experimentally determined values.

Acknowledgments

Work conducted by M.R.Z and G.C.E has been supported by the Army Research Office (Ralph Anthenien) and the Defense Threat Reduction Agency. J-P.M and E.J.M. acknowledge Ralph Anthenien and the U.S. Army Research Office for financial support under contract W911NF1310493. I acknowledge the support of the Maryland NanoCenter and its AIMLab.

7.6. Supplemental Information

As the temperature dependence of the concentration gradient (∇c) prevents a neat analytical solution for ignition temperature, an iterative refinement approach was employed. An initial approximation of a constant gradient was used as a starting point. Fitting the experimental data with Equation 7.4 from the text gave the

activation energy E_a and D_o of 20 kJ/mol and 9.0x10^{-13} m^2/s. This was then used to numerically integrate Equation 7.5 to determine barrier layer thickness, which relates to temperature dependent concentration gradient as : $\nabla c(T) = \frac{\Delta c}{\Delta x_b(T)}$. To incorporate this data into the next fit, the concentration gradient was considered a function of bilayer thickness using the relationship between T and n from Equation 7.4. The experimental number of bilayers (N_{exp}) was then transformed into $n\nabla c = (2\ N_{exp} - 1) * \nabla c(N_{exp})$. The effect of a temperature (and thus N) dependent concentration on this transformation is shown in Figure S7.1. Figure S7.1(a) used the constant concentration gradient based on the initial 4 nm barrier, while Figure S7.1(b) used a gradient based on the barrier growth shown in Figure 7.6. Equation 4 was then fit based on this modified experimental data to determine E_a and D_o, which were then used to start the next iteration. How these values change with number of iterations is shown in Figure S7.2. As can be seen, they converge before ~10 iterations. The same trend is true of R^2 coefficient, which is shown in Figure S7.3.

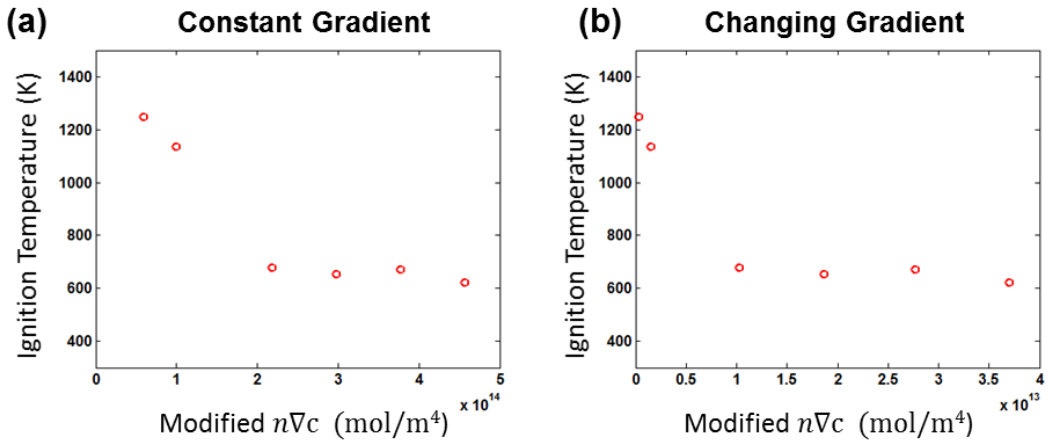

Figure S7.1. The experimental ignition temperatures versus number of interfaces modified by (a) a constant concentration gradient and (b) a temperature dependent concentration gradient based on the barrier thickness derived from the model.

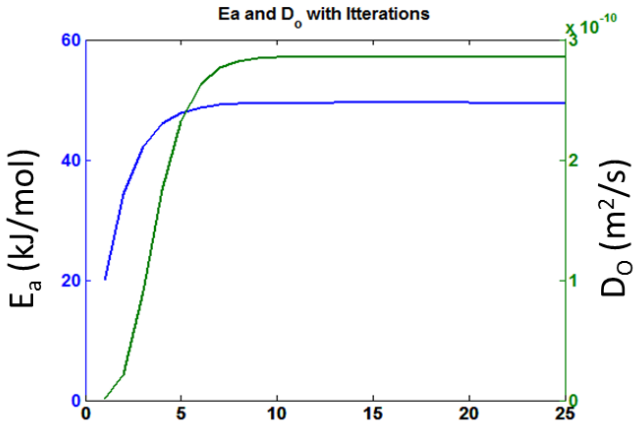

Figure S7.2. The effect of iteration on the values of E_a and D_o.

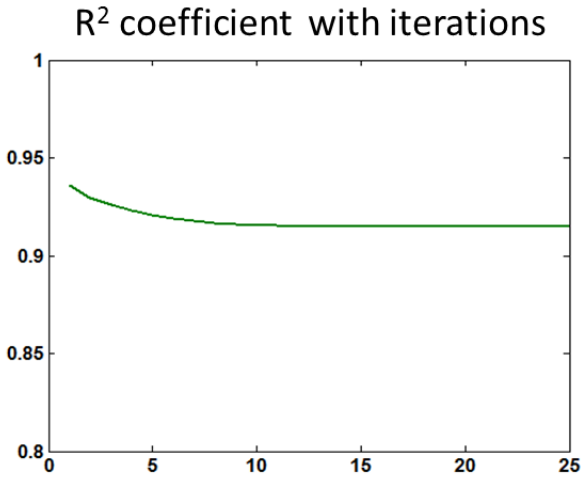

Figure S7.3. The effect of iteration on the R^2 coefficient.

Chapter 8: The Effect of Gaseous Oxygen and Total Gas Production on the Behavior of Nanocomposite Thermite Reactions: Comparison of CuO and Cu_2O as Oxidizers.*

Summary

The importance of gaseous oxygen and total gas production in nanocomposite thermite combustion was investigated by probing the reaction and ignition properties of aluminum nanoparticles (Al-NPs) with both cupric oxide (CuO) and cuprous oxide (Cu_2O). The gas release and ignition behavior of these materials were tested with $>10^5$ K/s temperature jump (T-jump) heating pulses in a high temporal resolution time of flight mass spectrometer (ToF-MS) as well as in an argon environment. Reactivity was tested using a constant volume combustion cell with simultaneous pressure and optical measurements. A variety of Cu_2O particle sizes ranging from 200-1500 nm were synthesized and found to release oxygen between 1150 K and 1250 K, which is higher than the values found for a variety of CuO particle sizes (~1000 K). Both oxides were found to ignite around 1000 K, which implies that the ignition mechanism was consistent for both and occurred through a condensed phase pathway. CuO thermites were found to be orders of magnitude more reactive, which implies that gaseous species play a critical role in the combustion process. Differences in reactivity between argon and vacuum environments and the use of Cu diluent to simulate Cu_2O, suggest that it

* The results presented in this chapter are in the process of being submitted to the Journal of Physical Chemistry C under the title "Gaseous Oxygen and Total Gas Production on the Behavior of Nanocomposite Thermite Reactions" with authors Egan, G. C.; Sullivan, K. T.; Olson, T. Y; Han, T. Y. J.; Zachariah, M. R.,.

I would like to thank my co-authors in that paper for all their hard work and input that made the paper and this chapter possible.

is the intermediate product gas, O_2, that plays the most significant role in combustion as an enabler of heat transfer and a secondary oxidizer.

8.1. Introduction

Energetic materials are one of the many areas of research that have seen remarkable gains with the emergence of nanoscale materials and technologies. In particular, the reactivity of thermites, which are highly exothermic mixtures of metal oxide oxidizers and metal fuels, has been increased by several orders of magnitude up to flame speeds of ~1000 m/s through the use of nanoparticles.[12] This increase is generally thought to result from reduced transport distances and increased specific surface areas of nanoscale materials. However, the rapid kinetics, high temperatures, dynamic morphologies, and multi-phase nature of these systems has limited our understanding of the mechanisms that control combustion. As a result, there are still many questions that remain about these systems including how choice of oxidizer affects the reaction process.

Generally, it has been shown that systems that produce a significant amount of gaseous species perform best in terms of reactivity.[7,10,13,26,27,156] Gases are thought to be important from a convective and advective heat transfer standpoint, as high pressures gradients can transport energy by moving hot gases and materials through the material into the unreacted zone.[27,35,36,157] In thermites, intermediate gaseous species can originate from the decomposition or sublimation of the metal oxide and its suboxides. Later-time gases form as the reaction proceeds to completion and produces some fraction of volatile products. Exactly when intermediate and product

gases form in respect to the overall reaction process and how they contribute to a propagating reaction are still unknown, as probing these materials dynamically with sufficient spatial and time resolution can be challenging. The exact nature of these gases will also be dependent on the oxidizer used, as there are a wide variety of gas-generating oxidizers which have different sizes, morphologies, decomposition pathways, densities, and enthalpies of formation. Directly comparing two oxidizers is complicated when one accounts for all of these parameters. For this reason, I sought to choose a set of oxidizers that share as many properties as possible, CuO and its reduced form Cu_2O, in order make direct comparison in this study. Here, these materials have been synthesized and purchased to have similar morphologies and cover a wide range of sizes in order tweeze out and separate the impact of these properties on the two systems.

Although CuO-Al has almost twice the specific energy and energy density of Cu_2O-Al (4.08 kJ/g and 20.8 kJ/cc vs. 2.41 kJ/g and 12.7 kJ/cc), these formulations yield the same adiabatic flame temperature of 2843 K, which is dictated by the boiling point of Cu.[101] Major equilibrium products for both are liquid Al_2O_3 and Cu, along with gas-phase Cu. In the case of CuO-Al, the higher energy density allows for a much larger fraction of Cu to be vaporized. This difference in equilibrium gas production is the only significant difference between the two systems, thermodynamically.

While equilibrium calculations are useful to give us some idea of the final temperature, pressure, and composition, it has become more apparent recently that gaseous intermediate species may play a more dominant role in governing ignition

and reaction processes. In particular, CuO is predicted to undergo decomposition to Cu_2O and release O_2 at a relatively low temperature, with the onset temperature generally shifting to lesser values as the atmospheric pressure decreases. Using time-resolved mass spectrometry, is been previously shown that rapidly-heated ($>10^5$ K/s) nanoparticles of CuO release O_2 at approximately 975 K.[38,55] Cu_2O can further decompose to Cu and additional O_2, but this will occur at a higher temperature according to thermodynamic predictions. Therefore, a second significant difference between the two materials, is that CuO has a low temperature gas-generation event as it decomposes into Cu_2O and liberates O_2 gas. What, exactly, is the benefit of this gas-generation step to ignition and combustion processes is a main question being addressed in this work. Furthermore, I am interested in what, if any, role does the size of the metal oxide play in contributing to the dynamic O_2 release.

To that end, CuO and Cu_2O particle sizes between 30 nm and 5 μm were mixed with nanometric aluminum. The ignition and transient O_2 release profiles were investigated in these materials at high heating rates using a combination of time of flight mass spectrometry (TOFMS) and high-speed video at both atmospheric and vacuum conditions. Pressurization and optical measurements were performed using a constant volume combustion cell to characterize combustion behavior.[45]

8.2. Experimental Details

8.2.1. Materials

Cu_2O was synthesized using a method by Huang *et al* that was scaled up to produce a larger quantity.[158] A one liter volume, glass reaction vessel with a heating jacket set at 33.5 °C was used to heat and stir 860 mL of milli-Q water (18.2 MΩ) and 5 g sodium dodecyl sulfate (OmniPur by VWR). 20 mL of 0.1 M copper(II) chloride anhydrous (99% by Acros Organics) was then added to the solution. 9 mL of 1 M sodium hydroxide (VWR) was subsequently added at which point the solution turned a light blue hue, indicating the formation of copper(II) hydroxide. After approximately a minute, 80 mL of 0.1 M hydroxylamine hydrochloride (99% by Alfa Aesar) was added to the reaction vessel. The stirring (via magnetic stir bar) was stopped and the Cu_2O particles were kept in the heated reaction vessel and allowed to grow for one hour. After the one hour growth process, the Cu_2O particle solution was poured into four large (500 mL each) centrifuge tubes. The particle solution was centrifuged (Sorvall GS-3) at 9000 rpm for 15 minutes. The supernatant was removed and replaced with ethanol and the Cu_2O particle pellet was resuspended using ultrasonication and vortex mixing. This cleaning process was repeated 3 times. Organics remaining from the synthesis process made up ~5% of the final weight of the material as determined by thermogravimetric analysis (TGA).

CuO was produced from the synthesized Cu_2O through oxidation, by holding the material at 250ºC in air for 2 hours. Conversion was confirmed through X-ray diffraction (XRD) and accompanied by a distinct color change from orange to black. Example XRD patterns are shown in the supporting information Figure S8.1.

Aluminum nanoparticles (Al-NPs) of average size 50 nm were used as purchased from the Argonide Corporation. They were considered 70% active by mass as a result of a ~3 nm native oxide shell. CuO was purchased from Sigma Aldrich as a nanopowder (<50 nm primary particle size) and micron scale powder (<5 μm). Additional Cu nanopowder (60-80 nm) was also purchased from Sigma Aldrich for use as a diluent.

Thermites were prepared stoichiometrically accounting for the oxide shell but not the organics on the Cu_2O. The samples were mixed with ultrasonication in hexane.

8.2.2. Characterization

Oxygen release and ignition were studied with temperature jump (T-Jump) wire heating capable of rates of ~$3x10^5$ K/s as described in Section 2.2. Material was deposited from solvent suspensions onto thin (76 μm) platinum wires that were resistively heated with 3 ms electrical pulses. By measuring the current and voltage of the wire during the pulse, the temperature was calculated based on a well-known relationship for platinum resistance.[159] Oxygen release was analyzed with a time of flight mass spectrometer (TOFMS) that recorded spectra every 100 μs. Details of this experimental set up are described in in Section 2.2.2 and can also be found in previous papers.[38,52,55] Ignition was monitored with a high speed camera (Phantom v12.0, 67000 frames per second) in both the TOFMS and a chamber that was used for argon environment experiments. In such experiments, the chamber was evacuated with a mechanical pump, purged with Argon flow, and then closed off to maintain 1 atm of Argon.

Reactivity was quantified by igniting 25 mg of material in a constant volume (13 cc) combustion cell capable of simultaneous optical and pressure measurements, the details of which can be found in Section 2.3 and a previous publication.[45] At least two runs were performed for each material.

8.3. Results

Examples of the synthesized Cu_2O nanoparticles are shown in Figure 8.1(a-d). As can be seen, the synthesis produced fairly monodisperse material over a wide range of sizes. The smaller particles tended to have less spherical morphologies in a manner consistent with previous studies of this synthesis method.[158] Figure 8.1(e,f) shows the CuO that resulted from oxidation of the material shown in Figure 8.1(a,b) respectively. While many particles remained roughly the same through oxidation, there was also significant morphological change that produced surface roughness and smaller irregularly shaped particles. As a result the specific surface area increased during the oxidation, with 360 nm particles going from a BET surface area of 4.8 m^2/g to 6.9 m^2/g.

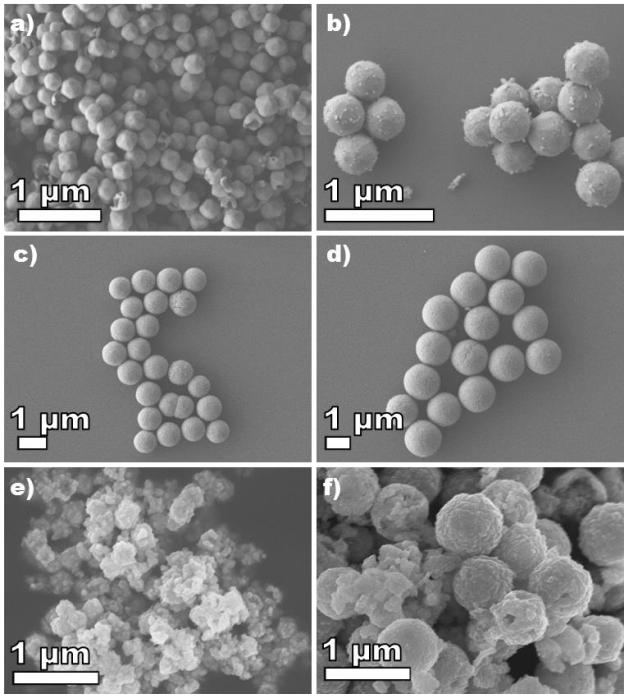

Figure 8.1. Scanning electron microscope (SEM) images of Cu_2O (a-d) synthesized for this study and the CuO (e,f) produced by oxidizing the material. The average Cu_2O particle diameter as determined from SEM analysis was 200 nm, 390 nm, 850 nm, and 1510 nm for a-d respectively. Images in (e) and (f) are the results of oxidation (250°C in air for 2 hours) of the material shown in (a) and (b) respectively.

As mentioned above, CuO and Cu_2O have significantly different decomposition behaviors, which control how they release gaseous oxygen. Equilibrium calculations done with CHEETAH at $5x10^{-9}$ atm (approximately the vacuum of the mass spectrometer) predict that CuO will decompose into Cu_2O and O_2 at 800 K and that Cu_2O will decompose into Cu and O_2 at 1150 K. This behavior was studied experimentally using the T-jump ToF-MS at heating rates of ~$3x10^5$ K/s. The mass spectra for these materials revealed that there was significant surface contamination for all the oxides used, as significant H_2O and CO_2 peaks were visible during the early stages of heating (500-1000 K). Representative O_2 species intensity are shown for both oxides and the corresponding thermites in Figure 8.2. Using the wire temperature measurements, the onset of O_2 release corresponds to temperatures

of 1050 K for CuO and 1170 K for Cu_2O. This difference is not as significant as predicted by the equilibrium calculations, which points to the fact that this process is likely kinetically limited as has previously been reported for CuO at high heating rates.[52]

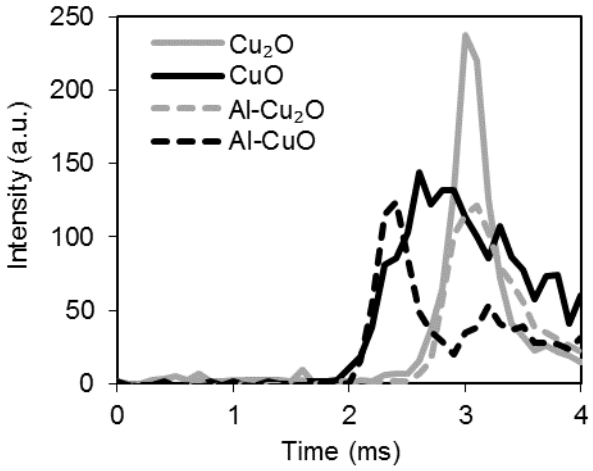

Figure 8.2. Example O_2 release profiles for the different oxides along with the corresponding thermite. The Cu_2O had a diameter of 320 nm and the CuO was the oxidized version of that material. All samples were heated with similar pulses (~$3x10^5$ K/s). The point of O_2 release was 1050 K and 1170 K for the CuO and Cu_2O respectively.

Along with the O_2 release temperature, high speed video was used to record the reaction of the thermites. This allowed for the determination of an ignition temperature as defined by the onset point of optical emission. However, the Cu_2O-Al reaction was found to be only weakly reactive in the vacuum of the mass spectrometer, making it difficult to distinguish the onset of reaction. Interestingly, when heated under 1 atm of argon, the same material was found to be far more reactive. This difference is shown in Figure 8.3, where the integrated optical intensity from each video frame is plotted versus time with the background intensities of the blank wires (taken by pulsing the wires a second time) subtracted out. Values are normalized to the peak value of the background run. The frames with peak intensity are also shown for reference.

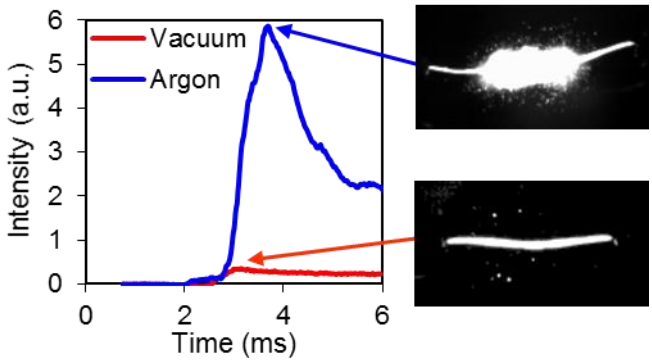

Figure 8.3. Integrated intensity of Cu_2O-Al (440 nm) reaction in vacuum (red) and argon (blue). Both sets of data are normalized by the peak intensity of a background run of the same wire used in the experiment, which is then subtracted out. Also shown are frames from the video corresponding to the peak visible reaction.

The measured oxygen release temperatures of neat CuO and Cu_2O are plotted along with the ignition temperature of the corresponding thermite in argon in Figure 8.4, as a function of oxidizer particle size. Each data point represents the average of at least 2 runs. The maximum uncertainty based on experimental variation was ±50 K and that was used as a conservative estimate for all data. It should be noted that the size of the synthesized CuO samples was taken to be that of the precursor Cu_2O before conversion to CuO, although, as I discussed earlier, this process led to changes in both size and morphology (see Figure 8.1). As can be seen in Figure 8.4, all of the CuO materials (filled symbols) have consistent ignition temperatures within 100 K of the corresponding O_2 release temperatures. In comparison, Cu_2O (hollow symbols) thermites ignited ~200 K before the oxide released O_2. Taking an average over all sizes, CuO and Cu_2O released oxygen at 1020 K and 1200 K respectively, while with Al-NPs CuO and Cu_2O ignited at 970 K and 980 K respectively. Another interesting feature of note is that there is no apparent size dependence on either O_2 release temperature or ignition temperature. Thus, it seems that the initiation of these process are not limited by total specific surface area for the studied range of particle sizes.

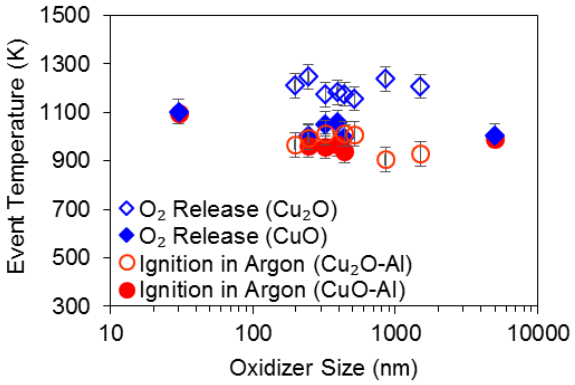

Figure 8.4. Oxygen release and ignition temperatures for the range of sizes tested. The blue diamonds represent the O_2 release from the oxidizer and the red circles are ignition in with Al-NPs in argon. The hollow symbols are for Cu_2O and the filled symbols are for CuO.

Combustion results from the constant-volume pressure cell experiments are shown for Al mixed with commercial CuO (30 nm and <5 μm) and synthesized 850 nm Cu_2O in Figure 8.5. The results show that CuO-Al was generally orders of magnitude more reactive than Cu_2O-Al. As can be seen for both pressure and optical signals, the nano CuO was the fastest material, with the micron CuO being about 2 orders of magnitude slower and the Cu_2O being an order of magnitude slower than that. Five different sizes of Cu_2O (190, 250, 390, 850, and 1500 nm) were tested and all showed similar behavior to the 850 nm sample shown in Figure 8.5. In particular, the run to run variation was more significant than sample to sample, suggesting that there is no significant size dependence for Cu_2O from 200 nm to 1500 nm as is shown in Figure S8.2 and Figure S8.3 in Section 8.6-Supplemental Information. The synthesized CuO (from oxidation of Cu_2O) of the sizes tested (original sizes 320 nm and 440 nm) performed nearly identically to the commercial nano CuO in terms of peak pressure and rise time, although there were noticeable features in the optical signal at later times. This can likely be attributed to the wide distribution of sizes that

resulted from oxidation (see Figure 8.1(e,f)), with the larger material reacting and emitting at later times.

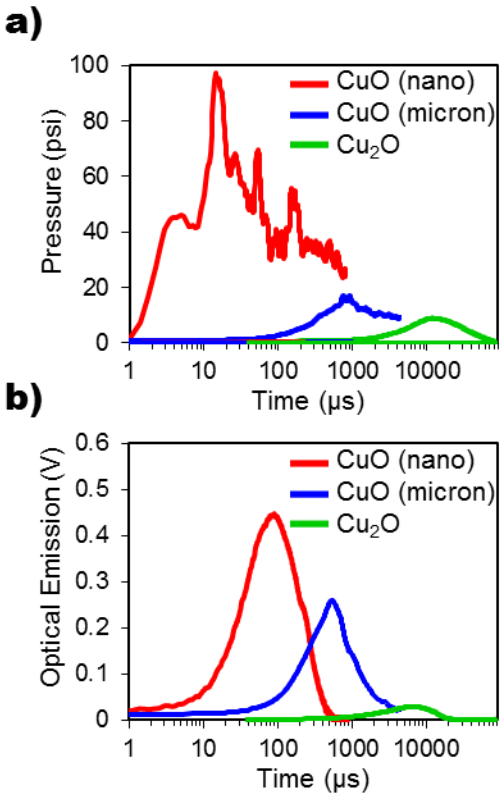

Figure 8.5. Results from reacting Al-NPs with the various oxidizers in a constant volume combustion cell. (a) shows the pressure response and (b) shows the optical emission. Note the logarithmic scale of the x axis. Nano and micron CuO refer to the commercial material with primary size 30 nm and 5 μm respectively.

To quantify these differences in reactivity, the key values are peak pressure, pressure rise time (i.e., time to peak pressure), and the burning time (full width at half maximum of optical signal). All of these values, as well as the key results from the T-Jump experiments, are summarized in Table 8.1. Since there was no observable size dependence, the Cu_2O values are averaged together. A significant drop in peak pressure was observed moving from nano to micron CuO (110 psi to 20 psi), and a further reduction when using Cu_2O, which had a peak pressure of just 8 psi. In terms

of burning time, nano CuO and synthesized CuO were approximately the same, with micro CuO lagging behind some. Cu_2O, in all cases, was dramatically slower than all CuO samples.

	T-Jump experiments		Combustion cell experiments		
	O_2 release temperature (K)	Ignition temperature (K)	Peak pressure (psi)	Pressure rise time (ms)	Burning time (ms)
nano CuO	**1030** (±50)	**990** (±50)	**110** (±16)	**0.012** (±0.002)	**0.28** (±0.1)
synthesized CuO	**1030** (±50)	**960** (±50)	**100** (±8)	**0.019** (±0.006)	**0.33** (±0.12)
micron CuO	**1000** (±50)	**990** (±50)	**20** (±4)	**0.75** (±0.1)	**0.86** (±0.3)
Cu_2O (average)	**1200** (±50)	**980** (±50)	**8** (±1)	**12** (±2)	**11** (±3)

Table 8.1. Quantified results of the different experiments with Al-NPs and the various forms of oxidizer.

8.4. Discussion

There are several interesting findings in this work that can be summed up as follows:

a) Cu_2O-Al thermite ignites at exactly the same temperature as CuO-Al, despite its O_2 release temperature being approximately 200 K higher.

b) There is no scaling of ignition temperature or oxygen release behavior with oxidizer particle size between 30 nm and 5 μm.

c) Cu_2O-Al thermites reacted poorly under vacuum and more violently at atmospheric pressure in Argon.

d) Nano-CuO, both commercial and synthesized, is the strongest oxidizer. Micron sized CuO yields about 5x less pressure and produces longer pressure rise time and burning time by factors of about 60 and 3 respectively. Cu_2O

was the poorest oxidizer, with significantly reduced pressure and much longer pressure rise and burning times than even the micron CuO.

The first point is a clear indication that the ignition process occurs directly through the condensed phase without the need for gaseous oxygen. For the CuO-Al case, given the proximity of ignition and O_2 release, it is possible that the primary interfacial reaction is between Al and the reduced form of CuO (i.e., Cu_2O), which would explain the similar ignition temperature. Such behavior was observed with *in situ* dynamic transmission electron microscopy (DTEM) experiments, where reaction proceeded only after decomposition of CuO (see Chapter 5).[79] Whether this truly happens during full scale reaction, and to what extent, would require further work and ultimately depends on the decomposition rate and time scale of liberating O_2 from the oxidizer relative to the interfacial reaction time scale.

The lack of a size dependence for ignition is a very interesting finding and seemingly goes against previous results that showed ignition temperature is directly related to the amount of interfacial area in Al/CuO nanolaminates (see Chapter 7).[160] However, unlike the straightforward laminar structure of those material, the relationship between the size of the components and interfacial area is not as clear cut for nanoparticles. Spherical particles are limited to only small amounts of interfacial contact compared to their total surface area and the complex aggregation that occurs in nanoparticles will further limit the amount of area in contact. Additionally, it has been shown that both Al and CuO nanoparticle aggregates will coalesce in <100 ns upon heating, which is much faster than other timescales found for combustion (see Chapter 4 and Chapter 5).[54] Therefore, the actual size of the particles during the initial

stages of reaction could be significantly larger than their starting size. For all these reasons, the initial size of the oxidizer may not have as big and impact on fuel/oxidizer interfacial area as might be expected.

The observation that Cu_2O did not react nearly as well under vacuum as it did at atmospheric pressure suggests that the gases liberated during combustion play an important role in determining overall reactivity. In vacuum, a significant portion of the gases will diffuse out of the reacting material, while a pressurized argon environment will slow the diffusion and leave the evolved gases in the reaction zone for longer. Given that both oxidizers have been shown to release O_2 during reaction, it follows that secondary oxidation with intermediate O_2 is responsible for sustaining a strong reaction. In the case of vacuum, what little O_2 does get liberated by Cu_2O will simply not have enough time to fully react with Al before it is transported out of the thin thermite layer on the wire. Under atmospheric pressure, the gases do not get transported out of the reacting film of nanoparticles nearly as fast, and the reaction has time to fully develop. In comparison to the reduced oxide, CuO can react violently in a vacuum, which suggests that it can produce O_2 fast enough to sustain a localized oxidizing environment, even with significant gas loss. However, as with Cu_2O-Al, the reaction of CuO-Al is enhanced by the presence of an argon environment, which causes the reaction to be much brighter and to last longer as is shown in Section 8.6-Supplemental Information with Figure S8.4. This is further evidence that localizing the produced gases enhances reactions and points towards a slower (on the order of ~2 ms) secondary reaction with gaseous oxygen accounts for a significant portion of the overall energy release. The general process of fast O_2 release

followed by heterogeneous reaction has been previously supported for nano CuO-Al based on the sharp pressure rise that precedes the peak of the optical signal in combustion cell experiment as well the long (~3 ms) burning that occurs well after the initial fast flame front has passed in burn tubes.[29,30,45]

To address the final point listed above, the poor pressure cell performance of the Cu_2O-Al cannot be attributed to the size, as it was consistent across a wide range, and is unlikely a result of condensed phase reaction rate, which should be the same mechanism as for CuO as discussed above. Therefore, it must be considered whether it is the diminished presence of a secondary oxidation source (O_2) that is responsible for the greatly reduced reactivity or if it is another factor related to gas release. Gases generated by reaction will play other important roles in the combustion process, particularly in regards to heat transfer, which is generally thought to be controlled by large pressure gradients driving hot gases and condensed phase material forward into the unreacted zone.[27,35,157] Strong gas generation could also potentially offset the growth of large clusters, which would preserve some of the high surface area and allow for faster reaction in the later stages of reaction. Previous observations made with phase contrast imaging for both CuO-Al (strong gas generator) and Fe_2O_3 thermites (weak gas generator) indicated that the CuO-Al system yielded significantly smaller material being ejected from the wire.[16] Additionally, it has been recently shown that the use of nitrocellulose as a gas generator and structural component can significantly assist thermite combustion by acting as a dispersant and reducing coalescence and sintering.[68]

For the CuO system, the use of micron scale oxidizers led to significantly slower pressure rise times, which could be the result of slower oxide decomposition, and thus O_2 release, as a result of the reduced specific surface area compared to nanoscale oxidizer. Additionally the large size and reduced surface area could simply slowdown the overall reaction rate leading to slower production of product gases (primarily Cu vapor). While the Cu_2O-Al system is not affected by oxidizer size, it produces significantly less O_2 and Cu vapor and it is not clear which is more important. In order to better understand these issues, another system that combines properties from both the Cu_2O and CuO thermites is desirable. This can be achieved by adding Cu diluent to the CuO-Al reaction. Since intermediate O_2 release is controlled by the oxidizer and its size, the nano CuO-Cu-Al system should maintain the O_2 production of nano CuO. However, the added mass of Cu will serve as a heat sink to the overall reaction, which will reduce the amount of Cu that is vaporized at equilibrium. In this way, the CuO-Cu-Al reaction ($3Cu+3CuO+2Al \rightarrow 6Cu+Al_2O_3$) approximates the global conditions of Cu_2O-Al reaction ($3Cu_2O+2Al \rightarrow 6Cu+Al_2O_3$). While both systems possess the same relative amount of each atom, the different reactants have slightly different enthalpies, so the equilibrium calculations results have minor differences. Using CHEETAH and accounting for oxide shell coating of the Al-NPs (30% of mass), at 1 atm constant pressure these CuO-Cu-Al and Cu_2O-Al systems will produce 0.54 and 0.27 moles of gas per kg of reactant respectively in contrast to the 3.7 mol/kg produced by CuO-Al.

Testing of the Al-Cu-CuO system (commercial 30 nm CuO and 60-80 nm Cu) showed that it performed almost identically to the micron CuO case (both are plotted

in Figure S8.5 in Section 8.6-Supplemental Information) with a peak pressure of 17 psi, a pressure rise time of 0.86 ms, and a burning time of 0.74 ms. That these line up so well indicates that both systems are limited by the same process. It could be related to a reduced amount of intermediate O_2, since the micron CuO will decompose at a slower rate as result of reduced surface area and the Cu-CuO mixture simply has less CuO per unit mass. It could also be a case of slower condensed phase reaction kinetics, with the Cu particles getting in the way of Al-CuO interfaces in the same way large CuO particles prevent access to the oxidizer in the center of the particle during the early stages of the reaction.

That the CuO-Cu-Al outperforms Cu_2O-Al by an order of magnitude despite sharing very similar equilibrium gas production indicates that the intermediate O_2 plays a larger role in the overall combustion process than Cu vapor. The intermediate gas, released in the early stages of reaction, likely serves as a key driver in heat transfer by providing a source of pressurization to drive hot material into the unreacted zone. This is in comparison to Cu gas, which is only produced as the last step of the reaction once the material has already reached the adiabatic flame temperature, which is the boiling point of copper vapor (2835 K). Since the O_2 will be generated much earlier in the reaction process, it can have a much larger impact on speeding up combustion propagation.

Combining all these results and discussions, a theory of the overall combustion process for copper oxide based nanocomposite thermites can be developed. From both oxides igniting at the same temperature and before O_2 release in Cu_2O, the ignition process occurs through a condensed phase reaction. Such a

mechanism has been shown to potentially occur very fast once the reactants are mobile, so this would quickly release significant energy.[79] The energy would raise the local temperature of the material and drive the decomposition of the unreacted oxidizer to produce O_2. This gas initially serves to produce a pressure gradient that drives hot material forward to the unreacted zone and propagate the reaction. Additionally, it provides a secondary oxidizer to sustain the reaction and move it towards completion. Some Cu vapor will also be produced during the reaction that will further support the heat transfer aspect.

8.5. Conclusion

The ignition and reaction properties of aluminum nanocomposite thermites with copper oxide oxidizers were studied with a variety of experiments. Cu_2O was synthesized in sizes ranging from 200 nm to 1500 nm and tested with temperature jump (T-Jump) heating of $>10^5$ K/s for oxygen release and ignition with nano Aluminum. These results were compared with CuO systems which have many similar properties but produce more intermediate (O_2) and equilibrium (Cu) gas. Cu_2O was found to release oxygen around 200 K higher than CuO, but ignite at the same temperature as the other oxidizer. This suggests that both oxides ignite through a condensed phase mechanism independent of gaseous oxygen. Cu_2O-Al reacted only very weakly in the vacuum environment and significantly more strongly in argon, which implies that secondary heterogeneous oxidation from O_2 is important for sustaining strong reaction.

Reactivity tests in a constant volume combustion cell, showed that Cu_2O-Al performed similarly independent of oxidizer size and were ~3 orders of magnitude slower than nano CuO thermites and ~1 order of magnitude slower than micron CuO thermite. CuO-Cu-Al was also tested as it has the intermediate gas release properties of CuO, with the equilibrium gases of Cu_2O-Al. The diluted system performed the same as micron CuO, which implies that O_2 production plays a significant role in both reaction and heat transfer.

Acknowledgments

Work conducted by M.R.Z and G.C.E has been supported by the Army Research Office (Ralph Anthenien) and the Defense Threat Reduction Agency. Work of the other authors was supported by the Laboratory Directed Research and Development Program at LLNL (13-ER-022, 14-SI-004). This work performed under the auspices of the US Department of Energy by Lawrence Livermore National Laboratory under Contract DE-AC52-07NA27344.

8.6. Supplemental Information

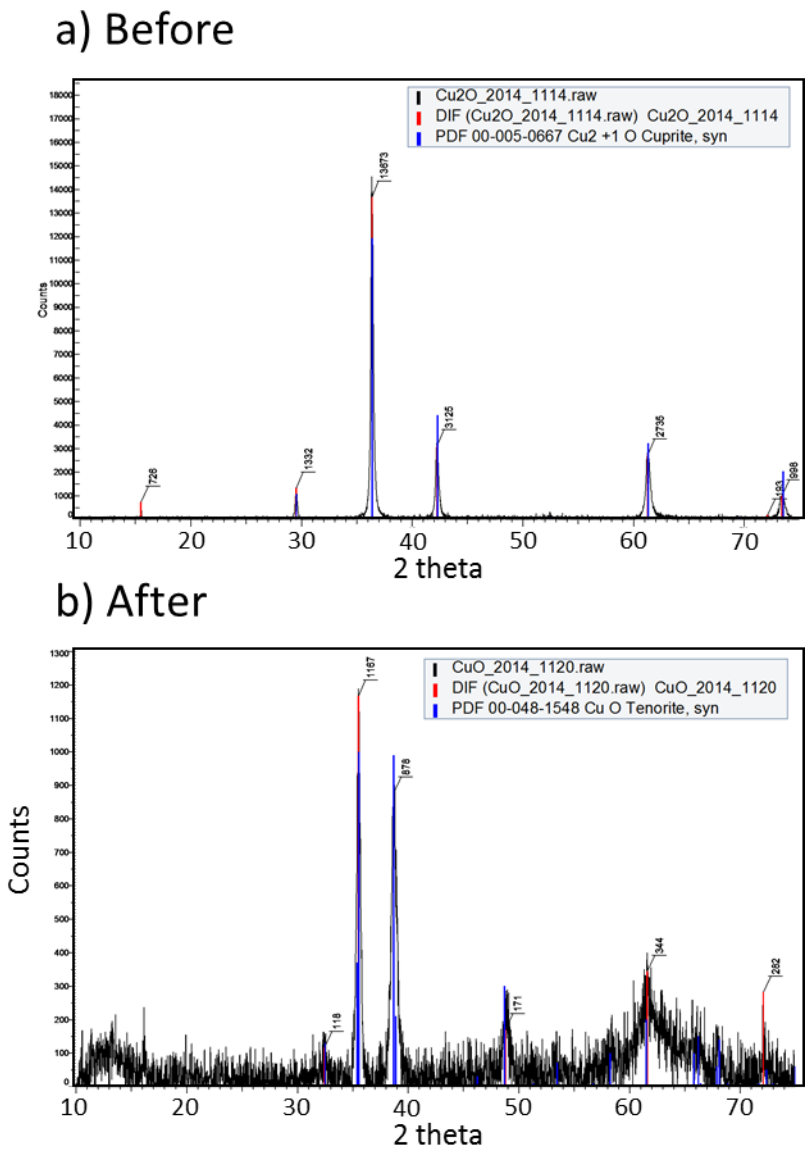

Figure S8.1. X-ray diffraction results from 350 nm Cu_2O a) before and b) after baking for 2 hr at 250°C. This shows how the material was oxidized to CuO during the process.

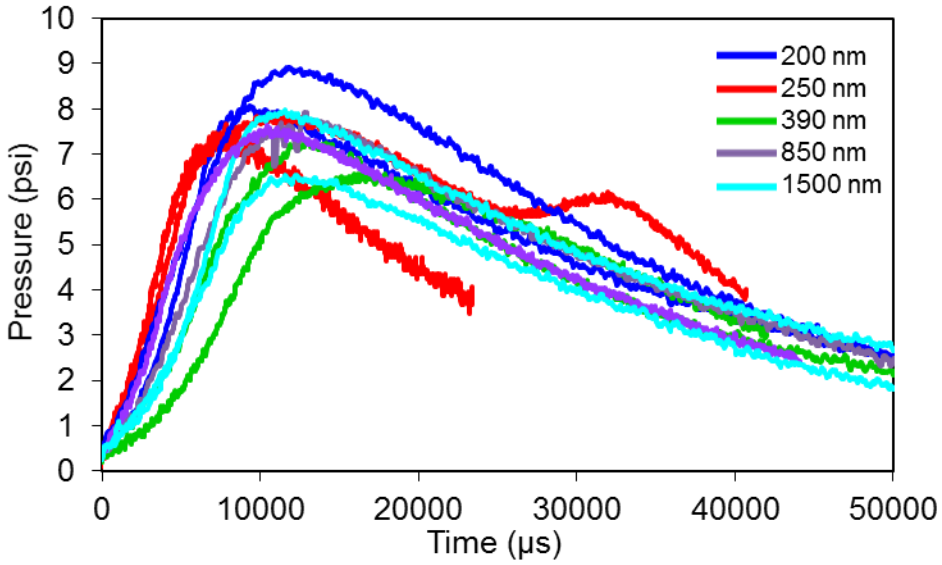

Figure S8.2. Pressure traces from the constant volume combustion cell runs of Cu_2O-Al. For all cases time zero is the point when the pressure is 5% of the max. As can be seen, there is no clear size dependence with the 390 nm oxide particles being the slowest and weakest by a small degree.

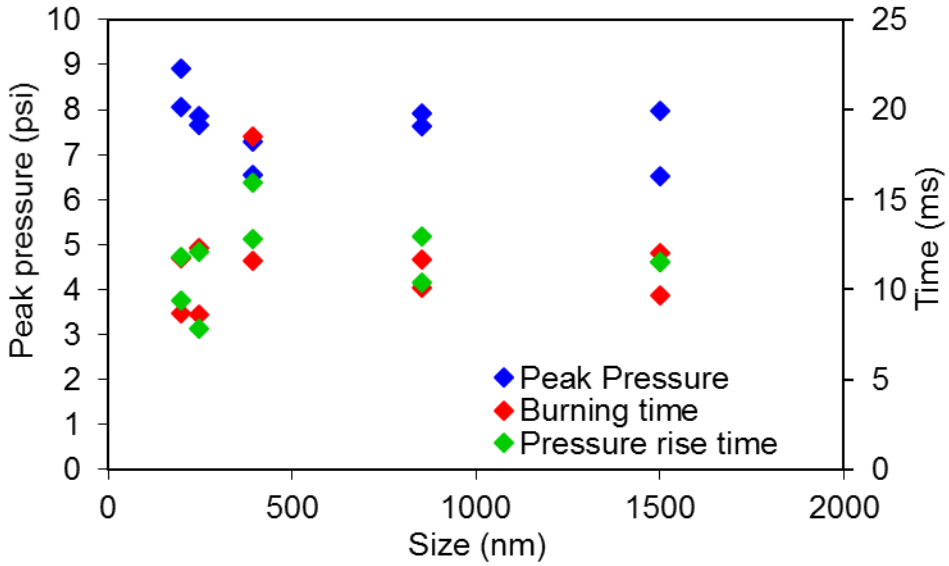

Figure S8.3. The quantified results from constant volume combustion cell runs of Cu_2O-Al. Each data point represents a different experimental run. The peak pressure (blue) corresponds to the left axis, while the burn time (full width at half maximum of optical signal) and pressure rise time (time to peak pressure) correspond to the right axis.

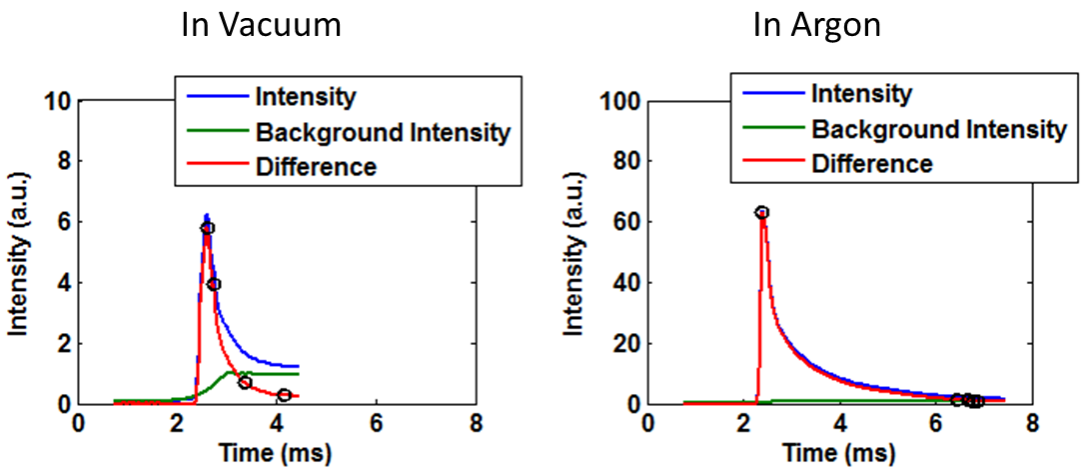

Figure S8.4. Integrated intensity from nano CuO-Al in both vacuum and argon.

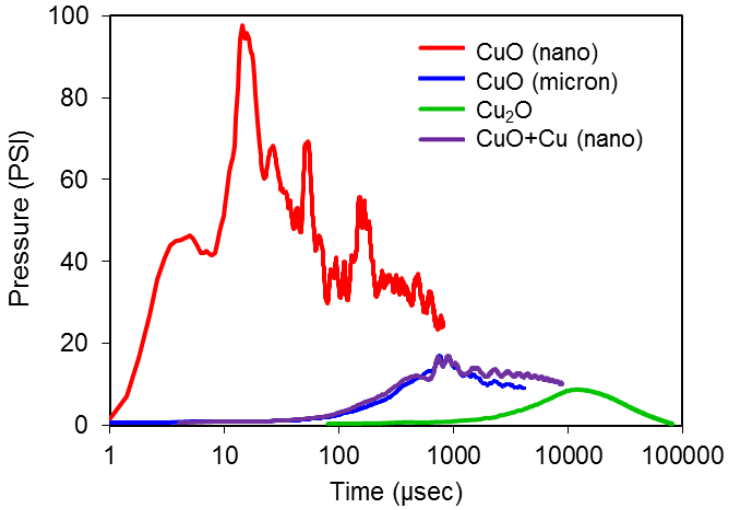

Figure S8.5. Pressure traces measured with the constant pressure cell from Al-NP with nano CuO, micron CuO, Cu_2O, and nano Cu+Cu_2O.

Chapter 9: Towards the Directed Deposition of Nanocomposite Thermite with a 3D Printing Platform for Studying the Effect of Fuel/Oxidizer Proximity on Combustion Behavior

Summary

9.1. Introduction

In Chapter 7, it was shown that the amount of interfacial area between fuel and oxidizer plays a significant role in determining the reaction characteristics for thermite nanolaminates. While the laminar structure of that system made it ideal for studying interfacial area, that property is not nearly as clear for a nanoparticle systems. Initially, the nanoparticles exist as complex aggregates (like Figure 1.3), where the number of inter-component contacts is not well defined. Then, upon heating, this nanostructure will be lost faster than reaction as discussed in Chapter 4 and 5. The process will produce dynamic interfaces that will grow and shift throughout the reaction process. Again, it is difficult to determine the amount of interfacial area because it will be changing so rapidly and the details of this process are not well understood, especially as the system evolves from the ~500 nm particles observed through DTEM to the ~5 μm particles collected from T-Jump experiments.[24]

While all these complications are eliminated in the reactive multilayer case, the dense nature of that material also removes the role of gases, which were found to be very important in the overall combustion event in Chapter 8. For these reasons, it is highly desirable to have a means of controlling the amount of interfacial contact in

nanoparticle thermites. A simple, but indirect, means of achieving this goal is to vary the quality of the mixing. In an ideal system, every fuel nanoparticle would be in contact with a neighboring oxidizer particle. In a poorly mixed case, the two materials would be highly segregated, with the only inter-component interfaces existing for particles along the borders of these zones. While this approach still does not provide an actual value for amount of interfacial area per unit mass, it does at least provides an avenue for tuning that parameter.

Previous studies have shown that mixing, and thus interfacial area, has a very significant impact on the reactivity of nanocomposite thermites.[70,71,161] Indeed, several groups have illustrated increased performance when using assembly techniques to have fuel and oxidizer combine selectively with their opposite component.[72,161,162] However, mixing of nanocomposite thermites is most often somewhat haphazard, with mixtures assumed to be well mixed or mixing being determined by performance rather than any physical parameter.[70] Even when mixing is directly assessed through elemental mapping, it is typically just for a qualitative comparison.[36,71,96] Part of the reason for this is the difficulty associated with quantifying mixing at the nanoscale.[163,164] To address some of these issues and develop a better understanding for mixing, in this chapter, I present some work with Al/Bi_2O_3 that focuses on assessing the mixing process, how it relates to interfacial area, and how it affects combustion.

Even if a complete analysis of the state of mixing can be achieved, it still remains as an inelegant and indirect means of affecting the amount of interfacial area. Therefore, it is highly desirable to develop a method that allows for more control over this process. An obvious example case to emulate with nanoparticles is the reactive multilayer system,

where the thickness of bilayers will control average diffusion distances and the amount of interfacial area. To achieve this, a platform needs to be able to deposit evenly distributed layers of fuel and oxidizers into a geometry that is ideal for testing combustion. One particularly interesting candidate technology for developing this capability is 3D printing as in recent years printing devices have become widely available and reasonably priced. In this chapter, I present two approaches to using a 3D printing platform to create lines of nanoparticle multilayers, which allow for the direct testing of combustion performance with liner burn speed measurements. The development of this process also has further implications as the directed deposition of nanoenergetics is a valuable tool for a range of applications, such as micropropulsion and MEMS devices.[14,165-168]

9.2. Experimental

9.2.1. Mixing Work

Aluminum nanoparticles were purchased form Argonide Corp., had nominal size of 50 nm and was 70% active by mass due to the oxide shell. The Bi_2O_3 was purchased from Sigma Aldrich and had a size of 90-210 nm. Fuel and oxidizer were mixed stoichiometrically accounting for the oxide shell. Mixing was done by adding hexane to the vial and ultrasonicating it for a prescribed amount of time. When no ultrasonication was used, a metal spatula was used to hand stir the suspension for 3 minutes instead. Reactivity was gauged using the constant volume combustion cell discussed in Section 2.3.

9.2.2. Printing Work

Aluminum nanoparticles were purchased form Argonide Corp., had nominal size of 50 nm and was 70% active by mass due to the oxide shell. The CuO and Bi_2O_3 were purchased from Sigma Aldrich and had a sizes of <50 nm and 90-210 nm respectively. CuO was treated with poly-4-vinylphenol (P4VP) to make it a more stable colloid following the procedures described in reference 169. Printing was done using a modified MakerBot Replicator following procedures described in the Appendix. A typical ink used in the continuous flow direct write printing was 100 mg of material in 6 ml of ethanol, 1 ml of distilled water and 0.5 ml of ethylene glycol. For electrospray printing, it was typically 100 mg in 2 ml ethanol.

9.3. Proximity Control through Mixing and the Effect on Combustion

As touched on above, quantifying the mixing of a nanocomposite is not a straightforward process. This is especially true when trying to relate the determined mixing parameter to a physical property such as interfacial area or average diffusion distance. For example, one successful approach measures the atomic ratio of fuel to oxidizer in a specific spot size at randomly selected locations throughout the material.[164] This data is used to create as histogram, which is fit to a normal distribution. The standard deviation then provides a quantified measure of mixing, since a homogenous mixture will have the same ratio wherever it is sampled. While this method is straightforward and effective, it gives no detail on the physical configuration. For that, imaging is required. Since the materials being used are nanoparticles, the characterization technique must be able to identify the different

materials with a spatial resolution on the order of ~50 nm. This restricts us to the use of electron microscopes with elemental analysis capabilities. For poorly mixed cases the segregated areas can be 10's of μm large,[71] so it is important to not limit analysis to just the smallest scale of the material, which is why SEM was chosen over TEM.

Even within the SEM, there are a wide range of magnifications that can be employed and this choice can have a significant effect on the results. Since the goal of this study is in part to study interfaces, I chose a resolution (10kx) where the individual particles are still resolvable but wider segregation was also visible. Energy dispersive X-ray spectroscopy (EDS) mapping was used as a primary tool of material identification, however this technique has a lower resolution than typical imaging since the electrons hitting a spot can excite a much larger area to produce X-rays.[170] To minimize this effect, low electron energies (10 kV) were used. Additionally, backscattered electron (BSE) images were used in conjuncture to use brightness thresholding as a secondary means of identifying materials. This works because the brightness in BSE images is proportional to the atomic number (Z) of the material. Therefore, an oxidizer like Bi_2O_3 will show up as much brighter than Al. An example of this difference is shown in Figure 9.1a,b for a standard secondary electron (SE) image and a BSE image respectively of Al/Bi_2O_3. The EDS map is shown in Figure 9.1c. Comparing the different images, the lines between components are more clearly defined for the BSE image than for the EDS map. However, in the BSE image it is not always clear whether something that appears dark is Al or just Bi_2O_3 that is lower down. Therefore, the most accurate results will be from analysis that combines both techniques.

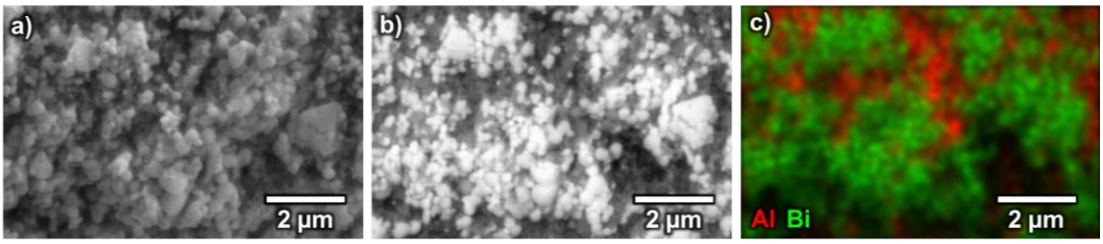

Figure 9.1. SEM images of Al/Bi_2O_3. a) was taken using secondary electrons and provides no information on material composition. b) shows the same area as imaged with BSE, which make the heavier elements (Bi in this case) appear brighter. c) shows an EDS map of the same area.

For this study, mixing was controlled by ultrasonicating the mixtures in hexane for varied amounts of time up to 20 minutes. The reactivity of these samples were tested using the constant volume combustion cell and their mixing would be characterized through SEM. BSE images and EDS maps would be taken at 5-10 locations for each mixture. Analysis would be performed on the produced images with ImageJ software. The mapping was overlaid onto the image, and Bi was identified as all pixels that were above a chosen threshold of green and brightness. These pixels were removed from the image and Al was identified in a similar manner as all those above a chosen threshold of red and brightness. Doing this creates, two binary maps for fuel and oxidizer that can be sued for further analysis. An example of this is process is shown in Figure 9.2. The sample in a) was fully mixed with the standard 20 minutes of ultrasonication. The sample in b) was only hand mixed and was not ultrasonicated at all.

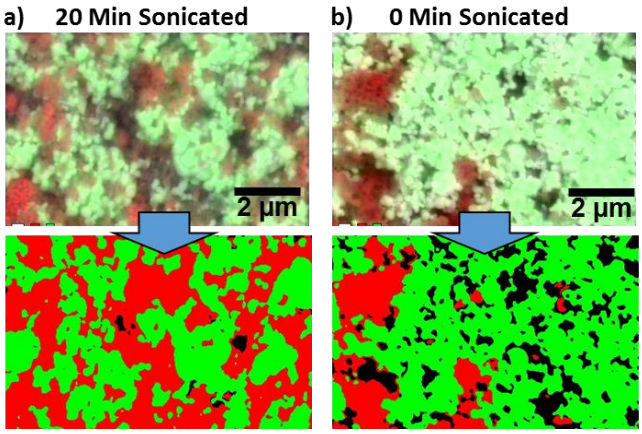

Figure 9.2. Results of the image processing analysis performed on a fully mixed example (20 minutes of ultrasonication) and a hand mixed example (0 minutes of ultra sonication) in parts a) and b) respectively. The top frames show the EDS map overlaid on the BSE image with green for Bi and red for Al. The bottom frame show the binary maps created through the process described above.

Once these maps were created, further analysis was done to assess the mixing. One helpful tool was the "distance map" function in ImageJ. This works by taking each map separately and at each pixel representing the location of material, measures the distance to the nearest pixel that is not that material. The program then represents this distance with a brightness. Thus material near the edge of a segregated area will be dark, while those in the center of such an area will be brighter. After the entire binary map is processed in this way, the histogram can be exported into data processing software (e.g., MATLAB, Excel). This data can be treated in a variety of ways. One is to consider all the materials that exist within a certain distance of the edges to be interfacial material. The number of interfacial pixels can be divided by the total number of pixels to get a percentage of material near an interface. Alternatively the average distance to the edge can be calculated for each material and then added up. This represents a rough approximation of the average diffusion distance of reaction. These two values are inversely proportional as shown in Figure

9.3 for three mixing cases of Al-Bi_2O_3. This plot also reveals the significant trouble with these measurements, that there is a very wide spread in the data.

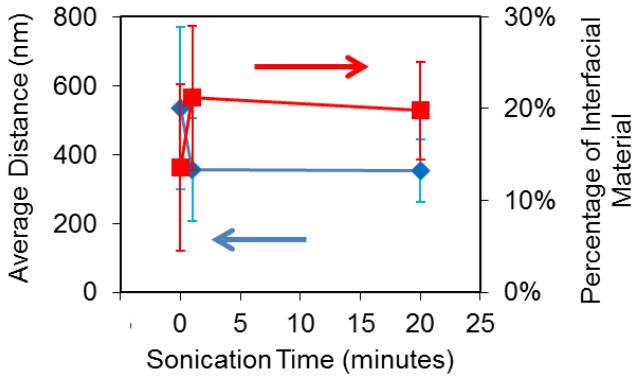

Figure 9.3. Quantified analysis of the mixing of a Al-Bi_2O_3 subjected to different amounts of ultrasonication. Interfacial area was considered as pixels within 2 pixels (~30 nm) of an edge. Both values came from running the "distance map" ImageJ function on the binary map for each material separately.

A significant issue with both of the measurements discussed above is that it is measuring to the closest pixel that is not of the same component, rather than the closest one of the opposite component. This point can be more clearly illustrated with the lower frame in Figure 9.2 where there a large number of black pixels. For this measurement made for the green pixels, it is measuring the nearest black or red pixel, and in many cases a black is clearly closer than a red. However, a more accurate representation of the diffusion distance that must be travelled will be for red to green only, ignoring the empty space of black pixels. This calculation can be done by exporting the XY data from the binary maps and analyzing it with a MATLAB code. However, except in some extreme cases (like Figure 9.2) the difference between this measurement and the one discussed above was only minimal compared to the general spread.

Along with the mixing quantification, the reactivity of these samples was assessed using the constant volume combustion cell. These results did reveal that the determined values were good predictors of performance as shown in Figure 9.4. This plot shows that the pressurization rate (peak pressure divided by pressure rise time) was greatly diminished by increasing average distance between materials.

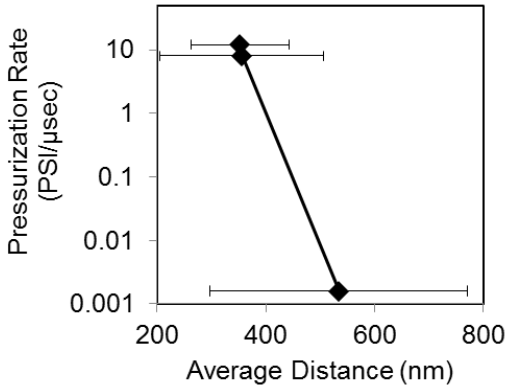

Figure 9.4. Combustion cell results for the Al-Bi_2O_3 samples subjected to different mixing, plotted against the average distance between fuel and oxidizer as shown in Figure 9.3. Note the logarithmic scale for pressurization rate.

9.3.1. Mixing Work Discussion and Conclusions

While the trend observed with Figure 9.4 indicates that this approach has potential, there are also significant issues that make it poorly suited for the stated goal of a detailed analysis of the interfacial surface area in nanocomposite thermites. For one, the quantification of mixing process is rather labor intensive. Taking a quality image and EDS map takes 10-20 minutes for each spot and the image analysis takes some human input to get the thresholding to the correct level which prevents full automation. Further, the standard deviation of this measurement is quite large, as is apparent in Figure 9.3 Figure 9.4, which limits the usability of this technique. Another very significant issue is that this approach is only effective for oxidizers with

very high atomic numbers. For example, this technique was tried on Al-CuO but the BSE and EDS contrast was too weak to allow for effective discrimination between the two materials. While identification could generally be done by eye, the simple thresholding approach was not sufficient to accurately separate fuel and oxidizer. Figure 9.3 also reveals that ultrasonication is not an effective method for controlling mixing, since even 1 minute led to mixing and performance comparable to 20 minutes.

As a final point, it is also not clear that the determined values are reasonable approximations of the actual physical values of interfacial area and diffusion distance. While SEM does differentiate topography reasonably well, the micrographs will project a certain amount of z axis down into one apparent plane. In this way it could be significantly shortening some distances. So it is not at all clear if these values could be accurately projected into a 3D space.

All of these reasons are behind the drive to create another platform for studying interfacial area in nanoparticle thermites.

9.4. Directed Deposition of Nanocomposites using 3D Printing Platform

With the growing availability of affordable and versatile 3D printers, they make an attractive choice for the basis of a nanocomposite thermite deposition system. In its simplest form, a 3D printer is an XYZ mobile nozzle that extrudes material in precisely controlled manner. Alternatively the motion relative to the nozzle, in any or all dimensions, can be provided by the stage onto which the

deposition is occurring. The structure is then built up layer by layer to create the 3D object. This is exactly the type of behavior needed to create the nanoparticle multilayers discussed above that will enable further study of the effect of interfacial area. A layer of fuel could be deposited, followed by a layer of oxide, and so on until the material is thick enough to propagate a reaction. If deposited in a straight line this will also enable a simple test of combustion behavior via burn speed.

To this end, I modified a commercially available MakerBot Replicator to enable syringe based extrusion of custom inks. The details of this modification and how to operate it can be found in the Appendix of this dissertation. In short the system works by replacing the extruder with a syringe and needle. These syringes can be filled with whatever ink formulation desired and are operated pneumatically through the printing g-code run by the program Replicator G. When printing is desired, a solenoid valve opens to allow compressed air to drive the ink. The system was also designed so that a negative pressure would be applied whenever printing was not in progress. This would cause air bubbles to flow through the ink, which would help keep it well mixed.

When designing inks for the printing of this system, the goal of an interfacial study on nanoenergetics added restraints to the formulation options. Particularly I did not want to add significant binder or surfactant which is often used to control the viscosity of the material and insure a stable solution.[171] Such materials could significantly affect the interfacial area and overall combustion. Additionally, since these materials are highly energetic, it was important to have low concentrations. While nanocomposite thermites are generally safe while in solvent, there was a

practical lower limit to how much volume of ink could be handled. Thus, if I wanted to keep the total mass of nanocomposite below a certain threshold (~100 mg), the concertation that could be achieved was limited by the minimum volume. If fuel and oxidizer are handled separately, this is no longer a safety concern, but for this study dilute inks were primarily used to allow for the production of premixed samples through the same process to serve as controls.

Two different deposition approaches were used for this study. The first was continuous flow direct ink writing, where the extrusion tip is positioned very close to the substrate and the ink is transferred directly to surface.[171] This is in comparison to droplet jetting methods such as ink-jet printing, where the droplets are generated well above the surface.[168] The continuous method chosen has the advantage of depositing more material faster than the alternative and does not require the complications associated with using an ink-jet piezoelectric for creating the droplets. Also, it is not clear that the droplet approach would be conducive to creating even layers of materials.

The primary challenge to this approach was designing an ink that could produce an even line profile after deposition. When a dilute colloid dries, it will often form a "coffee ring" pattern as particles end up depositing primarily on the outer rim of the droplet.[172,173] In a line, this same effect can lead to the buildup of the edges and leave a valley in the center. The "coffee ring" is caused by the edges of a droplet being pinned to the substrate so that as it dries that liquid on the edge is replaced from the interior of the droplet, leading to a flow of material towards the edge.[172,173] This effect can be prevented if the liquid has a high contact angle. However if a solvent

with too high of a contact angle is formed, the droplets will tend to be too mobile, which leads to beading up and uneven edges on the line. An example of these two extremes are shown in Figure 9.5 with an optical micrograph and a cross-sectional line profile. Figure 9.5a had a high contact angle, which led to the irregular edges but a plateau profile, while Figure 9.5b had a low contact angle leading to the "coffee ring" profile.

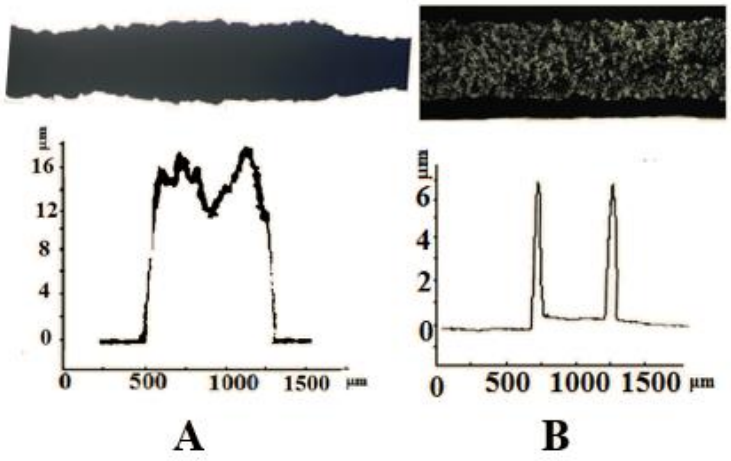

Figure 9.5. Example lines of Al-CuO nanocomposite thermite printed with two different inks and continuous flow direct ink writing. The ink for A was made from ethanol, distilled water, and ethylene glycol (EG), while the ink for B was just ethanol. Both inks had similar particle concentration ~100mg/5ml.

Based on these factors, the ink could be tuned to produce a better line by adding small percentages of higher surface energy solvents (H_2O and ethylene glycol) to the ethanol base. The surface of the substrate could also be tuned with coating to affect the contact angle and thus deposition. This surface effect also necessitated that the substrate be consistent and reliable for this style of printing. Unfortunately with all these different parameters, the sweet spot of good deposition characteristics proved to be quite small. While tuning the ink properties provided a reasonable avenue for changing the deposition characteristics, small changes would often have

large and unpredictable effects. As a result this process was hard to control and often not repeatable.

Given these difficulties, a second printing approach was also employed. This one incorporated a technique called electrospray, which is based on applying a high voltage between the needle and the substrate.[174,175] As a result of this voltage, charge builds up in the solvent, which drives it down towards the substrate. But as the droplets produced evaporate solvent, the charge gets contained in smaller and smaller volumes. This eventually leads to the breakdown of the droplets into smaller droplets which repel each other to produce an even spray of nearly monodisperse droplets. An image and schematic of this process are shown in Figure 9.6. If enough distance is given between the needle and the substrate, these droplets can be fully evaporated by the time they dry leading to an even deposition that is not dependent on any of the effects discussed for the approach discussed previously. One downside to using that is far from the substrate is that the spray can end up quite wide (~3 cm). Therefore, to get a thin line for testing burn speed, masking must be used. One downside to masking is that a significant volume of the material deposited is lost to the mask, which limits how much goes towards building up height and thus slows down the printing process.

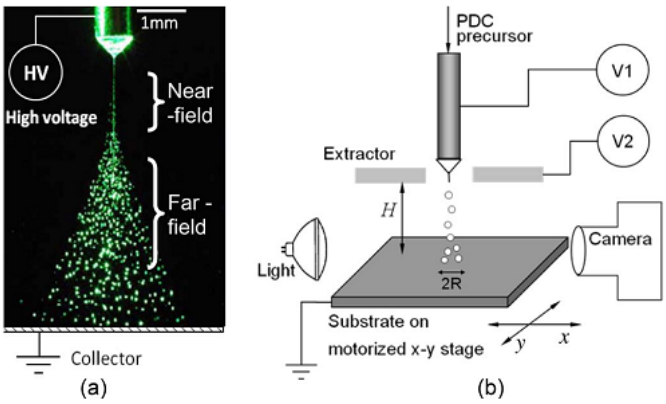

Figure 9.6. A photograph illustrating the electrospray process (a) and a schematic illustration of how it can be used to deposit material for printing (b). Figure reproduced from Duan, H., Li, C., Yang, W., Lojewski, B., An, L., & Deng, W., Near-field electrospray microprinting of polymer-derived ceramics. Journal of Microelectromechanical Systems, 22(1), 1-3. © 2013 IEEE.[174]

Full details on this printing process, including the inks used, can be found in the Appendix of this dissertation. In short a power supply was used so that a high voltage (4-5 kV) could be held between the needle and substrate, which was typically a sheet of aluminum held at ground. Note that this system did not use an extractor like is shown in Figure 9.6. The printing program moved the needle along the length of the line established by the mask while maintaining a distance of 10 mm above the substrate. The syringe turned on and off as controlled by the program but the voltage was controlled manually. When the printing is aligned with the syringe holder, both syringes can be run simultaneously, which allows for fuel/oxidizer layers with the same pass.

The lines produced using this technique did have generally better and more consistent cross-sectional profiles (compare Figure 9.7a with those of Figure 9.5). It also enabled the successful printing of multilayers, as shown in Figure 9.7b. In these ways, this approach was a success. However, there are still hurdles with consistency

and metrology that must be overcome before a detailed analytical study of interfacial area can be performed. For, repeatability it was found that the quality of the ink was dependent on the batch of oxidizer purchased from the supplier. Some would allow for stable inks that produced good lines and others would lead to clogs in the needle and poor printing. What causes these differences is not yet well known so more work is needed on this point. More concerning is that the technique (physical profilometery) used for measuring height was not always reliable. SEM imaging revealed that for less dense samples the profilometer could drag a line through the material itself and provide false values.

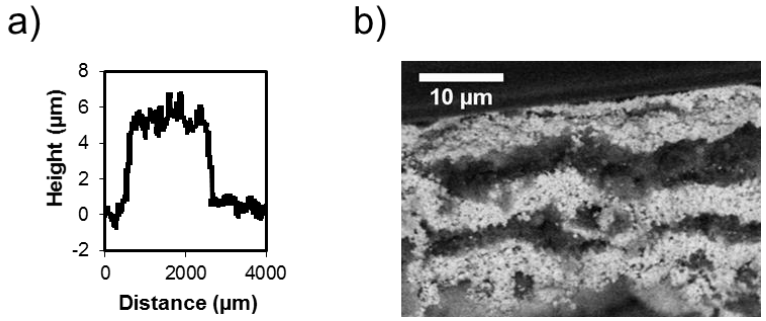

Figure 9.7. a) The cross-sectional profile of an Al-Bi_2O_3 produced through the electrospray printing process. b) The cross-sectional view of a multilayer produced by alternatingly electrospray printing Al and Bi_2O_3. The image was taken with SEM using BSE, so the brighter material is Bi_2O_3.

Outside of the printing, the linear geometry produced was indeed well suited to burn speed tests. Films as thin as 2 µm were found to propagate when ignited with a NiCr wire. The combustion events were observed with a high speed camera (Phantom v12.1) and a flame speed could be determined. For well mixed Al/Bi_2O_3, the flame was found to propagate at speeds of 2-200 m/s depending on the film thickness. However, the thickness was measured with the profilometer was not

always a good predictor of speed, but as mentioned this may have been more of a problem with the thickness measurement than the line itself.

9.4.1. Printing Work Conclusions

3D printers hold significant potential for a wide range of applications, and that is true for nanocomposite thermites as well. They are highly versatile and allows for a wide range of approaches to depositing material. For the specific goal of studying interfacial area, electrospray printing is a very good option. It allows for the even deposition of nanoparticle films without the need for binder or significant tuning of the solvent. The addition of some stabilizing agents may be beneficial to the process. An improved method for characterizing the films is also needed, perhaps a 3D lase profilometer like the one used in a previous study of electrophoretically deposited nanothermite films.[36]

Chapter 10: Summary

10.1. Conclusions

The goal of this dissertations was to provide a better understanding of the nanoscale processes that occur during nanocomposite thermite reactions and how they affect combustion. This was done primarily using high temporal resolution *in situ* experiments with heating rates that simulate free combustion. Taking all the presented results into consideration, it is possible to form a comprehensive picture of the overall reaction and propagation process.

To start, DTEM was used to directly image the nanoscale morphological change in Al-NPs that undergo rapid heating (10^{11} K/s) as presented in Chapter 4. These results indicated that loss of nanostructure can occur in as little as 10 ns and can complete in ~75 ns for a typical aggregate. This timescale is far shorter than any observed for bulk combustion, where ~10 μs pressure rise times have generally been considered the fastest event.[22,45] Therefore, one of the earliest events in the process of nanocomposite thermite combustion is the loss of nanostructure, with the complex aggregates coalescing into larger spheres. Thus the overall reaction rate may be dictated by the final size of the particle rather than the initial size. This can explain some of the diminishing improvement that has been observed by using smaller and smaller particles.[11,17,18,56,58]

While, this process is detrimental to the specific surface area and the diffusion distances, it can also lead to larger interfaces between fuel and oxidizer. Across these interfaces, reaction can occur through the condensed phase, which generates energy and promotes further mobility and the growth of larger interfaces in process referred

to as reactive sintering.[16] Such a process was directly observed through DTEM to occur on a timescale of 0.5-5 μs, as discussed in Chapter 5. For Al-CuO, the product was found to be phase separated large particles, which were consistent with T-Jump product. The timescale corresponded well with the initial pressure rise observed in a combustion cell and the oxide decomposition was consistent with TOFMS. All of these results, suggest the early stages (<10 μs) of reaction are dominated by a condensed phase interfacial reaction that simultaneously releases gas.

More insight into this reaction mechanism was provided by the T-Jump study of Al/CuO reactive multilayers discussed in Chapter 7. There, it was found that condensed phase reaction could occur across an oxide barrier layer with an activation energy of ~50 kJ/mol. This value is much lower than what would be expected from bulk values for diffusion through an Al_2O_3 layer. This lays the ground work for modelling the kinetics of the condensed phase reaction and also supports that it can occur fast enough to produce the dynamic response observed in nanoparticle thermites. The product collected from both thermite geometries were consistent, which further supports that the dominant reaction mechanism was the same for both materials.

This general mechanism for the early stages of reaction is supported by the results of the reduced oxide study in Chapter 8. However the study also revealed that secondary oxidation and general gas production are equally important for the overall reaction process. It was found that both CuO and Cu_2O thermites ignite at the same temperature, despite Cu_2O not releasing oxygen until a significantly higher temperature. So while this supports condensed phase initiation, the reaction of Al-

Cu_2O was very weak in the vacuum of the TOFMS, but violent at atmospheric pressure. This indicates that gaseous oxidizer plays an important role in maintaining reaction after condensed phase initiation. It was also determined that the strong release of intermediate gases (such as O_2 from oxidizer decomposition) is critical for the heat transfer to support a fast overall combustion event. As illustrated by the straightforward calculations in Chapter 3, this gas is needed to propel hot material forward into the unreacted zones and thereby propagate the reaction

Taking all these pieces together creates a general outline of nanocomposite thermite combustion that is illustrated schematically in Figure 10.1. First, heating leads to initiation of reaction through the condensed phase. Then, the heat quickly leads to a significant loss in the initial nanostructure in less than 100 ns. Starting with this process, intermediate gases are produced, which continue to build up as the condensed phase reaction continues. A significant portion of this process occurs within ~10 µs. The gases produced then play two roles. They create large pressure gradients that propel the hot material forward into the unreacted zone, which propagates combustion. Also, oxidizing gases continue to react with the material for a much longer time (several milliseconds).

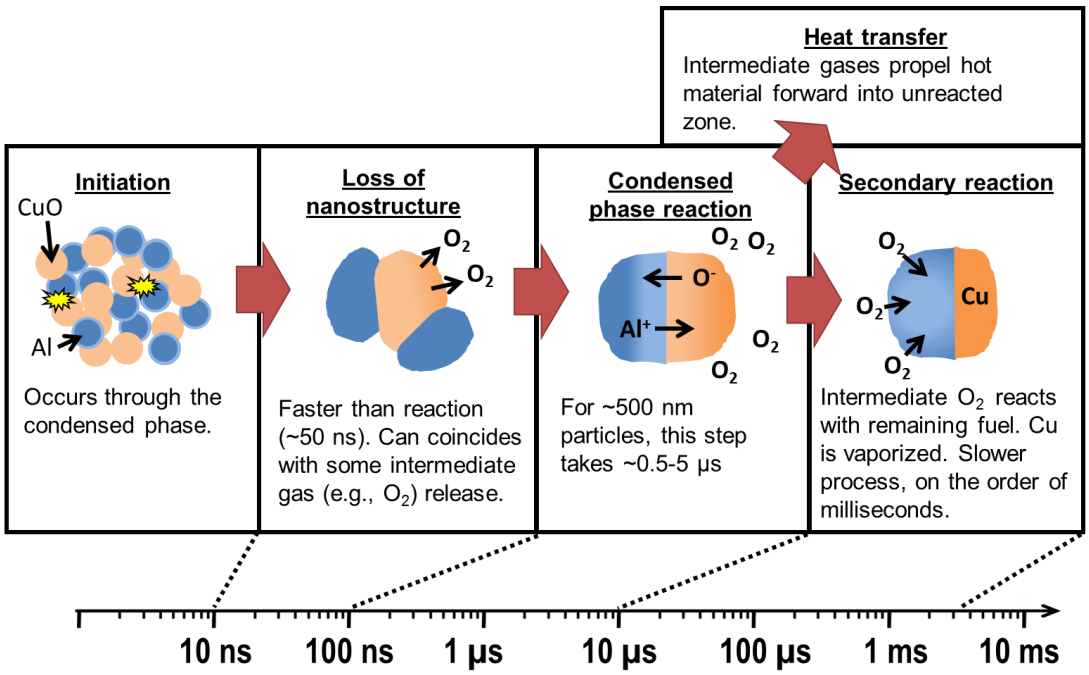

Figure 10.1. A schematic illustration of the overall combustion process of a nanocomposite thermite. This uses Al/CuO as an example since it was the most studied, but the process should be generally consistent over a wide range of systems.

The hard lines drawn between these different processes here was done for illustrative purposes to represent the rough timescale of the different mechanisms. In an actual combustion event, all these different processes will be occurring throughout the material simultaneously, but this illustration gives an idea of what is likely to be controlling the kinetics at any given point. The details will also be different depending on the materials properties of the fuel and oxidizer, but there was enough consistency among the different materials tested to indicate that the overall picture will be similar to what is shown.

10.2. Recommendations for Future Work

10.2.1. DTEM at Different Heating Rates

Two of the biggest challenges when interpreting DTEM results were both caused by the laser heating. First, absorption was highly dependent on nanoscale morphology in such a way that the temperature reached by a given aggregate cannot be reasonably estimated with modelling. Second, the heating rate (10^{11} K/s) is significantly faster than any of the other techniques used in this study (10^{5}-10^{6} K/s) and faster even than the upper bound estimates for free combustion (10^{8}-10^{9} K/s).[22] For these reasons it would be highly useful to have an alternate heating mechanism that could provide an accurate temperature and a rate more comparable to other studies. Exactly this capability has been recently developed through the integration of a nanocalorimeter (10^{5} K/s) into the DTEM.[176,177] However, one of the challenges of such an approach is that the DTEM is designed to operate over a time frame of several μs, while the heating will take several ms. To overcome this, the system integrated a fast cathode laser shutter. The laser pulses were set to occur every 100 ms with the calorimeter and shutter initiated a timed delay from one of those pulses. Thus only one image will be taken for experiment, at a defined time from the start of the heating. While being limited to a single shot per experiment is a significant limitation because of the wide variability in shape and size of nanoparticle aggregates, it can still provide a valuable comparison to the laser heating experiments.

Besides the accurate temperature and more moderate heating rate, the nanocalorimeter has the additional advantage of providing significantly more information on the behavior of the material. The calorimetry data will provide

information on the heat generation of the sample. Also the same system has been recently coupled with my group's TOFMS to provide speciation as well.[178] Therefore, through a series of experiments, in this lab and LLNL, the morphological changes observed with DTEM could be directly related to energy release and gas generation.

10.2.2. Alternative Fuels for Nanolaminates

As discussed in Chapter 7, the effective diffusivity controlling reaction in Al-CuO nanolaminates was found to be significantly lower than bulk values from Al_2O_3. This raises some interesting questions about what process is responsible for this effect. Could it be a physical breakdown of the barrier layer? Does the high heating rate somehow effect the process? One way to address these questions is to use an experimental approach similar to the one used by my collaborator at NCSU, Dr. Edward Mily, in a slow heating rate study of reactive multilayers.[61] In that, study the authors tested Al, Mg, and Zr with CuO multilayers of varying bilayer thickness with DSC and X-ray diffraction (XRD) of annealed sample. They found that the bulk diffusivity was a very good predictor of the temperature of heat release as shown in Figure 10.2. As oxygen has a higher diffusivity in both MgO and ZrO_2 compared with Al_2O_3, if barrier layer diffusion is still the limiting step at high heating rates, T-Jump experiments with these materials should ignite at lower temperatures and with lower activation energy than for Al-CuO. If that is not the case, then the controlling behavior may be more complex and may involve mechanical breakdown of the barrier.

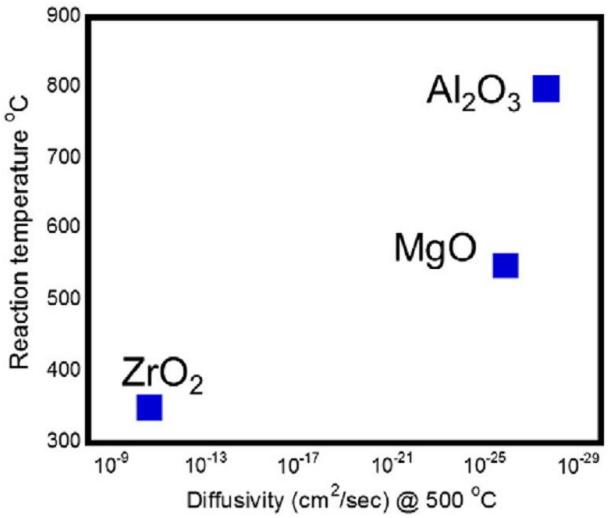

Figure 10.2. The temperature at which reaction was first observed for a reactive multilayer in DSC plotted against the diffusivity of oxygen in the metal's oxide layer. Reprinted from Thin Solid Films, 562, Mily, E. J., Oni, A., LeBeau, J. M., Liu, Y., Brown-Shaklee, H. J., Ihlefeld, J. F., & Maria, J. P., The role of terminal oxide structure and properties in nanothermite reactions, 405-410 (2014), with permission from Elsevier[61]

Initial work with T-Jump studies of Zr-CuO and Mg-CuO has been done. However, changes to the deposition chamber prevented further deposition onto the wires. Upgrades to enable this process once again are in progress, but will not be completed in time to allow for this study to be a part of this dissertation. What has been found so far is that the Mg-CuO does indeed ignite at a lower temperature than Al-CuO over a range of different bilayer thicknesses. However, there was inconsistencies with the reactivity of the prepared samples, which will require this work to be repeated. Zr-CuO was not found to ignite at all despite the fact that many samples at many different bilayer thicknesses were tested. However, mild exothermic behavior occurring at very low temperature was observed through comparing the wire temperature during the initial sample run to the temperature during the background run. This could suggest that reaction in these sample occurs early, which grows the

barrier layer and makes it too thick to enable ignition. Instead. an even higher heating rate may be need to achieve ignition, such as the heating provided by shock experiments.[87] More tests are needed to rule out sample preparation factors and to further investigate this possibility.

Testing other fuels will also help determine the role of molten fuels in reaction. It is also possible that the Zr samples were not reactive because it melts at a high temperature 2128 K. The lack of a highly mobile fuel could prevent violent reaction. For this reason Ta is another interesting choice, as it has been seen to react violently despite its high melting point as discussed in Chapter 6.

10.2.3. Alternate Reduced Oxide Oxidizers

The study discussed in Chapter 8 illustrated that the weakened gas release in Cu_2O severely limited its reactivity but did not affect ignition. It would be very interesting to see if this holds true for other oxides with stable reduced oxides as well. Of particular interest are ones with different oxygen release behavior compared with CuO. Looking back at Figure 1.8, it can be seen that Co_3O_4 releases oxygen far before it ignites and SnO_2 ignites without any oxygen release. Both these oxidizers also have stable reduced phases (CoO and SnO). Unfortunately, there are not a wide array of commercially available reduced oxide nanoparticles. For example, CoO nanoparticles purchased from US Research Nanomaterials, Inc. were found to contain a significant portion of Co_3O_4 through XRD analysis. The best example that could be found was Fe_3O_4 purchased from Sigma Aldrich. T-Jump tests with this material showed that it was consistent with the copper oxide case, releasing oxygen at higher temperatures than Fe_2O_3 but igniting at the same. However combustion cell tests showed that it

behaved very similarly to the fully oxidized case. This may be because Fe_2O_3 is already a poor gas producer, so further reducing its production only has a minimal effect.[101] More work is needed to investigate this issue.

As for the other oxides, it may be possible to reduce the commercially available nanomaterials to produce the desired material. Perry *et al*. showed that this was possible by using H_2 to reduce WO_3 to WO_2.[179] A similar procedure could be used on Co_3O_4 and SnO_2.

Appendix: Tutorial on Printing Nanocomposite Thermites

Part A: The Printer

As mentioned in Chapter 9, the system (pictured in Figure A.1a) used in this dissertation is based off of a MakerBot Replicator 3D printer. The primary modification was removing the extruders from the mobile carriage that supports it and enables XY motion. This can be done easily by removing a few small bolts. I replaced the extruder system with a syringe holder designed to fit the carriage and take its place. The holder can take two 5 ml standard syringes and was built using the 3D printer itself prior to dismantling it. This is shown attached to the carriage, with a syringe in place in Figure A.1b.

a) b)

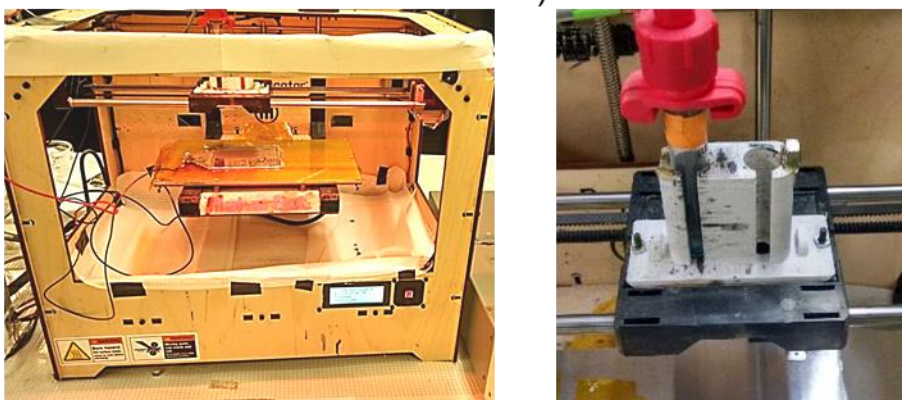

Figure A.1. An image of the modified 3D printer (a) and a close up of the syringe holder in place in the mobile carriage with a syringe in place (b).

The red piece on the top of the syringe is a syringe adaptor that allows for compressed air to control the syringe. The adaptor is connected to a 3-way solenoid valve. The input pressure port of the valve is connected to a compressed air line that runs through a regulator, then a pressure gauge, then a high precision pressure

regulator, then a digital pressure gauge where it splits to the input ports of the two solenoid valves that each control a syringe (designated 0 and 1). The setup used to control all this is shown in Figure A.2. The high pressure regulator functions best when its input pressure (controlled by regulator 1) is ~5-10 psi higher than the output pressure. The exhaust ports of each solenoid valve are connected to a 12 V vacuum pump, which is controlled through a variable voltage and current power supply. Thus whenever the solenoid is off, the syringe will feel the negative pressure of the vacuum pump, which will cause it to pull in air from the needle tip. This will cause bubbles to go through the ink which can help support a stable suspension. When the solenoid is turned on, the syringe feels the high pressure and begins to push out ink.

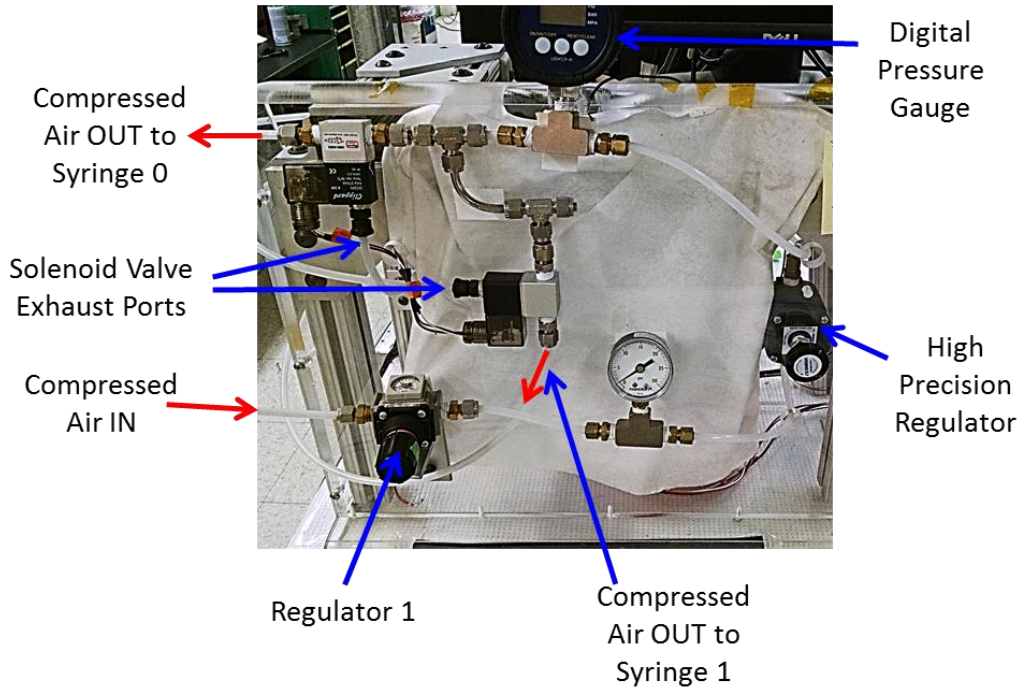

Figure A.2. The pressure control system used to operate the syringes in the 3D printer.

The scheme for controlling the solenoids involved the other significant modification to the printer. In regular operation, the extruders are heated up to high

temperature in order to melt the plastic. As this function is not needed for syringe printing, these signals were coopted for the purpose of operating the solenoids. The heating outputs are well labeled on the circuit board and provide 24 V which can be directly connected to the solenoid valve. Note that when solenoids turn off they can create inductive “kick back” which could send current the wrong way into the circuit board and cause problems. Therefore it is good to use a solenoid valve with an built in diode to prevent this from occurring. I used the item number 6124K536 available from McMaster-Carr, which has an LED.

Part B: Controlling the Printer

Operation of the printer is handled through an open source program known as Replicator G (http://replicat.org/). The printer connects to the computer running the program through USB. Before opening the program it is good to have the printer already be on (switch is in the back). A screenshot of Replicator G is shown in Figure A.3. The first step is to connect with the printer, which is done with the button indicated in the figure and will also happen automatically if the printer is on when the program loads. Prewritten scripts can be opened using the file tab and when you are ready to run them, hit the run code button indicated (note that it is greyed out in figure because the program is not connected). The Control panel can be used to manually control the XYX position.

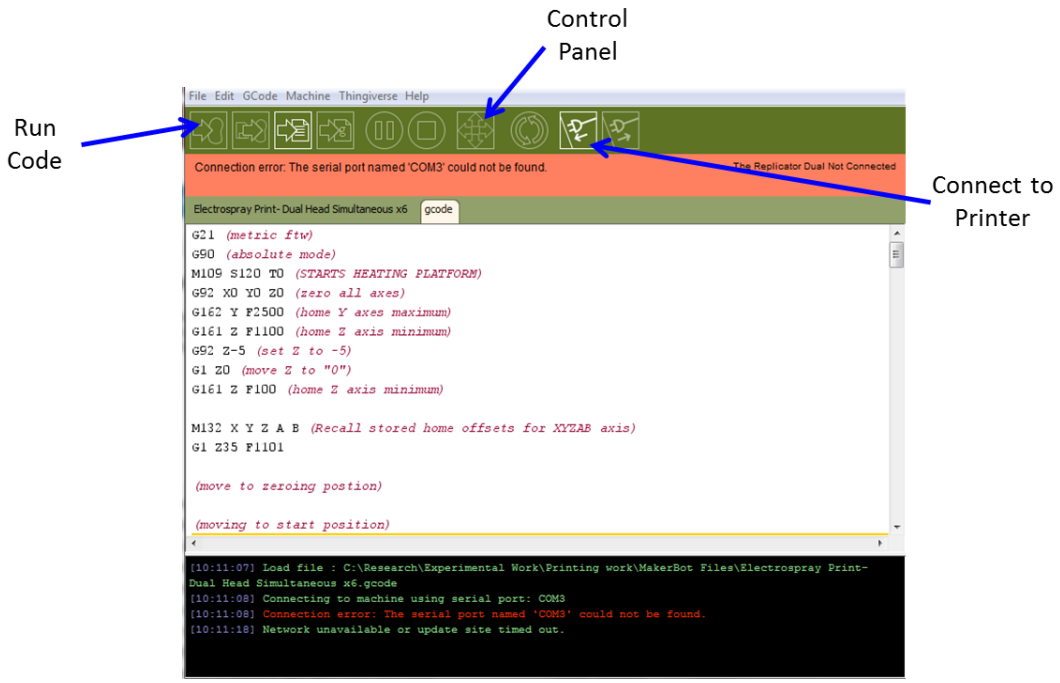

Figure A.3. A screenshot of Replicator G with the buttons for connecting to the printer, the control panel, and running the code indicated.

Replicator G works by turning commands written using gcode into commands for the printer. Gcode is a pretty straightforward system where a certain function is given a code (e.g., G1 is for motion) which is then followed by a series of numbers that tell the system what to do with that function. Some gcodes are universal to all systems, but many are also tuned for the specific device. The Replicator G website has a good primer on gcodes but be wary that they are not 100% applicable to this printer. At the start of every script, there are several gcodes which confirm the settings of machine and get everything in place to start printing. Thus they should be included in every script to be run. This sequence is:

G21 (metric)
G90 (absolute mode)
M109 S120 T0 (starts heating platform)
G92 X0 Y0 Z0 (zero all axes)
G162 Y F2500 (home Y axes maximum)
G161 Z F1100 (home Z axis minimum)

G92 Z-5 (set Z to -5)
G1 Z0 (move Z to "0")
G161 Z F100 (home Z axis minimum)
M132 X Y Z A B (Recall stored home offsets for XYZAB axis)

Any text in parentheses is not read by the computer so it works as a comment describing the code. The first two lines make all the units metric (mm) and turn it to absolute coordinate mode. This means that commands will move the printer carriage to a set location rather than move it by that amount. M109 directs the substrate heating, the number after S is the desired temperature in degrees Celsius (120 is the highest), and T signifies which platform (there is only one so this should always be 0). G92 sets the given axis (XYZ) to the given value (0 in this case). The next two lines home the Z and Y axis, which means that the carriage moves until it hits the stop switch that tells it that it has reached the end of the track. Note, that the X axis does not home, since after removing the extruder there is nothing on the carriage that will touch the switch. Therefore, **always start a print with the carriage as far right as possible.** If not, the computer will think it is in a different X position than it actually is. This can lead to collisions with the frame and stress on the motors. The next 3 lines are for more accurately homing the Z axis. The number after F always indicates the speed of motion (in mm/min) so by moving the stage close at higher speed, it can be repeated more accurately at low speed. The final code sets all the values to those stored in the computer, since it now knows the physical position of the carriage and stage. In these coordinates (0,0,0) is towards the center of the stage, with it in its highest position.

Other than those standard codes which can be copied into every script there are really only 3 others that need to be known:

G1 X__ Y__ Z__ F__ - This tells the system to go to the specified coordinates at the set speed. So G1 X-55 Y10 Z10 F2000 will have the carriage move to 55 mm to the left of center, 10 mm away from center toward the back of the printer, and set the stage 10 mm below its max all at 2000 mm/min. Note that this speed is pretty good for fast course motion. Also if a dimension is not mentioned it will not be changed.

G4 P____ - This is the pause function. The number after the P determines how many milliseconds the systems pauses for.

M104 S__ T__ - This command controls the extruder temperature normally, but controls the solenoid valve for us. The number after S is the desired temperature (max 220) and the number after T is which syringe (0 or 1). By setting the temperature high (220), the solenoid turns on. Setting the temperature low (0) turns it off.

Those are all the pieces needed to build printing script. One other one is M18 which turns all the drives off, so I usually insert it at the end of a script. In terms of piecing together code, there are a few best practices to keep in mind to help avoid bugs:

- Make sure the stage heating is off before using the solenoid valves. If the circuit is providing a voltage to both, the signal can get mixed up. So always use M109 S0 T0 directly before turning the solenoid valves on. You can always turn the stage back on to keep it hot once that segment of printing is done.
- Always add pauses after important commands. Without that the compiler may combine two lines that you want separate. For example if you want to turn the syringe off after moving it, I've noticed it sometimes turn off at the start of the movement instead if you do not have a short pause (e.g., G4 P10 = 10 ms).
- Always end the code with G1 X152 F___. That is the position all the way to the right, which is where you always want the carriage to start for the reasons discussed above. This prevents you from having to do it manually.

Part C: Example Printing Procedure

Here I present a generic procedure for printing a single layer using the continuous flow direct writing approach.

1. **Preheat the printer-** you want the printer stage hot to help with evaporation of solvent, but it takes ~10-15 min to reach 120 ^{o}C (the max temperature). Preheating can be done using the screen on the front of the bot itself. From the main menu, select "preheat", and then turn it on. Make sure that the extruder preheating is off. Preheat settings can be reached form the main menu by selecting the info and settings option and then preheating settings.
2. **Make ink-** usual inks are ~100 mg of material in ~5 ml Ethanol, with some other solvents like H_2O and EG sometimes added. Weigh out your material into a vial, then use the 1 ml syringes to measure out the appropriate amount of each solvent. Then ultrasonicate for ~5 minutes if it is single component, ~20 minutes for a mixture.
3. **Activate pressure system-** Turn on regulator 1 up to a pressure of ~15 psi. Then turn the high precision regulator to the desired pressure using the digital pressure gauge to monitor. Generally a pressure of ~0.1-1 psi is wanted. If bubbling is desired, turn on the power supply for the vacuum pump
4. **Fill syringe with ink-** The easiest way to do this is attach your needle to the syringe (typically 30 gauge) and dump the ink in through the top.
5. **Load syringe into holder-** attach the adapter to the syringe and insert it into the holder. DO NOT PUSH IT ALL THE WAY IN
6. **Run Code**

```
G21                 (metric)
G90                 (absolute mode)
M109 S120 T0        (starts heating platform)
G92 X0 Y0 Z0        (zero all axes)
G162 Y F2500        (home Y axes maximum)
G161 Z F1100        (home Z axis minimum)
G92 Z-5             (set Z to -5)
G1 Z0               (move Z to "0")
G161 Z F100         (home Z axis minimum)

M132 X Y Z A B      (Recall stored home offsets for XYZAB axis)
G1 Z35 F1101        (moves stage down)

(move to zeroing position)
G1 X-10 Y20 F2000
G4 P10
G1 Z0 F200          (raises stage to max)
G4 P6000        (NOTE!! ZERO NEEDLE TIP HERE – see detail in text).
G1 Z35 F200

(moving to start position)
G1 X-50 Y10 F2000
G4 P10
```

```
G1 Z0.5 F200          (height for printing)

(Printing   1)
M109 S0 T0            (stops platform heating)
G4 P100
M104 S220 T0          (Left Nozzle On)
G4 P1000
G1 X-15   F1000       (Printing speed)
G4 P10
M104 S0 T0            (Left Nozzle Off)
G4 P10
M109 S120 T0          (starts heating platform again)
G1 Z75 F500
G4 P10

 (return to start position)
G1 Z75 F1100
G4 P10
G1 X152 F2000         (returns to starting X position)
M109 S120 T0          (starts heating platform again)

M18 (drives off)
```

7. **Zero needle tip-** during the phase of the code after the label "moving to zeroing position," the stage will move up to you maximum and should be centered on the substrate you are printing onto (change the XY so this is true as needed). At this point during the long pause, push the syringe down into its holder so that the needle tip is just touching the substrate. This is the z=0 position of the code and must be done every time a syringe is loaded.

The preceding code simply moves the needle over the substrate to allow for zeroing and then prints a single line along the X dimension. Part of the trick to printing will be making sure all the XY coordinates in the code correspond to the desired positions on the substrate.

Part D: Electrospray Printing

As discussed in Chapter 9, electrospray printing offers many advantages. To operate in this mode, you need a high voltage power supply. Direct the positive high

voltage to an alligator clip, which gets attached to the needle of the syringe. Direct the ground to a conductive substrate. For this purpose, I generally used aluminum sheet (0.016” thick 6061 alloy). Since this method sprays rather than being finely directed, masking is needed. For this purpose I generally used painters tape and a pen knife to create a line 2 mm wide as shown in Figure A.4. The syringe will be directed along the length of the open line. In regards to the procedure above in Part C, the only major changes needed are the height and speed of printing. The needle should still be zeroed (MAKE SURE THE VOLTAGE IS OFF FOR THIS TO PREVENT ARCING) and then the height should be set for 10 mm above the substrate for a voltage of ~4 kV. Generally electrospray deposits slower, so you will also want to move slower than listed above. Also, a higher concentration ink was found to be successful and I most commonly used 100 mg per 4 ml Ethanol.

The high voltage power supply must be handled manual. Only turn it on when printing is occurring. That is only when the solenoids are engaged and ink is flowing. Turn the voltage off as soon as it reaches the end of the line and the solenoid turns off. High voltage is dangerous. NEVER reach into the printer when the voltage is on. ALWAYS double check that it is off before handling the syringe.

Figure A.4. The type of mask and substrate typically used for electrospray printing. Note that this piece has a smaller Al piece taped inside to allow for easy cross-sectioning of the line.

Bibliography

1 J. Akhavan and Royal Society of Chemistry (Great Britain), *The chemistry of explosives*, 2nd ed. (Royal Society of Chemistry, Cambridge, UK, 2004).

2 A. E. Gash, R. L. Simpson, Y. Babushkin, A. I. Lyamkin, F. Tepper, Y. Biryukov, A. Vorozhtsov, and V. Zarko, in *Energetic materials : particle processing and characterization*, edited by U. Teipel (Wiley-VCH, Weinheim ; [Cambridge], 2005), p. xxii.

3 E. L. Dreizin, Progress in Energy and Combustion Science **35,** 141 (2009).

4 L. L. Wang, Z. A. Munir, and Y. M. Maximov, Journal of Materials Science **28,** 3693 (1993).

5 R. A. Yetter and F. L. Dryer, Microgravity Combustion: Fire in Free Fall**,** 419 (2001).

6 C. E. Aumann, G. L. Skofronick, and J. A. Martin, Journal of Vacuum Science & Technology B **13,** 1178 (1995).

7 B. W. Asay, S. E. Son, J. R. Busse, and D. M. Oschwald, Propellants Explosives Pyrotechnics **29,** 216 (2004).

8 J. J. Granier and M. L. Pantoya, Combustion and Flame **138,** 373 (2004).

9 S. F. Son, J. R. Busse, B. W. Asay, P. D. Peterson, J. T. Mang, B. Bockmon, and M. Pantoya, *Propagation studies of metastable intermolecular composites (MIC)* (2002).

10 V. E. Sanders, B. W. Asay, T. J. Foley, B. C. Tappan, A. N. Pacheco, and S. F. Son, Journal of Propulsion and Power **23,** 707 (2007).

11 K. T. Sullivan, J. D. Kuntz, and A. E. Gash, Propellants Explosives Pyrotechnics **39,** 407 (2014).

12 M. R. Weismiller, J. Y. Malchi, J. G. Lee, R. A. Yetter, and T. J. Foley, Proceedings of the Combustion Institute **33,** 1989 (2011).

13 M. L. Pantoya and J. J. Granier, Propellants Explosives Pyrotechnics **30,** 53 (2005).

14 C. Rossi and D. Esteve, Sensors and Actuators a-Physical **120,** 297 (2005).

15 K. J. Blobaum, M. E. Reiss, J. M. P. Lawrence, and T. P. Weihs, Journal of Applied Physics **94,** 2915 (2003).

16 K. T. Sullivan, N. W. Piekiel, C. Wu, S. Chowdhury, S. T. Kelly, T. C. Hufnagel, K. Fezzaa, and M. R. Zachariah, Combustion and Flame **159,** 2 (2012).

17 P. Chakraborty and M. R. Zachariah, Combustion and Flame **161,** 1408 (2014).

18 Y. Zong, R. J. Jacob, S. Li, and M. R. Zachariah, Journal of Physical Chemistry A **119,** 6171 (2015).

19 M. A. Trunov, M. Schoenitz, and E. L. Dreizin, Combustion Theory and Modelling **10,** 603 (2006).

20 V. I. Levitas, M. L. Pantoya, and B. Dikici, Applied Physics Letters **92** (2008).

21 M. L. Pantoya and J. J. Granier, Journal of Thermal Analysis and Calorimetry **85,** 37 (2006).

22 V. I. Levitas, Combustion and Flame **156,** 543 (2009).

[23] S. Chowdhury, K. Sullivan, N. Piekiel, L. Zhou, and M. R. Zachariah, Journal of Physical Chemistry C **114,** 9191 (2010).
[24] R. J. Jacob, G. Q. Jian, P. M. Guerieri, and M. R. Zachariah, Combustion and Flame **162,** 258 (2015).
[25] V. I. Levitas, M. L. Pantoya, and S. Dean, Combustion and Flame **161,** 1668 (2014).
[26] B. S. Bockmon, M. L. Pantoya, S. F. Son, B. W. Asay, and J. T. Mang, Journal of Applied Physics **98** (2005).
[27] M. R. Weismiller, J. Y. Malchi, R. A. Yetter, and T. J. Foley, Proceedings of the Combustion Institute **32,** 1895 (2009).
[28] B. D. Shaw, M. L. Pantoya, and B. Dikici, Combustion Theory and Modelling **17,** 25 (2013).
[29] J. M. Densmore, K. T. Sullivan, A. E. Gash, and J. D. Kuntz, Propellants Explosives Pyrotechnics **39,** 416 (2014).
[30] K. T. Sullivan, O. Cervantes, J. M. Densmore, J. D. Kuntz, A. E. Gash, and J. D. Molitoris, Propellants Explosives Pyrotechnics **40,** 394 (2015).
[31] V. I. Levitas, B. W. Asay, S. F. Son, and M. Pantoya, Applied Physics Letters **89** (2006).
[32] S. W. Dean, M. L. Pantoya, A. E. Gash, S. C. Stacy, and L. J. Hope-Weeks, Journal of Heat Transfer-Transactions of the Asme **132** (2010).
[33] R. Prasher, Physical Review B **74** (2006).
[34] X. J. Hu, R. Prasher, and K. Lofgreen, Applied Physics Letters **91** (2007).
[35] S. F. Son, B. W. Asay, T. J. Foley, R. A. Yetter, M. H. Wu, and G. A. Risha, Journal of Propulsion and Power **23,** 715 (2007).
[36] K. T. Sullivan, J. D. Kuntz, and A. E. Gash, Journal of Applied Physics **112** (2012).
[37] D. A. Firmansyah, K. Sullivan, K. S. Lee, Y. H. Kim, R. Zahaf, M. R. Zachariah, and D. Lee, Journal of Physical Chemistry C **116,** 404 (2012).
[38] G. Jian, S. Chowdhury, K. Sullivan, and M. R. Zachariah, Combustion and Flame **160,** 432 (2013).
[39] K. Park, D. Lee, A. Rai, D. Mukherjee, and M. R. Zachariah, Journal of Physical Chemistry B **109,** 7290 (2005).
[40] A. Ermoline and E. L. Dreizin, Chemical Physics Letters **505,** 47 (2011).
[41] P. Lynch, G. Fiore, H. Krier, and N. Glumac, Combustion Science and Technology **182,** 842 (2010).
[42] A. Rai, K. Park, L. Zhou, and M. R. Zachariah, Combustion Theory and Modelling **10,** 843 (2006).
[43] W. D. Kingery, H. K. Bowen, and D. R. Uhlmann, *Introduction to Ceramics* (Wiley, 1976).
[44] T. Bazyn, H. Krier, and N. Glumac, Combustion and Flame **145,** 703 (2006).
[45] K. Sullivan and M. R. Zachariah, Journal of Propulsion and Power **26,** 467 (2010).
[46] B. J. Henz, T. Hawa, and M. R. Zachariah, Journal of Applied Physics **107** (2010).
[47] D. Stamatis, A. Ermoline, and E. L. Dreizin, Combustion Theory and Modelling **16,** 1011 (2012).

[48] V. I. Levitas, Philosophical Transactions of the Royal Society a-Mathematical Physical and Engineering Sciences **371** (2013).
[49] Y. Li, R. K. Kalia, A. Nakano, and P. Vashishta, Journal of Applied Physics **114** (2013).
[50] W. Q. Wang, R. Clark, A. Nakano, R. K. Kalia, and P. Vashishta, Applied Physics Letters **95** (2009).
[51] A. Shekhar, W. Q. Wang, R. Clark, R. K. Kalia, A. Nakano, and P. Vashishta, Applied Physics Letters **102** (2013).
[52] G. Jian, N. W. Piekiel, and M. R. Zachariah, Journal of Physical Chemistry C **116,** 26881 (2012).
[53] Y. Ohkura, P. M. Rao, and X. L. Zheng, Combustion and Flame **158,** 2544 (2011).
[54] G. C. Egan, K. T. Sullivan, T. LaGrange, B. W. Reed, and M. R. Zachariah, Journal of Applied Physics **115** (2014).
[55] L. Zhou, N. Piekiel, S. Chowdhury, and M. R. Zachariah, Journal of Physical Chemistry C **114,** 14269 (2010).
[56] P. Lynch, H. Krier, and N. Glumac, Proceedings of the Combustion Institute **32,** 1887 (2009).
[57] T. Bazyn, H. Krier, and N. Glumac, Proceedings of the Combustion Institute **31** (2007).
[58] Y. Huang, G. A. Risha, V. Yang, and R. A. Yetter, Proceedings of the Combustion Institute **31,** 2001 (2007).
[59] C. Kong, Q. Yao, D. Yu, and S. Li, Proceedings of the Combustion Institute (2014).
[60] T. P. Weihs, in *Metallic Films for Electronic, Optical and Magnetic Applications: Structure, Processing and Properties*, edited by K. Barmak and K. Coffey (2014), p. 160.
[61] E. J. Mily, A. Oni, J. M. LeBeau, Y. Liu, H. J. Brown-Shaklee, J. F. Ihlefeld, and J. P. Maria, Thin Solid Films **562,** 405 (2014).
[62] M. Bahrami, G. Taton, V. Conedera, L. Salvagnac, C. Tenailleau, P. Alphonse, and C. Rossi, Propellants Explosives Pyrotechnics **39,** 365 (2014).
[63] A. Ermoline, M. Schoenitz, and E. L. Dreizin, Combustion and Flame **158,** 1076 (2011).
[64] W. L. Shaw, D. D. Dlott, R. A. Williams, and E. L. Dreizin, Propellants Explosives Pyrotechnics **39,** 444 (2014).
[65] M. Schoenitz, T. S. Ward, and E. L. Dreizin, Proceedings of the Combustion Institute **30,** 2071 (2005).
[66] D. Stamatis, Z. Jiang, V. K. Hoffmann, M. Schoenitz, and E. L. Dreizin, Combustion Science and Technology **181,** 97 (2009).
[67] A. Poda, R. Moser, M. Cuddy, Z. Doorenbos, B. Lafferty, C. Weiss, A. Harmon, M. Chappell, and J. Steevens, Nanomater. Mol. Nanotechnol **2,** 1000105 (2013).
[68] H. Wang, G. Jian, G. C. Egan, and M. R. Zachariah, Combustion and Flame **161,** 2203 (2014).
[69] T. Hawa and M. R. Zachariah, Journal of Aerosol Science **38,** 793 (2007).

[70] K. S. Martirosyan, L. Wang, A. Vicent, and D. Luss, Nanotechnology **20** (2009).
[71] R. R. Nellums, B. C. Terry, B. C. Tappan, S. F. Son, and L. J. Groven, Propellants Explosives Pyrotechnics **38,** 605 (2013).
[72] F. Severac, P. Alphonse, A. Esteve, A. Bancaud, and C. Rossi, Advanced Functional Materials **22,** 323 (2012).
[73] R. J. Jacob, B. Wei, and M. R. Zachariah, Combustion and Flame.
[74] T. R. Sippel, S. F. Son, and L. J. Groven, Combustion and Flame **161,** 311 (2014).
[75] V. I. Levitas, B. W. Asay, S. F. Son, and M. Pantoya, Journal of Applied Physics **101** (2007).
[76] C. D. Yarrington, S. F. Son, T. J. Foley, S. J. Obrey, and A. N. Pacheco, Propellants Explosives Pyrotechnics **36,** 551 (2011).
[77] Y.-S. Kwon, A. A. Gromov, and J. I. Strokova, Applied Surface Science **253,** 5558 (2007).
[78] M. K. Berner, V. E. Zarko, and M. B. Talawar, Combustion Explosion and Shock Waves **49,** 625 (2013).
[79] G. C. Egan, T. LaGrange, and M. R. Zachariah, Journal of Physical Chemistry C **119,** 2792 (2015).
[80] V. I. Levitas, J. McCollum, and M. Pantoya, Scientific Reports **5** (2015).
[81] V. I. Levitas, B. Dikici, and M. L. Pantoya, Combustion and Flame **158,** 1413 (2011).
[82] W. G. Kreyling, M. Semmler-Behnke, and W. Moeller, Journal of Nanoparticle Research **8,** 543 (2006).
[83] P. R. N. Childs, in *Practical Temperature Measurement*, edited by P. R. N. Childs (Butterworth-Heinemann, Oxford, 2001), p. 145.
[84] L. Zhou, N. Piekiel, S. Chowdhury, and M. R. Zachariah, Rapid Communications in Mass Spectrometry **23,** 194 (2009).
[85] G. Jian, (2014).
[86] M. Petrantoni, C. Rossi, L. Salvagnac, V. Conedera, A. Esteve, C. Tenailleau, P. Alphonse, and Y. J. Chabal, Journal of Applied Physics **108** (2010).
[87] E. J. Mily, Thesis, North Carolina State University, 2015.
[88] B. N. Chapman, *Glow discharge processes : sputtering and plasma etching* (Wiley, New York, 1980).
[89] D. B. Williams and C. B. Carter, 2nd ed. (Springer, New York, 2009), p. 1 online resource (lxii.
[90] T. LaGrange, G. H. Campbell, B. Reed, M. Taheri, J. B. Pesavento, J. S. Kim, and N. D. Browning, Ultramicroscopy **108,** 1441 (2008).
[91] M. K. Santala, B. W. Reed, T. Topuria, S. Raoux, S. Meister, Y. Cui, T. LaGrange, G. H. Campbell, and N. D. Browning, Journal of Applied Physics **111,** 024309 (2012).
[92] G. H. Campbell, J. T. McKeown, and M. K. Santala, Applied Physics Reviews **1** (2014).
[93] B. W. Reed, T. LaGrange, R. M. Shuttlesworth, D. J. Gibson, G. H. Campbell, and N. D. Browning, Review of Scientific Instruments **81** (2010).
[94] T. LaGrange, B. W. Reed, and D. J. Masiel, Mrs Bulletin **40,** 22 (2015).

[95] S. R. Turns, *An introduction to combustion : concepts and applications*, 3rd ed. (McGraw-Hill, New York, 2012).
[96] J. A. Puszynski, C. J. Bulian, and J. J. Swiatkiewicz, Journal of Propulsion and Power **23,** 698 (2007).
[97] E. S. Domalski and E. D. Hearing, in *NIST Chemistry WebBook, NIST Standard Reference Database Number 69*, edited by P. J. Linstrom and W. G. Mallard (National Institute of Standards and Technology, Gaithersburg, MD 20899), p. http://webbook.nist.gov.
[98] R. Powell, C. Y. Ho, and P. E. Liley, "Thermal conductivity of selected materials," (1966).
[99] M. R. Weismiller, J. G. Lee, and R. A. Yetter, Proceedings of the Combustion Institute **33,** 1933 (2011).
[100] A. Trebs and T. J. Foley, Journal of Propulsion and Power **26,** 772 (2010).
[101] S. H. Fischer and M. C. Grubelich, in *32nd AIAA/ASME/SAE/ASEE Joint Propulsion Conference* (Sandia National Laboratories, Lake Buena Vista, FL, 1996).
[102] Y. J. Min, M. Akbulut, K. Kristiansen, Y. Golan, and J. Israelachvili, Nature Materials **7,** 527 (2008).
[103] B. L. Cushing, V. L. Kolesnichenko, and C. J. O'Connor, Chemical Reviews **104,** 3893 (2004).
[104] P. C. Hiemenz and R. Rajagopalan, *Principles of Colloid and Surface Chemistry, revised and expanded*, Vol. 14 (CRC Press, 1997).
[105] F. E. Kruis, H. Fissan, and A. Peled, Journal of Aerosol Science **29,** 511 (1998).
[106] Y. Chen, R. E. Palmer, and J. P. Wilcoxon, Langmuir **22,** 2851 (2006).
[107] L. Meli and P. F. Green, Acs Nano **2,** 1305 (2008).
[108] R. Prasher, P. E. Phelan, and P. Bhattacharya, Nano Letters **6,** 1529 (2006).
[109] J. W. Chung, S. W. Ko, N. R. Bieri, C. P. Grigoropoulos, and D. Poulikakos, Applied Physics Letters **84,** 801 (2004).
[110] A. Sandmann, C. Notthoff, and M. Winterer, Journal of Applied Physics **113,** 6 (2013).
[111] T. Kim, C. H. Lee, S. W. Joo, and K. Lee, Journal of Colloid and Interface Science **318,** 238 (2008).
[112] C. T. Campbell, S. C. Parker, and D. E. Starr, Science **298,** 811 (2002).
[113] A. K. Datye, Q. Xu, K. C. Kharas, and J. M. McCarty, Catalysis Today **111,** 59 (2006).
[114] A. O. Govorov and H. H. Richardson, Nano Today **2,** 30 (2007).
[115] V. K. Pustovalov, Chemical Physics **308,** 103 (2005).
[116] C. Langhammer, E. M. Larsson, B. Kasemo, and I. Zoric, Nano Letters **10,** 3529 (2010).
[117] T. LaGrange, B. W. Reed, M. K. Santala, J. T. McKeown, A. Kulovits, J. M. K. Wiezorek, L. Nikolova, F. Rosei, B. J. Siwick, and G. H. Campbell, Micron **43,** 1108 (2012).
[118] B. W. Reed, M. R. Armstrong, N. D. Browning, G. H. Campbell, J. E. Evans, T. LaGrange, and D. J. Masiel, Microscopy and Microanalysis **15,** 272 (2009).

[119] M. K. Santala, B. W. Reed, T. Topuria, S. Raoux, S. Meister, Y. Cui, T. LaGrange, G. H. Campbell, and N. D. Browning, Journal of Applied Physics **111** (2012).
[120] B. Alinejad and K. Mahmoodi, International Journal of Hydrogen Energy **34,** 7934 (2009).
[121] X. Y. Huang, P. K. Jiang, and C. U. Kim, Journal of Applied Physics **102** (2007).
[122] Y. N. Zhang, Z. Ouyang, N. Stokes, B. H. Jia, Z. R. Shi, and M. Gu, Applied Physics Letters **100,** 4 (2012).
[123] Y. Ekinci, H. H. Solak, and J. F. Loffler, Journal of Applied Physics **104,** 6 (2008).
[124] T. L. Temple and D. M. Bagnall, Journal of Applied Physics **109,** 13 (2011).
[125] R. A. Yetter, G. A. Risha, and S. F. Son, Proceedings of the Combustion Institute **32,** 1819 (2009).
[126] W. K. Lewis, C. G. Rumchik, M. J. Smith, K. A. S. Fernando, C. A. Crouse, J. E. Spowart, E. A. Guliants, and C. E. Bunker, Journal of Applied Physics **113,** 5 (2013).
[127] D. W. Mackowski and M. I. Mishchenko, Journal of Quantitative Spectroscopy & Radiative Transfer **112,** 2182 (2011).
[128] D. W. Mackowski and M. I. Mishchenko, 2.2 ed. (http://www.eng.auburn.edu/users/dmckwski/scatcodes/, 2011).
[129] D. Y. Smith, E. Shiles, and M. Inokuti, in *Handbook of Optical Constants of Solids*, edited by E. D. Palick (Academic Press, Orlando, 1985), p. 369.
[130] B. Huttner, Journal of Physics-Condensed Matter **6,** 2459 (1994).
[131] T. Q. Qiu, J. P. Longtin, and C. L. Tien, Journal of Heat Transfer-Transactions of the Asme **117,** 340 (1995).
[132] A. S. Rogachev and A. S. Mukasyan, Combustion Explosion and Shock Waves **46,** 243 (2010).
[133] K. S. Martirosyan and M. Zyskin, Applied Physics Letters **102,** 4 (2013).
[134] N. W. Piekiel, L. Zhou, K. T. Sullivan, S. Chowdhury, G. C. Egan, and M. R. Zachariah, Combustion Science and Technology**,** null (2014).
[135] G. Jian, L. Zhou, N. W. Piekiel, and M. R. Zachariah, Chemphyschem **15,** 1666 (2014).
[136] P. Laven; *Vol. 10*, v4.3 ed. (2006).
[137] *M. N. Polyanskiy*; *Vol. 2014* (*http://refractiveindex.info*).
[138] A. V. Kosenko and G. A. Emel'chenko, Journal of Phase Equilibria **22,** 12 (2001).
[139] J. Li, S. Q. Wang, J. W. Mayer, and K. N. Tu, Physical Review B **39,** 12367 (1989).
[140] K. E. Oberg, L. M. Friedman, Boorstei.Wm, and R. A. Rapp, Metallurgical Transactions **4,** 61 (1973).
[141] R. J. Jouet, A. D. Warren, D. M. Rosenberg, V. J. Bellitto, K. Park, and M. R. Zachariah, Chemistry of Materials **17,** 2987 (2005).
[142] E. M. Hotze, T. Phenrat, and G. V. Lowry, Journal of Environmental Quality **39,** 1909 (2010).

[143] O. G. Cervantes, J. D. Kuntz, A. E. Gash, and Z. A. Munir, Combustion and Flame **158,** 117 (2011).
[144] D. A. Fredenburg, A. Jakus, T. McCoy, J. Cochran, and N. Thadhani, Materials Chemistry and Physics **144,** 318 (2014).
[145] J. Kwon, J. M. Ducere, P. Alphonse, M. Bahrami, M. Petrantoni, J.-F. Veyan, C. Tenailleau, A. Esteve, C. Rossi, and Y. J. Chabal, Acs Applied Materials & Interfaces **5,** 605 (2013).
[146] C. Rossi, A. Esteve, and P. Vashishta, Journal of Physics and Chemistry of Solids **71,** 57 (2010).
[147] G. C. Egan, T. LaGrange, and M. R. Zachariah, The Journal of Physical Chemistry C **119,** 2792 (2014).
[148] R. J. Jacob, G. Jian, P. M. Guerieri, and M. R. Zachariah, Combustion and Flame (2014).
[149] Placeholder.
[150] P. R. Childs, *Practical temperature measurement* (Butterworth-Heinemann, 2001).
[151] L. Alawieh, T. P. Weihs, and O. M. Knio, Combustion and Flame **160,** 1857 (2013).
[152] A. B. Mann, A. J. Gavens, M. E. Reiss, D. VanHeerden, G. Bao, and T. P. Weihs, Journal of Applied Physics **82,** 1178 (1997).
[153] A. L. Edwards, "Compilation of Thermal Property Data for Computer Heat-Conduction Calculations," Report No. UCRL--50589 United StatesTue Feb 05 23:26:23 EST 2008Dep. CFSTI.DTIE; NSA-23-026444English (1969).
[154] A. H. Heuer, Journal of the European Ceramic Society **28,** 1495 (2008).
[155] T. Nabatame, T. Yasuda, M. Nishizawa, M. Ikeda, T. Horikawa, and A. Toriumi, Japanese Journal of Applied Physics Part 1-Regular Papers Brief Communications & Review Papers **42,** 7205 (2003).
[156] G. Dutro, S. Son, and A. Tappan, in *The Effect of Microscale Confinement Diameter on the Combustion of an Al/MoO3 Thermite*, 2008.
[157] G. C. Egan and M. R. Zachariah, Combustion and Flame (2015).
[158] W.-C. Huang, L.-M. Lyu, Y.-C. Yang, and M. H. Huang, Journal of the American Chemical Society **134,** 1261 (2012).
[159] H. Preston-Thomas, Metrologia **27,** 3 (1990).
[160] G. C. Egan, E. J. Mily, J. P. Maria, and M. R. Zachariah, Journal of Physical Chemistry C **119,** 20401 (2015).
[161] S. H. Kim and M. R. Zachariah, Advanced Materials **16,** 1821 (2004).
[162] R. Thiruvengadathan, C. Staley, J. M. Geeson, S. Chung, K. E. Raymond, K. Gangopadhyay, and S. Gangopadhyay, Propellants Explosives Pyrotechnics **40,** 729 (2015).
[163] D. G. Wei, R. Dave, and R. Pfeffer, Journal of Nanoparticle Research **4,** 21 (2002).
[164] J. Yang, Y. L. Wang, R. N. Dave, and R. Pfeffer, Advanced Powder Technology **14,** 471 (2003).
[165] A. S. Tappan, J. Cesarano, and J. N. Stuecker, (Sandia Corp).
[166] R. R. Nellums, S. F. Son, and L. J. Groven, Propellants Explosives Pyrotechnics **39,** 463 (2014).

[167] K. T. Sullivan, C. Zhu, D. J. Tanaka, J. D. Kuntz, E. B. Duoss, and A. E. Gash, Journal of Physical Chemistry B **117,** 1686 (2013).
[168] A. S. Tappan, J. P. Ball, and J. W. Colovos, in *The 38th International Pyrotechnics Seminar* (Denver, CO, 2012), p. 605.
[169] R. Shende, S. Subramanian, S. Hasan, S. Apperson, R. Thiruvengadathan, K. Gangopadhyay, S. Gangopadhyay, P. Redner, D. Kapoor, S. Nicolich, and W. Balas, Propellants Explosives Pyrotechnics **33,** 122 (2008).
[170] J. Goldstein, *Scanning electron microscopy and X-ray microanalysis : a text for biologists, materials scientists, and geologists*, 2nd ed. (Plenum Press, New York, 1992).
[171] J. A. Lewis, Advanced Functional Materials **16,** 2193 (2006).
[172] X. Shen, C.-M. Ho, and T.-S. Wong, Journal of Physical Chemistry B **114,** 5269 (2010).
[173] D. M. Kuncicky and O. D. Velev, Langmuir **24,** 1371 (2008).
[174] H. Duan, C. Li, W. Yang, B. Lojewski, L. An, and W. Deng, Journal of Microelectromechanical Systems **22,** 1 (2013).
[175] A. Jaworek and A. T. Sobczyk, Journal of Electrostatics **66,** 197 (2008).
[176] M. D. Grapes, T. LaGrange, L. H. Friedman, B. W. Reed, G. H. Campbell, T. P. Weihs, and D. A. LaVan, Review of Scientific Instruments **85** (2014).
[177] M. D. Grapes, T. LaGrange, K. Woll, B. W. Reed, G. H. Campbell, D. A. LaVan, and T. P. Weihs, Apl Materials **2** (2014).
[178] F. Yi, J. B. DeLisio, M. R. Zachariah, and D. A. LaVan, Analytical Chemistry **87,** 9740 (2015).
[179] W. L. Perry, B. L. Smith, C. J. Bulian, J. R. Busse, C. S. Macomber, R. C. Dye, and S. F. Son, Propellants Explosives Pyrotechnics **29,** 99 (2004).